

Utah State University

DigitalCommons@USU

All Graduate Theses and Dissertations

Graduate Studies

5-1994

A Monte Carlo Simulation of Coulomb Collisions and Wave-Particle Interactions in Space Plasma at High Latitudes

Imad Ahmad Barghouthi

Follow this and additional works at: <https://digitalcommons.usu.edu/etd>



Part of the [Physics Commons](#)

Recommended Citation

Barghouthi, Imad Ahmad, "A Monte Carlo Simulation of Coulomb Collisions and Wave-Particle Interactions in Space Plasma at High Latitudes" (1994). *All Graduate Theses and Dissertations*. 2272. <https://digitalcommons.usu.edu/etd/2272>

This Dissertation is brought to you for free and open access by the Graduate Studies at DigitalCommons@USU. It has been accepted for inclusion in All Graduate Theses and Dissertations by an authorized administrator of DigitalCommons@USU. For more information, please contact digitalcommons@usu.edu.



A MONTE CARLO SIMULATION OF COULOMB COLLISIONS AND
WAVE-PARTICLE INTERACTIONS IN SPACE PLASMA
AT HIGH LATITUDES

by

Imad Ahmad Barghouthi

A dissertation submitted in partial fulfillment
of the requirements for the degree

of

DOCTOR OF PHILOSOPHY

in

Physics

Approved:

Copyright © Imad Barghouthi 1994

All rights reserved

DEDICATION

To the souls of the martyrs of the
blessed Palestinians' uprising
'INTIFADAH'
I am supplicating to you

To my brother Ramadan and his prisonmates, in the
Israeli occupation prisons,
Accept my admirations and appreciations

To the Palestinian children, who are
protesting the Israeli occupation,
by a rock.
I wish to be one of you

ACKNOWLEDGMENTS

Praise and thanks is given first to God, who has provided the author with health, patience, and knowledge to complete this study.

I would like to express my sincere gratitude and appreciation to my major professor, Dr. Abdallah R. Barakat, for his help and support during all phases of my study. With Abdallah, I felt more like a friend or a co-worker than a student. I wish to express heartfelt thanks to my graduate committee, Dr. Robert W. Schunk, for providing helpful suggestions and for his contributions to the manuscript, Dr. Howard G. Demars, Dr. J.R. Dennison, and Dr. Chris S. Coray.

I would like to express my love to my parents, Ahmad Abu Jihad and Fatimah UM Jihad, to my brothers and sisters, Jihad, Hamed, and Ramadan, Suad, and Massadeh. Without their efforts this undertaking would not have been possible.

Special thanks go to my wife, Suhair Um Ahmad, to my son, Ahmad, and my daughter, Sujoud. They have given me a lot of love and power to concentrate on study and not worry about the rest.

I would like to acknowledge my office mates. In particular, Ali Sabbah, for his help and great coffee over the past three years and Tumkur Raghuram for his help in typing the manuscript.

My deepest gratitude and respect to all my brothers at the Logan Islamic Center for their support and encouragement.

I express appreciation to NASA, under contract NAG5-1546 to Utah State University, for financial support.

Imad A. Barghouthi

CONTENTS

iv

	Page
DEDICATION.....	ii
ACKNOWLEDGMENTS.....	iii
LIST OF TABLES.....	vi
LIST OF FIGURES.....	vii
ABSTRACT.....	ix
CHAPTER	
I. INTRODUCTION.....	1
Formulations.....	1
Polar Wind.....	6
Experimental Data.....	8
General Outline.....	10
References.....	12
II. A MONTE CARLO SIMULATION OF THE EFFECT OF ION SELF-COLLISIONS ON THE ION VELOCITY DISTRIBUTION FUNCTION IN THE HIGH LATITUDE F-REGION.....	17
Abstract.....	17
Introduction.....	18
The Model.....	22
Behavior of O ⁺	25
Comparison with Other Work	32
Conclusion.....	38
Appendix.....	40
References.....	41
III. MONTE CARLO STUDY OF THE TRANSITION REGION IN THE POLAR WIND: AN IMPROVED COLLISION MODEL	44
Abstract.....	44
Introduction.....	45
Theoretical Formulation.....	47
Monte Carlo Simulation.....	51
Results.....	54
Conclusion.....	67
References.....	69
IV. THE EFFECTS OF ALTITUDE-DEPENDENT WAVE PARTICLE INTERACTIONS ON POLAR WIND PLASMA.....	72

Abstract.....	72
Introduction.....	73
The Model.....	75
Monte Carlo Simulation.....	77
Wave Spectral Density.....	78
Outflow Characteristics.....	79
Finite Larmor Radius Effect.....	88
Effect of WPI Level.....	96
Summary.....	100
References.....	101
V. THE EFFECTS OF WAVE PARTICLE INTERACTIONS ON H ⁺ AND O ⁺ OUTFLOW AT HIGH LATITUDE: A COMPARATIVE STUDY	105
Abstract.....	105
Introduction.....	106
The Model.....	109
Model Test.....	113
Corrected Auroral Ion Outflow.....	116
Comparison with the Mean Particle Theory.....	121
The Effect of Body Forces.....	123
Comparison Between WPI in the Auroral Region and the Polar Wind..	131
Conclusion.....	134
References.....	135
VI. CONCLUSION.....	138
APPENDIX.....	143
CURRICULUM VITAE.....	147

LIST OF TABLES

Table	Page
V.1 The Monte Carlo results of this study are compared to the Monte Carlo calculations of <i>Retterer et al.</i> (1987a) and to the estimates of the mean particle theory.....	116

LIST OF FIGURES

Figure	Page
I.1 Schematic diagram showing the different regions of the high latitude ionosphere.....	7
I.2 The DE 1 orbit as it appeared shortly after launch.....	9
II.1 Typical O ⁺ and O density profiles.....	21
II.2 Contours of the O ⁺ velocity distribution function in the principal velocity plane parallel to the magnetic field B for an O ⁺ -to-O density ratio equal to 10 ⁻⁵	26
II.3 Contours of the O ⁺ velocity distribution function in the principal velocity plane parallel to the magnetic field B for an O ⁺ -to-O density ratio equal to 10 ⁻⁴	28
II.4 Contours of the O ⁺ velocity distribution function in the principal velocity plane parallel to the magnetic field B for an O ⁺ -to-O density ratio equal to 10 ⁻³	29
II.5 Variation of the O ⁺ temperature characteristics with the electric field <i>E</i> and the O ⁺ -to-O density ratio.....	31
II.6 Comparison of the ion temperature characteristics at low altitude.....	34
II.7 Comparison of the ion temperature characteristics at high altitude.....	35
III.1 A schematic diagram for the flow of the polar wind plasma.....	48
III.2 A schematic diagram of the setup for the Monte Carlo simulation.....	52
III.3 Comparison of the exact profiles (dashed) and the piecewise linear approximation (solid) adopted in the simulation for the H ⁺ normalized potential energy.....	55
III.4 The H ⁺ velocity distribution function for the case of no <i>B</i> field altitude dependence.....	56
III.5 Altitude profiles of the different H ⁺ moments for the case of no <i>B</i> field altitude dependence	59
III.6 The H ⁺ velocity distribution function for the case when the <i>B</i> field altitude dependence is included.....	63
III.7 Altitude profiles of the different H ⁺ moments for the case when the <i>B</i> field altitude dependence is included.....	64

	viii
III.8 Comparison of the H^+ moments for three cases.....	65
IV.1 An example of the observed data.....	80
IV.2 H^+ velocity distributions for the case of negligible WPI.....	81
IV.3 Altitude profiles of the lower order H^+ moments for the case of negligible WPI.....	83
IV.4 O^+ velocity distributions for the case of negligible WPI.....	85
IV.5 Altitude profiles of the lower order O^+ moments for the case of negligible WPI.....	86
IV.6 O^+ velocity distribution function at different geocentric distances.....	90
IV.7 Altitude profiles of the lower order O^+ moment for different electromagnetic turbulence wavelengths (λ).....	92
IV.8 H^+ velocity distribution function at different geocentric distances.....	94
IV.9 Altitude profiles of the lower order H^+ moments.....	95
IV.10 Altitude profiles of the lower order O^+ moments for different spectral densities.....	97
IV.11 Altitude profiles of the lower order H^+ moments for different levels of WPI.....	99
V.1 Profiles of the perpendicular diffusion coefficients $D_{\perp}(O^+)$	112
V.2 The O^+ velocity distribution function $f(O^+)$	114
V.3 Ion velocity distribution functions at different geocentric distances.....	117
V.4 Altitude profiles of the different O^+ (solid) and H^+ (dotted) moments....	119
V.5 Comparison between the Monte Carlo calculations (solid) and the estimates of the mean particle theory (dotted).....	122
V.6 An altitude profile for O^+ density in the auroral region.....	125
V.7 O^+ velocity distribution in the auroral region at different geocentric distances.....	127
V.8a Comparison of the H^+ moments in the polar wind.....	128
V.8b Comparison of the O^+ moments in the polar wind.....	129
V.9 Comparison between the ion moments profiles.....	132

ABSTRACT

A Monte Carlo Simulation of Coulomb Collisions and
Wave-Particle Interactions in Space Plasma
at High Latitudes

by

Imad A. Barghouthi, Doctor of Philosophy
Utah State University, 1994

Major Professor : Dr. Abdallah R. Barakat
Department : Physics

Four studies were considered to simulate the ion behavior in the auroral region and the polar wind.

In study I, a Monte Carlo simulation was used to investigate the behavior of O^+ ions that are $\mathbf{E} \times \mathbf{B}$ -drifting through a background of neutral O, with the effect of O^+ (Coulomb) self-collisions included. Wide ranges of the ion-to-neutral density ratio n_i / n_n and electrostatic field E were considered in order to investigate the change of ion behavior with respect to the solar cycle and altitude. For low altitudes and/or solar minimum ($n_i / n_n \leq 10^{-5}$), the effect of self-collisions is negligible. For higher values of n_i / n_n , the effect of self-collisions becomes significant and, hence, the non-Maxwellian features of the O^+ distributions are reduced.

In study II, the steady-state flow of the polar wind protons through a background of O^+ ions was studied. Special attention was given to using an accurate collision model. The Fokker-Planck expression was used to represent H^+-O^+ Coulomb collisions. The

transition layer between the collision-dominated and the collisionless regions plays a pivotal role in the behavior of the H^+ flow. In the transition region, the shape of H^+ distribution changes in a complicated manner from Maxwellian to "kidney bean". The flow also changes from subsonic to supersonic within the transition region. The heat fluxes of parallel and perpendicular energies change rapidly from their maximum (positive) to their minimum (negative) values within the same transition region.

In study III, a Monte Carlo simulation was developed in order to study the effect of the wave-particle interactions (WPI) on O^+ and H^+ ions outflow in the polar wind. The simulation also considered the other mechanisms included in the classical polar wind studies such as gravity, polarization electrostatic field, and divergence of geomagnetic field lines. Also, an altitude dependent wave spectral density was adopted. The main conclusions are (1) the O^+ velocity distribution develops conic features at high altitudes; (2) the O^+ ions are preferentially energized; (3) the escape flux of O^+ increased by a factor of 40, while the escape flux of H^+ remained constant; (4) including the effect of a finite ion Larmor radius produced toroidal features for O^+ and H^+ distributions at higher altitudes.

In study IV, a comparison between the effect of WPI on H^+ and O^+ ion outflow in the polar wind and in the auroral regions was studied. It was concluded that: (1) O^+ is preferentially energized in both regions; (2) both ions (H^+ and O^+) are more energetic in the auroral region at most altitudes; (3) in the auroral region, the ion conics formed at lower altitudes, at $1.6 R_e$ for O^+ and $2.5 R_e$ for H^+ , while in the polar wind H^+ did not form conics and O^+ formed conics at high altitudes; (4) the effects of body forces are more important in the polar wind than in the auroral region, and for O^+ than H^+ .

CHAPTER I

INTRODUCTION

The Monte Carlo technique is used to approximate the solution of a physical problem by using random sampling. I implemented it in this dissertation to study the effects of ion-self (Coulomb) collisions on the auroral ion velocity distribution in the high latitude F-region. This technique also is used to investigate the effects of wave-particle interactions and Coulomb collisions on the ion outflow at high latitudes. Here, I review the current understanding of the physical mechanisms and tools I used in this dissertation. I describe the Boltzmann equation and the mathematical approaches that have been used over the years to solve that equation in section 1. In section 2, I review the classical polar wind. A short description of the experimental data is provided in section 3. Dissertation outline is presented in section 4.

1. FORMULATIONS

In dealing with gas mixtures it is convenient to describe each species in the mixture by a separate velocity distribution function, $f_s(\mathbf{r}, \mathbf{v}_s, t)$. The velocity distribution function is defined such that $f_s(\mathbf{r}, \mathbf{v}_s, t) d\mathbf{r} d\mathbf{v}_s$ represents the number of particles of species s which at time t have velocities between \mathbf{v}_s and $\mathbf{v}_s + d\mathbf{v}_s$ and positions between \mathbf{r} and $\mathbf{r} + d\mathbf{r}$. Alternatively, f_s can be viewed as a probability density function in the \mathbf{r}, \mathbf{v}_s phase space. The evolution in time of the species velocity distribution function is determined by the net effect of collisions and the flow in phase space of particles under the influence of external forces. The mathematical description of this evolution is given by the well-known Boltzmann equation

$$\frac{\partial f_s}{\partial t} + \mathbf{v}_s \cdot \nabla f_s + \left(\frac{e_s}{m_s}\right) [\mathbf{E} + \mathbf{v}_s \times \mathbf{B} / c] \cdot \nabla_{\mathbf{v}_s} f_s = \left(\frac{\delta f_s}{\delta t}\right) \quad (1)$$

where e_s and m_s are the charge and mass of species s , \mathbf{E} is the electric field, \mathbf{B} is the magnetic field, c is the speed of light, $\partial/\partial t$ is the time derivative, ∇ is the coordinate space gradient, and ∇_{v_s} is the velocity space gradient.

The quantity $\delta f_s/\delta t$ in Boltzmann's equation represents the rate of change of f_s in a given region of phase space as a result of collisions. For collisions governed by inverse power potentials and for resonant charge exchange collisions, the appropriate expression for $\delta f_s/\delta t$ is the Boltzmann collision integral which is given by

$$\frac{\delta f_s}{\delta t} = \sum_t \int dv_t d\Omega g_{st} \sigma_{st}(g_{st}, \theta) [f'_s f'_t - f_s f_t] \quad (2)$$

where dv_t is the velocity-space volume element of species t , g_{st} is the relative velocity of the colliding particles s and t , $\sigma_{st}(g_{st}, \theta)$ is the differential scattering cross section, θ is the scattering angle, $d\Omega$ is the element of solid angle in the s particle reference frame, and the primes denote quantities evaluated after a collision.

Although it would be nice to know the individual velocity distribution functions of the different species, the mathematical difficulties associated with obtaining closed-form solutions to Boltzmann's equation preclude this approach for most flow situations.

A variety of plasma flows can be found throughout the solar terrestrial system, including gentle near-equilibrium flows, such as those that occur on full plasmaspheric flux tubes, as well as highly nonequilibrium supersonic flows like the polar and solar winds. Because the plasma flow conditions can vary markedly within a given region or from one region to another, several different mathematical approaches have been used over the years. These include hydromagnetic, hydrodynamic, generalized transport, kinetic, semi-kinetic formulations, Monte Carlo, and hybrid particle-in-cell (PIC) models [cf. *Oraevskii et al.*, 1968; *Holzer et al.*, 1971; *Lemaire and Scherer*, 1973; *Schunk*, 1977; *Demars and Schunk*, 1987; *Ganguli and Palmadesso*, 1987; *Barakat and Lemaire*, 1990; *Wilson et al.*, 1990].

When applied to different macroscopic plasma flows, all of the mathematical techniques have both strengths and limitations. For example, the transport equations are particularly useful for macroscopic problems because they are relatively easy to solve and because collisions and chemical reactions can be easily included. They are limited, however, in that they correspond to a truncated set of moment equations and the truncation procedure can affect the solution. The kinetic and semi-kinetic models are particularly suited to collisionless, steady-state plasma flows. They have an advantage in that the full hierarchy of moment equations is implicit in the solution and multiple particle populations can be readily included. Some of their limitations are that they are difficult to apply to time-dependent, multi-dimensional or collisional flows, and an artificial discontinuity can occur at the boundary. Monte Carlo and PIC techniques have the advantage that the motion of individual particles can be followed and, hence, a lot of the important physics can be included self-consistently. Monte Carlo techniques are particularly useful for collision-dominated gases, and with the PIC approach, self-consistent electric fields can be taken into account. Some disadvantages are that both techniques are computationally demanding and, therefore, they cannot be easily extended to multi-dimensional situations. Also, for the Monte Carlo method, it is difficult to get an accuracy of better than 1% on the particle distribution function, and the uncertainties increase as higher-order moments (heat flow, stress, etc.) are obtained. Likewise, when PIC techniques are applied to macroscopic flows, "macroparticles" are used and this introduces numerical noise, which can affect the resulting physics. Clearly, a better understanding of the limitations associated with the various mathematical approaches will lead to an improved interpretation of the model results. In the next three paragraphs, the different approaches are discussed in more detail, with Monte Carlo simulation emphasised.

1.2. Transport Equations

The generalized transport equations are obtained by taking velocity moments of the Boltzmann equation. Specifically, the Boltzmann equation is multiplied by a set of velocity functions and then integrated over velocity space. The result is a hierarchy of coupled partial differential equations which describe the spatial-temporal variation of the velocity moments. To close the system of equations, a specific form for the particle velocity distribution function must be adopted. The general approach is to expand the distribution function in a complete, orthogonal series about a weight factor (zeroth-order distribution function). If a Maxwellian is taken as the zeroth-order distribution [Grad, 1949], the truncation of the series at various levels leads to the well-known 5-moment, 13-moment, and 20-moment approximations. At the 13-moment level of approximation, stress and heat flow are put on an equal footing with the lower-order moments (density, drift velocity, temperature), and, hence, this level of approximation is very useful. However, for highly anisotropic space plasmas, it is more appropriate to expand the distribution function about zeroth-order bi-Maxwellian distribution function [cf. *Oraevskii et al.*, 1968; *Barakat and Schunk*, 1982a, b]. When the series is truncated at the 16-moment level, there are separate transport equations to describe the density, drift velocity, parallel and perpendicular (to \mathbf{B}) temperatures, and the flow of parallel and perpendicular thermal energies (heat flows).

1.2. Kinetic Models

With the kinetic approach, the Boltzmann equation is directly solved to give the spatial-temporal variation of the particle distribution function in terms of a known (typically assumed) distribution function at the boundary [Lemaire and Scherer, 1973]. Although the full hierarchy of moment equations is implicit in a kinetic solution, the result is sensitive to the assumptions made about the particle dynamics and populations. Nevertheless, this approach is extremely powerful for certain collisionless space plasma

applications. Also, if one of the species (either the electrons or the ions) can be described by fluid equations (semi-kinetic model), the approach is even more useful.

1.3. Monte Carlo Techniques

Monte Carlo (MC) techniques have the advantage that one follows the motion of the individual particles and, hence, a lot of the important physics can be included self-consistently. The standard procedure of the Monte Carlo simulation is to follow the motion of one ion for a large number of collisions, and to continually monitor its velocity. Then, various kinds of time averages for the ion are computed, which can be equated to the corresponding ensemble averages of the system. In practice, the ion motion is simulated as follows. The time interval between every two successive collisions is found via a proper random number generator. The ion trajectories during these intervals are determined by the classical laws of motion of a charge particle under the influence of electric and magnetic fields. Changes of ion velocity due to collisions are determined using another set of random numbers having the statistical properties determined according to the chosen collision model. Then, a suitable grid in velocity space is used to register the ion's behavior. The time that an ion spends in each bin, divided by the bin's volume, is taken to be proportional to the ion velocity distribution function at its center. Moreover, the individual segments of the trajectory can be directly used to find different velocity moments. The general aspects of this technique are discussed in more detail by *Lin and Bardsley [1977]*, while some fine details, which depend on the specific collision model, are discussed in the appropriate chapters.

Recently, the Monte Carlo simulation was shown to be a very powerful technique in solving Boltzmann's equation by particle simulation [*Barakat and Lemaire, 1990*]. Its simple concept, straightforward algorithm, and its adaptability to include new features (such as electrostatic field, magnetic field, and different collision models) make it a useful tool in physics, and a powerful test of results obtained with other mathematical methods.

The early attempts were largely limited by computational facilities. But as computer technology has improved in the succeeding years, more computing power became available at lower expense, and the Monte Carlo particle simulation has become a more viable alternative to address physical and engineering problems.

The Monte Carlo technique has been used in space physics by several authors, such as *Barakat and Schunk* [1982b, 1983], *Barakat and Lemaire* [1990], *Wilson et al.*, [1990], *Barakat and Hubert* [1991], and *Winkler et al.*, [1992]. This technique is the basis of the models that were developed and applied in this dissertation.

2. POLAR WIND

In the early 1960's, it was recognized that the interaction of the solar wind with the earth's dipole magnetic field acts to significantly modify the magnetic field configuration in the vast region close to the earth [*Axford and Hines*, 1961; *Dungey*, 1961]. The dynamo action associated with the flow of solar wind plasma across magnetic field lines generates an intense current system which acts to compress the earth's magnetic field on the sunward side and stretch it into a long comet-like tail on the anti-sunward. The magnetic field lines which form the tail originate in the earth's polar regions, and since the pressure in the ionosphere is much greater than that in the distant tail, it was suggested that a continual escape of thermal plasma (H^+ and He^+) should occur along these open field lines [*Dessler and Michel*, 1966]. *Nishida* [1966] also proposed an escape of thermal plasma in combination with horizontal plasma convection to explain the experimental discovery of the plasmopause by whistler measurements.

These early suggestions of light ion outflow were based on the well-known theory of thermal evaporation, which had been successfully applied to the escape of neutral gases from planetary atmospheres. Via thermal evaporation, the light ions would escape the topside ionosphere (figure I.1) with velocities close to their thermal velocities and then

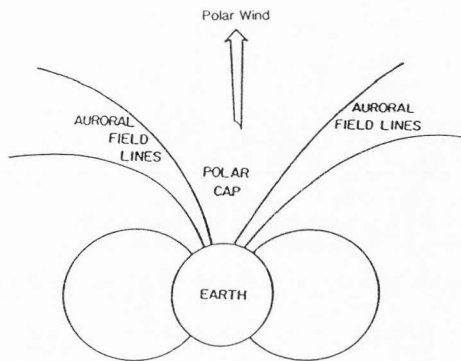


Figure I.1 Schematic diagram showing the different regions of the high latitude ionosphere. The classical polar wind occurs in the polar cap region.

flow along magnetic field lines to the magnetospheric tail. However, it was subsequently argued that the outflow should be supersonic and it was termed the polar wind in analogy to the solar wind [Axford, 1968]. A hydrodynamic model was then used that emphasized the supersonic nature of the flow, thereby elucidating its basic characteristics [Banks and Holzer, 1969; Marubashi, 1970].

It is now well known that the classical polar wind is an ambi-polar outflow of thermal plasma from the high-latitude ionosphere and that it undergoes four major transitions, including a transition from chemical to diffusion dominance, a transition from subsonic to supersonic flows, a transition from collision dominated to collisionless regimes, and a transition from a heavy to a light ion dominance. Also, recent measurements have indicated that the polar wind contains suprathermal components of both light and heavy ions [Lockwood *et al.*, 1985; Yau *et al.*, 1985; Moore *et al.*, 1986]. Because of the complicated nature of the flow, numerous mathematical models have been constructed over the years, including hydrodynamic [Banks and Holzer, 1969; Raitt *et al.*, 1975], hydromagnetic [Holzer *et al.*, 1971], generalized transport [Schunk and Watkins, 1981, 1982], kinetic [Lemaire and Scherer, 1973], and semi-kinetic [Barakat and Schunk, 1983, 1984]. These models have been used primarily to study the steady-state characteristics of the flow, with emphasis on elucidating physical processes.

3. EXPERIMENTAL DATA

In Chapters IV and V, I used the observed wave spectra of the electromagnetic turbulence as an input to my polar wind models. The principal source of these measured waves needed for the proposed studies is the data collected by the Plasma Wave Instrument (PWI) on the Dynamics Explorer 1 (DE 1) spacecraft. In particular, the low frequency range of the wave spectrum (\leq ion cyclotron frequency) measured above the high latitude region is the most relevant to our study since it is expected to interact with the

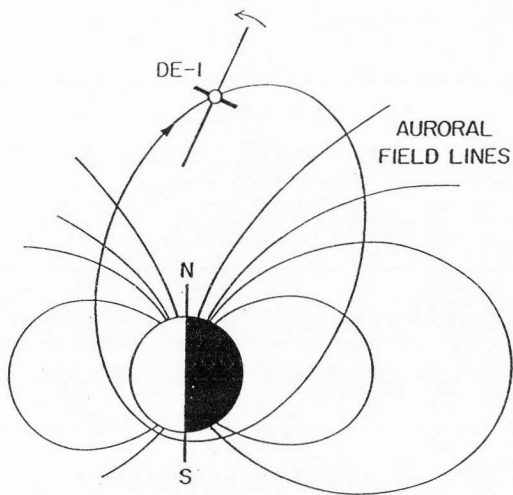


Figure 1.2. The DE 1 orbit as it appeared shortly after launch. The spacecraft spin axis is perpendicular to the orbital plane. The argument of perigee advances at a rate of 108° per year, thereby providing excellent coverage of the polar cap, the auroral field lines, and the equatorial region at radial distances extending out to $4.65 R_e$ [Gurnett *et al.*, 1988].

ions more efficiently. The DE 1 was launched on August 2, 1983, into a highly elliptical polar orbit with a perigee and apogee altitudes of 1.09 Re and 4.65 Re, respectively. Its initial orbit is shown schematically in figure I.2, and the orbit rotates such that it provides a complete coverage in about three years.

The PWI is designed to measure the electric and magnetic field over a wide range of frequencies (1 Hz to 400 kHz). It includes five antennas, a 200-m electric dipole perpendicular to the spin axis, a 9-m electric dipole parallel to the spin axis, a 0.6-m short electric antenna, and two magnetic antenna to provide the data for the magnetic field. A cross correlation between any selected pair of antennas is provided depending on the mode of operation. The correlation data provide additional information about the polarization of the wave and whether it is electrostatic or electromagnetic. A more detailed description of the instrument and the obtained data is given elsewhere [Shawhan *et al.*, 1981; Gurnett and Inan, 1988] and a comprehensive discussion of the low frequency range, which is relevant to this study, is given in [Gurnett *et al.*, 1984].

4. GENERAL OUTLINE

This dissertation consists of six chapters. In Chapter II, I studied the effect of O^+ - O^+ self-(Coulomb) collisions on the non-Maxwellian O^+ velocity distribution function. Non-Maxwellian ion velocity distribution functions have been predicted theoretically and confirmed by observations to occur at high latitudes [Barakat *et al.*, 1983; Barakat and Hubert, 1990; Hubert and Barakat, 1990; Winkler *et al.*, 1992]. The deviations of these distributions from Maxwellian are due to the interplay between the $\mathbf{E} \times \mathbf{B}$ - drift and ion-neutral collisions. In particular, the O^+ ion velocity distribution has a toroidal shape, especially for high electrostatic field values ($E \geq 100$ mV/m). At high latitudes and/or solar maximum conditions, the ion-to-neutral density ratio increases, and consequently, self-collisions play a significant role compared to ion-neutral collisions. I used a Monte

Carlo simulation to investigate the effect of ion-ion (Coulomb) collisions on the ion velocity distribution function and its moments (parallel temperature, perpendicular temperature, etc). A wide range of ion-to-neutral density ratios and electrostatic field intensities (E) were considered. This enabled us to understand the change in ion behavior with solar cycle and with altitude.

In Chapter III, I studied the effect of H^+O^+ Coulomb collisions on the hydrogen ion outflow in the polar wind. With regard to the behavior of the ions, there are two different regions: 1) the collision-dominated region (ion-barosphere); and 2) the collisionless region (ion-exosphere). I developed a Monte Carlo code to study the outflow of H^+ ions with emphasis on the transition layer between the collisionless and the collision-dominated regions. I calculated the H^+ velocity distribution function and its moments (drift velocity, parallel temperature, perpendicular temperature, parallel heat flow, and perpendicular heat flow) at different altitudes. Also, I investigated the effect of the polarization electric field and of inter-particle collision models (Maxwell molecule and Coulomb).

In Chapter IV, I studied the effect of wave-particle interactions on the ion outflow of the polar wind plasma at high latitudes. The escape of ionospheric ions at high latitude is an important element in the ionosphere-magnetosphere coupling. Most of the previously developed models [Barakat and Schunk, 1983; Demars and Schunk, 1989; Barakat and Lemaire, 1990] did not properly account for the wave-particle interactions (WPI). Both theory and measurements indicated that the WPI play a significant role in the dynamics of ion outflow along open geomagnetic field lines. I used the low frequency wave data measured by the Plasma Wave Instrument (PWI) aboard the Dynamics Explorer 1 (DE 1) satellite and a Monte Carlo simulation to include the effects of the WPI in addition to the other mechanisms included in the "classical" polar wind (i.e., gravity, polarization electrostatic field, and divergence of geomagnetic field lines). In this chapter,

I investigated the effects of WPI in the polar wind region on the following: (1) the ion distribution function and the profiles of its moments (density, drift velocity, and temperatures), (2) the magnitude and composition of the ion escape fluxes, and (3) the preferential heating of the heavy ions.

In Chapter V, I used a Monte Carlo simulation to study the effect of wave-particle interaction (WPI) on ion outflow at high latitudes (the auroral region and the polar cap). As the ions drift upward along the geomagnetic field lines, they interact with the electromagnetic turbulence and consequently get heated in the direction perpendicular to the geomagnetic field. The mirror force converts some of the gained ion energy in the perpendicular direction into parallel kinetic energy. These effects combine to form an ion-conic distribution. Previous studies [*Chang et al.*, 1986; *Retterer et al.*, 1987; *Crew et al.*, 1990] of WPI in the auroral region neglected the body forces (i.e., gravitational and polarization electrostatic) and the altitude-dependence of the spectral density. In contrast, this work included the effect of body forces, and an altitude-dependent spectral density. The ion distribution function, the profiles of ion density, drift velocity, and parallel and perpendicular temperatures were presented for both H^+ and O^+ ions. These results were compared to the ones corresponding to polar wind conditions.

General conclusions and the experimental observations that supported the theoretical predictions of this dissertation are presented in Chapter VI.

REFERENCES

- Axford, W. I., The polar wind and the terrestrial helium budget, *J. Geophys. Res.*, 73, 6855-6859, 1968.
- Axford, W. I., and C. O. Hines, A unifying theory of high-latitude geophysical phenomena and geomagnetic storms, *Com. J. Phys.*, 39, 1433, 1961.

- Banks, P. M., and T. E. Holzer, Features of plasma transport in the upper atmosphere, *J. Geophys. Res.*, 74, 6304, 1969.
- Barakat, A. R., and D. Hubert, Comparison between the Monte Carlo solution of the non-Maxwellian ion distributions and the generalized polynomial expansion: II. 1-D distributions, *Annales Geophys.*, 697, 1990.
- Barakat, A. R., and J. Lemaire, Monte Carlo study of the escape of a minor species, *Phys. Rev.*, A, 42, 3921, 1990.
- Barakat, A. R., and R. W. Schunk, Comparison of transport equations based on Maxwellian and bi-Maxwellian distributions for anisotropic plasmas, *J. Phys. D: Appl. Phys.*, 15, 1195, 1982a.
- Barakat, A. R., and R. W. Schunk, Comparison of Maxwellian and bi-Maxwellian expansions with Monte Carlo simulations for anisotropic plasmas, *J. Phys. D: Appl. Phys.*, 15, 2189, 1982b.
- Barakat, A. R., and R. W. Schunk, O⁺ ions in the polar wind, *J. Geophys. Res.*, 88, 7887-7894, 1983.
- Barakat, A. R., and R. W. Schunk, O⁺ ions in the polar wind, *J. Geophys. Res.*, 89, 9771, 1984.
- Barakat, A. R., R. W. Schunk, and J.-P. St.-Maurice, Monte Carlo calculations of the O⁺ velocity distribution in the auroral plasma, *J. Geophys. Res.*, 88, 3237, 1983.
- Chang, T., G. B. Crew, N. Hershkowitz, J. R. Jasperse, J. M. Retterer, and J. D. Winningham, Transverse acceleration of oxygen ions by electromagnetic ion cyclotron resonance with broadband left-hand-polarized waves, *Geophys. Res. Lett.*, 13, 636, 1986.
- Crew, G. B., T. Chang, J. M. Retterer, W. K. Peterson, D. A. Gurnett, and R. L. Huff, Ion cyclotron resonance heated conics: Theory and observations, *J. Geophys. Res.*, 95, 3959, 1990.

- Demars, H. G., and R. W. Schunk, Temperature anisotropies in the terrestrial ionosphere and plasmasphere, *Rev. Geophys.*, 25, 1659, 1987.
- Demars, H. G., and R. W. Schunk, Solutions to bi-Maxwellian transport equations for the polar wind, *Planet. Space Sci.*, 37, 85, 1989.
- Dessler, A. J., and F. C. Michel, Plasma in the geomagnetic tail, *J. Geophys. Res.*, 71, 1421, 1966.
- Dungey, J. W., Interplanetary magnetic field and the auroral zones, *Phys. Rev. Lett.*, 6, 47, 1961.
- Ganguli, S. B., and P. J. Palmadesso, Plasma transport in the auroral return current region, *J. Geophys. Res.*, 92, 8673, 1987.
- Grad, H., On the kinetic theory of rarefied gases, *Commun. Pure Appl. Math.*, 2, 331, 1949.
- Gurnett, D. A., R. L. Huff, J. D. Menietti, J. L. Burch, J. D. Winningham, and S. D. Shawhan, Correlated low-frequency electric and magnetic noise along the auroral field lines, *J. Geophys. Res.*, 84, 8971, 1984.
- Gurnett, D. A., and U. S. Inan, Plasma wave observations with the Dynamics Explorer 1 spacecraft, *Rev. Geophys.*, 26, 285, 1988.
- Holzer, T. E., J. A. Fedder, and P. M. Banks, A comparison of kinetic and hydrodynamic models of an expanding ion-exosphere, *J. Geophys. Res.*, 76, 2453, 1971.
- Hubert, D., and A. R. Barakat, Comparison between the Monte Carlo solution of the non-Maxwellian ion distributions and the generalized polynomial expansion: I. 3-D distributions, *Annales Geophys.*, 687, 1990.
- Lemaire, J., and M. Scherer, Kinetic models of the solar and polar winds, *Rev. Geophys. Space Phys.*, 11, 427, 1973.

- Lin, S. L., and J. N. Bradsley, Monte Carlo simulation of ion motion in drift tubes, *J. Chem. Phys.*, 66, 435-445, 1977.
- Lockwood, M., J. H. Waite, T. E. Moore, J. F. E. Johnson, and C. R. Chappell, A new source of suprathermal O^+ ions near the dayside polar cap boundary, *J. Geophys. Res.*, 90, 4099, 1985.
- Marubashi, K., Escape of the polar-ionospheric plasma into the magnetospheric tail, *Rep. Ionosph. Space Res. Japan*, 24, 322, 1970.
- Moore, T. E., M. Lockwood, M. O. Chandler, J. H. Waite, Jr., C. R. Chappell, A. Persoon, and M. Suguira, Upwelling O^+ ion source characteristics, *J. Geophys. Res.*, 91, 7019, 1986.
- Nishida, A., Formation of a plasmopause or magnetospheric convection and plasma escape from the tail, *J. Geophys. Res.*, 71, 5669, 1966.
- Oraevskii, V., R. Chodura, and W. Feneberg, Hydrodynamic equations for plasmas in strong magnetic fields, *I. Plasma Phys.*, 10, 819, 1968.
- Raitt, W. J., R. W. Schunk, and P. M. Banks, A comparison of the temperature and density structure in high and low speed thermal proton flows, *Planet. Space Sci.*, 23, 1103, 1975.
- Retterer, J. M., T. Chang, G. B. Crew, J. R. Jasperse, and J. D. Winningham, Monte Carlo modeling of oxygen ion conic acceleration by cyclotron resonance, *Phys. Rev. Lett.*, 59, 148, 1987.
- Schunk, R. W., Mathematical structure of transport equations for multispecies flows, *Rev. Geophys. Space Phys.*, 15, 429, 1977.
- Schunk, R. W., and D. S. Watkins, Electron temperature anisotropy in the polar wind, *J. Geophys. Res.*, 86, 91, 1981.
- Schunk, R. W., and D. S. Watkins, Proton temperature anisotropy in the polar wind, *J. Geophys. Res.*, 87, 171, 1982.

- Shawhan, S. D., D. A. Gurnett, D. L. Adem, R. A. Helliwell, and C. G. Park, The plasma wave and quasi-static electric field instrument (PWI) for Dynamics Explorer-A, *Space Sci. Inst.*, 5, 535, 1981.
- Wilson, G. R., C. W. Ho, J. L. Horwitz, N. Singh, and T. E. Moore, A new kinetic model for time-dependent polar plasma outflow: Initial results, *Geophys. Res. Lett.*, 17, 263, 1990.
- Winkler E., J.-P. St-Maurice, and A. R. Barakat, Results from improved Monte Carlo calculations of auroral ion velocity distributions, *J. Geophys. Res.* 97, A6, 8399-8423, 1992.
- Yau, A. W., E. G. Shelley, W. K. Peterson, and L. Lenchyshyn, Energetic auroral and polar ion outflow at DE 1 altitudes: Magnitude, composition, magnetic activity dependence, and long-term variations, *J. Geophys. Res.*, 90, 8417, 1985.

CHAPTER II

A MONTE CARLO SIMULATION FOR THE EFFECT OF ION SELF-COLLISIONS ON THE ION VELOCITY DISTRIBUTION FUNCTION IN THE HIGH-LATITUDE F-REGION¹

ABSTRACT

Non-Maxwellian ion velocity distribution functions have been predicted theoretically, and confirmed by observations, to occur at high latitudes. These distributions deviate from Maxwellian due to the combined effect of the $\mathbf{E} \times \mathbf{B}$ -drift and ion-neutral collisions. The majority of the previous literature, in which the effect of ion self-collisions was neglected, established a clear picture for the ion distribution under a wide range of conditions. At high altitudes and/or for solar maximum conditions, the ion-to-neutral density ratio increases and, hence, the role of ion self-collisions becomes appreciable. A Monte Carlo simulation was used to investigate the behavior of O^+ ions that are $\mathbf{E} \times \mathbf{B}$ -drifting through a background of neutral O, with the effect of O^+ (Coulomb) self-collisions included. Wide ranges of the ion-to-neutral density ratio n_i/n_n , and the electrostatic field E were considered in order to investigate the change of ion behavior with solar cycle and with altitude. For low altitudes and/or solar minimum ($n_i/n_n \leq 10^{-5}$), the effect of self-collisions is negligible. For higher values of n_i/n_n , the effect of self-collisions becomes significant and, hence, the non-Maxwellian features of the O^+ distribution are reduced, i.e., the parallel temperature $T_{i\parallel}$ increases, the perpendicular temperature $T_{i\perp}$ decreases, the temperature anisotropy approaches unity, and the toroidal features of the ion distribution function becomes less pronounced. Also, as E increases,

¹ Coauthored by A. R. Barakat and R. W. Schunk.

the ion-neutral collision rate increases, while the ion-ion collision rate decreases. Therefore, the effect of the ion self-collisions is reduced. Finally, the Monte Carlo results were compared to the ones that used simplified collision models in order to assess their validity. In general, the simple collision models tend to be more accurate for low E and for high n_i/n_n .

1. INTRODUCTION

The presence of relatively high electrostatic fields in the high latitude F region results in $\mathbf{E} \times \mathbf{B}$ ion drifts that can exceed the neutral gas thermal velocity. As a result of the interplay between these large drifts and ion-neutral collisions, the ion velocity distribution function shows significant non-Maxwellian features, such as a temperature anisotropy (with $T_{i\perp} > T_{i\parallel}$) and toroidal characteristics.

This problem was first addressed by *Cole* [1971]. Since this study, the large number of scientific studies that have been conducted can be classified into three categories: theoretical, simulation, and experimental. With regard to the first category, Boltzmann's equation was directly solved after replacing the collision term with a BGK expression [*St.-Maurice and Schunk*, 1973; *Barakat and Schunk*, 1982]. In these studies, the non-Maxwellian features of the ion velocity distribution were established in a qualitative sense, but the simple BGK collision term was found to exaggerate the non-Maxwellian features. Boltzmann's equation with more realistic (yet more complicated) collision terms was solved by expanding the ion distribution function about a zero-order function $f_i^{(0)}$ [*Schunk and Walker*, 1972; *St.-Maurice and Schunk*, 1976; *Hubert*, 1983; 1984a]. In these studies the quantitative behavior of the ion distribution function was clearly established. However, since a small number of correction terms were used in such expansions, the results were not valid for relatively large values of E , nor were they valid for ions in the tail of the distribution function.

Monte Carlo simulations were used to find the distribution function for arbitrarily large E and for realistic collision models [Barakat *et al.*, 1983; Winkler *et al.*, 1992]. Barakat and Hubert [1990] used a Monte Carlo simulation to show that for large values of E the O^+ distribution function f_i displays features that are difficult to model analytically, and that several higher-order correction terms are needed to give a satisfactory approximation for f_i .

Several observations confirmed the non-Maxwellian features of f_i as theoretically predicted. Perraut *et al.* [1984], using data from an incoherent scattering radar (EISCAT), observed an ion temperature anisotropy ($T_{i\perp}/T_{i\parallel}$) as high as 1.5. The EISCAT data were also used to study the toroidal features of f_i [Winser *et al.*, 1986; Lockwood *et al.*, 1987].

The toroidal features of f_i need to be taken into consideration when studying certain properties of the F-region, such as plasma instabilities, the incoherent scattering radar, the IV characteristics of the retarding potential analyzer (RPA), and the F-region irregularities. Raman *et al.* [1981] and Hubert [1984b] predicted that as E increases and, hence, the toroidal characteristics of f_i increase, the incoherent scattering radar spectra change from the normal double-hump shape to a triple hump, and finally to a "baby bottle" shape. These signatures were observed in the EISCAT data [Lockwood *et al.*, 1987]. The instability of the non-Maxwellian ion distributions [St.-Maurice and Schunk, 1979], and the current-voltage (I-V) characteristics of the RPA [St.-Maurice *et al.*, 1976] were investigated under conditions of non-Maxwellian f_i . Barakat *et al.* [1990] used a Monte Carlo simulation to find f_i , from which the shape of the incoherent radar spectrum was directly derived. They showed that the shape of the spectrum is very sensitive to the details of the distribution function.

Recently, Hubert *et al.* [1993] deduced that at a certain angle to the geomagnetic field B , the 1-D line-of-sight distribution displays a Maxwellian shape. They suggested a scenario to use the radar measurements along that direction to find the plasma parameters.

An accurate and efficient method to interpret the incoherent radar spectrum scattered from a non-Maxwellian f_i was suggested by *Elssamadisy et al.* [1992]. This method, which was based on the "neural network" approach, was tested successfully on a large set of synthetic data.

In all the studies mentioned above the effect of ion self-collisions was neglected, which is valid in the lower F-region and for high electric fields [cf. *Schunk et al.*, 1975]. As shown in Figure II.1, the ion-to-neutral density ratio increases rapidly with altitude. Therefore, at high altitudes, ion self-collisions play a significant role in deciding the shape of f_i and should be included in the simulation. The role of ion self-collisions becomes even more significant for solar maximum conditions where n_i is enhanced. Therefore, ion self-collisions can have an indirect influence on the measurements, such as the shape of the scattered wave spectrum of an incoherent scattering radar, and the I-V curve of a retarding potential analyzer.

Tereshchenko et al. [1991] studied the effect of O^+ self-collisions on the ion velocity distribution function and on the corresponding incoherent scatter radar spectrum. However, in order to get a closed form analytical solution for Boltzmann's equation, they adopted several simplifying assumptions, such as: a simple (BGK) collision term, and ion-ion and ionneutral collision frequencies that were velocity independent and based on Maxwellian distributions. *Kinzelin and Hubert* [1992] improved on this model by using a modified BGK collision term with the collision frequencies computed self-consistently with the adopted phenomenological ion distribution function. As a result of this modification, the ratio of the ion-ion and ion-neutral collision frequencies (v_{ii}/v_{in}) was corrected by a factor of up to 50%.

Barghouthi et al. [1991] used a Monte Carlo simulation to find f_i for more realistic collision models, and this chapter is an augmented version of their AGU (American Geophysical Union) presentation. This approach not only accurately predicts the moments

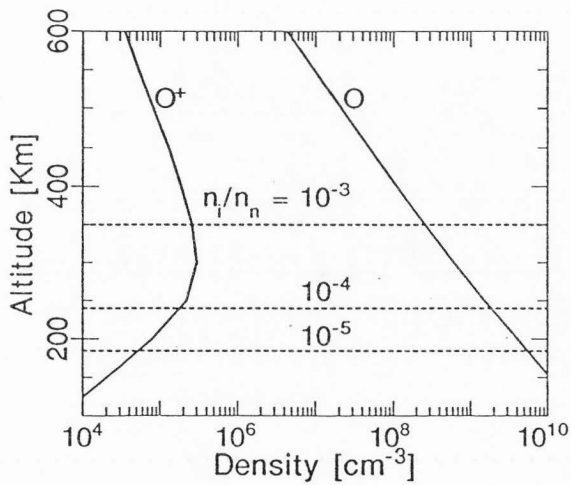


Fig. II.1. Typical O⁺ and O density profiles. The dotted lines indicate the altitudes at which the O⁺-to-O density ratio equals 10⁻⁵, 10⁻⁴, and 10⁻³.

of f_i (e.g., $T_{i\parallel}$ and $T_{i\perp}$), but also gives additional details of f_i that are very difficult to model with analytical expressions [Winkler *et al.*, 1992], such as the ones used by Tereshchenko *et al.* [1991] and by Kinzelin and Hubert [1992]. However, the additional details are very important in studying the plasma stability and the incoherent scatter radar spectrum.

2. THE MODEL

Our objective is to calculate the auroral O^+ velocity distribution function using a Monte Carlo simulation technique. Our work is an extension of Barakat *et al.* [1983], who studied the effect of ion-neutral collisions on the O^+ velocity distribution function. In this work, we use the same model for ion-neutral collisions (polarization scattering and resonance charge exchange) that was used by Barakat *et al.* [1983], but as an extension to that work we include ion-ion Coulomb collisions. The effect of ion-ion collisions becomes important at high altitudes where the ion-ion collision frequency (ν_{ii}) becomes comparable to or greater than the ion-neutral collision frequency (ν_{in}). Note that subscripts i and n refer to O^+ and O , respectively.

In our Monte Carlo simulation, the motion of an oxygen ion is followed for a short period of time. At the end of each period, the effect of a binary self-Coulomb-collision is included to determine the ion velocity after collisions [Takisuki and Abe, 1977]. After several ion self-collisions, an ion-neutral collision occurs. By knowing the physical situation of the problem, the scattering process can be specified as either a polarization interaction or a resonance charge exchange interaction. For each process, the effect on the O^+ velocity is then determined. Consequently, the O^+ velocity distribution can be calculated. Note that between collisions the oxygen ion moves in a circle centered at \mathbf{v}_D (i.e., the $\mathbf{E} \times \mathbf{B}$ drift). In order to calculate the ion velocity distribution function, a 2-D grid is used with velocity coordinates parallel and perpendicular to the geomagnetic field.

The ion motion is monitored and the time spent in each bin is accumulated. This time, divided by the bin's size, is taken to be proportional to f_i at the center of the bin. Also, the data needed to compute $T_{i\parallel}$ and $T_{i\perp}$ directly are accumulated. In calculating the distribution function, we assume it to be azimuthally symmetric in velocity space, since in the F-region the ion collision frequency is much smaller than the ion cyclotron frequency. In the following subsections, we briefly present the models for ion-neutral and ion-ion collisions.

2.1. Resonance Charge Exchange (RCE)

For collisions between an ion and its parent neutral, an electron will switch from the neutral to the ion, and this process is called a resonant charge exchange (RCE). The probability for this process to occur is very high when the relative ion-neutral speed is high. In this case, it is necessary to include the quantum mechanical behavior of the collision process, which complicates the problem. To avoid this complexity, *Barakat et al.* [1983] assumed a reasonable phenomenological model for the probability of RCE,

$$P_{ex} = \begin{cases} 0.5 & \text{for } b < b_o(g) \\ 0 & \text{elsewhere} \end{cases} \quad (1)$$

where $g[=|v_i - v_n|]$ is the relative velocity, b is the impact parameter, and $b_o(g)$ is chosen such that the total cross-section for RCE is given by *Knof et al.* [1964],

$$Q_E(g) = (10.995 - 0.95 \log_{10} g)^2 \times 10^{-16} \quad (2)$$

where

$$Q_E = 2\pi \int_0^{\infty} db b P_{ex}(g, b) \quad (3)$$

2.2. Polarization Interaction

For low ion-neutral relative speeds, O^+ induces a dipole moment in the O neutral. Consequently, a polarization force will affect the O^+ motion. The polarization interaction model used here is the same model used by *Barakat et al.* [1983]. In this model, the polarization scattering is isotropic (i.e., the differential scattering cross section is independent of the scattering angle χ) and the scattering cross section σ is given by

$$\sigma(g, \chi) = 0.55(\alpha e^2 / \mu g^2)^2 \quad (4)$$

where α is the oxygen polarizability ($0.77 \times 10^{-24} \text{ cm}^3$), e is the electron charge, and μ is the reduced mass.

2.3 Coulomb Collisions

The main idea of this work is to study the effect of ion-ion collisions on the ion temperature and the ion velocity distribution function. In our model, ion self-collisions were included as a binary Coulomb collision, as suggested by *Takizuka and Abe* [1977]. In this case, we can randomly choose a pair of oxygen ions. As a result of a Coulomb collision, the absolute value of the relative velocity $\mathbf{u} [= \mathbf{v}_{i1} - \mathbf{v}_{i2}]$ does not change, but its direction does change.

In a time period Δt , an ion makes many small angle scatterings. The accumulation of these small angle scatterings is used to compute the deflection in the relative velocity \mathbf{u} . The variable $\delta = \tan(\theta/2)$ (θ is the deflection angle) is chosen randomly from a Gaussian distribution with zero mean and variance $\langle \delta^2 \rangle$ given by

$$\langle \delta^2 \rangle = \frac{2\pi e^4 n_i \lambda}{m_i^2 u^3} \Delta t \quad (5)$$

where n_i is the oxygen ion density, m_i is the oxygen mass, e is the electron charge, and λ is the Coulomb logarithm. The change in the velocity is given by

$$v'_{i1} = v_{i1} + \frac{\Delta \mathbf{u}}{2} \quad (6)$$

$$v'_{i2} = v_{i2} - \frac{\Delta \mathbf{u}}{2} \quad (7)$$

where the primes denote velocities after collisions. According to equations (6) and (7), the momentum and energy for both particles are conserved and they will be conserved for all of the particles.

3. BEHAVIOR OF O⁺

In this section, we present the auroral ion velocity distribution, f_i , for different density ratios [$n_i/n_n = 10^{-5}$, 10^{-4} , and 10^{-3}], and for different electric field intensities [$E = 0, 50, 100$, and 150 (mV/m)]. In this work, the distribution function of the background f_n (i.e., neutral O) was taken to be Maxwellian, with the temperature equal to 1000K, and the geomagnetic field B was assumed to be 0.5 Gauss. As we said earlier, we use the Monte Carlo simulation to calculate the O⁺ velocity distribution, and its parallel and perpendicular temperatures. In each simulation, 100 simulation ions were considered, and we followed the motion of the ions for 10^5 mean free times. The results were stored as we followed the simulation ions.

Figure II.2 shows the O⁺ velocity distribution f_i for the density ratio ($n_i/n_n = 10^{-5}$) for different values of electric field intensity [$E = 0, 50, 100$, and 150 (mV/m)]. For this density ratio, we basically have reproduced the results of Barakat *et al.* [1983], who assumed that the effect of ion-ion collisions is negligible (i.e., the ion density is very small). For example, we found that for $E = 0$ (mV/m), f_i is Maxwellian and the ion temperature is equal to the neutral temperature because of ion-neutral collisions. As the

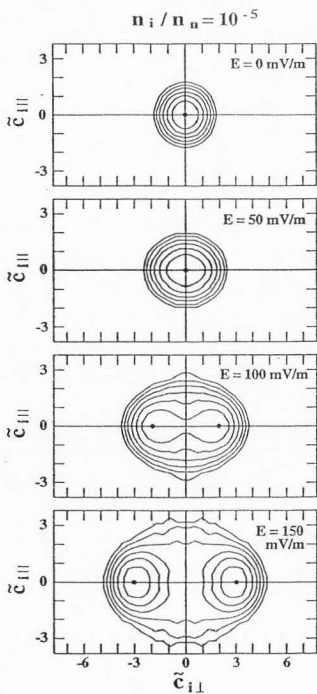


Fig. II.2. Contours of the O^+ velocity distribution function in the principal velocity plane parallel to the magnetic field \mathbf{B} for an O^+ -to- O density ratio equal to 10^{-5} and for different values of the electrostatic field E (0, 50, 100, and 150 mV/m). Typical ionospheric conditions were used in the calculations ($T_n = 1000$ K, and $B = 0.5$ G). The contours are plotted against the normalized random velocity $\tilde{c}_i [\equiv (v_i - v_D) / (2kT_n / m_n)^{1/2}]$. The contour levels decrease by a factor of $e^{1/2}$ from the maximum shown by the dot.

electric field increases, it drives the ions through the neutrals at a higher speed. Ion heating then occurs in the perpendicular direction with respect to the magnetic field. This explains the bi-Maxwellian shape of f_i for intermediate values of E (~ 50 mV/m). For $E = 100$ (mV/m) the toroidal features start to appear; there are two maxima, and they are off the center. For $E = 150$ (mV/m), the toroidal features are well pronounced. These toroidal features appear because of the combined action of the Lorentz force and collisions with neutrals, which tend to deplete the number of ions at the $\mathbf{E} \times \mathbf{B}$ drift point in the velocity distribution [Winkler *et al.*, 1992].

As the density ratio increases (i.e., $n_i/n_n = 10^{-4}$), ion-ion collisions have to be taken into account. Ion self-collisions act to isotropize the ion velocity distribution function, by transferring thermal energy from the perpendicular direction to the parallel direction. In other words, the effect of ion-ion collisions is to reduce the effect of the electric field. Therefore, if we do not include ion-ion collisions, we overestimate the effect of the electric field. The ion-ion collisions effect can be seen in Figure II.3, where the anisotropy of the distribution function is decreased. For example, when $E = 50$ (mV/m), f_i is close to Maxwellian, while in the previous corresponding case (Figure II.2) f_i is bi-Maxwellian. When $E = 100$ (mV/m), the toroidal features are less pronounced, while for $E = 150$ (mV/m) they are clearly visible (i.e., ion-ion collisions are not dominant).

At higher altitudes (see Figure II.1), the density ratio reaches a significant level ($n_i/n_n = 10^{-3}$), and ion-ion collisions dominate ion-neutral collisions. For that density ratio, Figure II.4 shows the ion velocity distribution. For $E = 0$ and 50 (mV/m), f_i is Maxwellian. For $E = 100$ (mV/m), f_i is bi-Maxwellian, while in the corresponding cases in Figure II.2 and Figure II.3 f_i has toroidal features. For $E = 150$ (mV/m), the toroidal features are still there, but they are less pronounced.

If we look at the O^+ velocity distribution (Figures II.2, II.3, and II.4), we see that as the electric field increases, the ion velocity distribution function broadens, which means

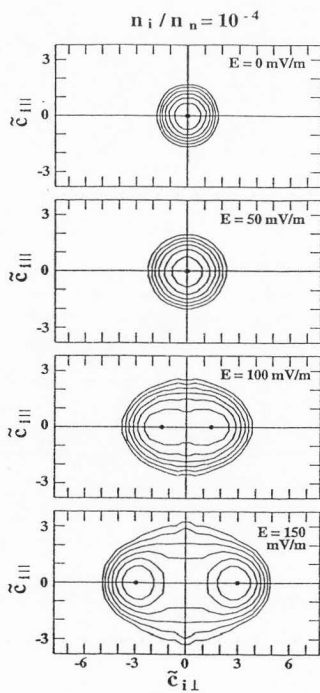


Fig. II.3. Contours of the O^+ velocity distribution function in the principal velocity plane parallel to the magnetic field \mathbf{B} for an O^+ -to- O density ratio equal to 10^{-4} . The other parameters and the plotting format are the same as those for Figure II.2.

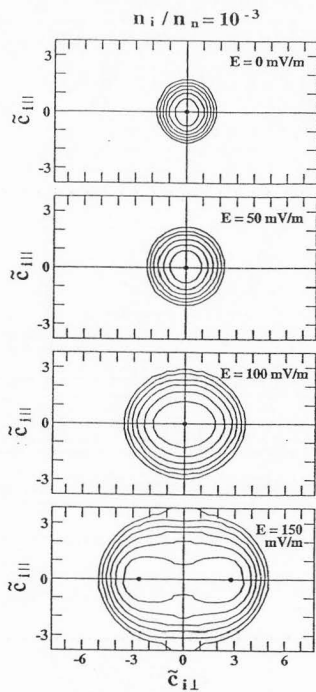


Fig. II.4. Contours of the O^+ velocity distribution function in the principal velocity plane parallel to the magnetic field B for an O^+ -to- O density ratio equal to 10^{-3} . The other parameters and the plotting format are the same as those for Figure II.2.

the ion temperature is increasing. Consequently, the ion-ion collision frequency ν_{ii} decreases [Schunk, 1977]. Therefore, we can point out that as the electric field increases, the role of ion-ion collisions is less important.

Now, we discuss the perpendicular and parallel temperatures of the O^+ ions. These two temperatures are given by the 2nd moments of f_i ,

$$T_{i\perp} = \frac{m_i}{2n_i k} \int d^3v_i v_{i\perp}^2 f_i \quad (8)$$

$$T_{i\parallel} = \frac{m_i}{n_i k} \int d^3v_i v_{i\parallel}^2 f_i \quad (9)$$

Figure II.5 shows the perpendicular temperature $T_{i\perp}$ (top), the parallel temperature $T_{i\parallel}$ (middle), and the anisotropy $T_{i\perp}/T_{i\parallel}$ (bottom) versus the electric field for different ion-to-neutral density ratios. In practice, we need to follow the test ions for several ion-neutral collision periods to allow for the transfer of energy between the ions and neutrals. However, in the limit of $n_i/n_n \rightarrow \infty$, the number of ion self-collisions is much higher than the number of ion-neutral collisions. This means that for this limit, the Monte Carlo simulation should be run for an extremely large number of ion-ion collisions, which requires too much computational resources. However, for this limit f_i is very close to Maxwellian, for which analytical results can be obtained. The analytical expressions are presented in the appendix and they were used to plot the corresponding curves in Figure II.5.

As we mentioned before, the effect of the electric field is to drive the ions through the neutrals at the $\mathbf{E} \times \mathbf{B}$ drift velocity. Because of this, the ion heating in the perpendicular direction increases (i.e., the perpendicular temperature increases). Also, the parallel temperature increases as the electric field increases, but at a slower rate than the perpendicular temperature.

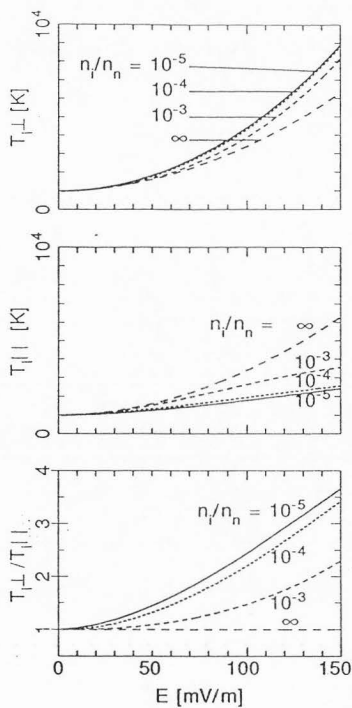


Fig. II.5. Variation of the O^+ temperature characteristics with the electric field E and the O^+ -to- O density ratio. The panels show the O^+ perpendicular temperature T_{\perp} (top), parallel temperature T_{\parallel} (middle), and temperature anisotropy T_{\perp}/T_{\parallel} (bottom). The curves are for $n_i/n_n = 10^{-5}$ (solid), 10^{-4} (dotted), 10^{-3} (short dash), and ∞ (long dash).

As the density ratio increases (Figure II.5), the role of ion-ion collisions increases. Ion-ion collisions transfer energy from the perpendicular to the parallel direction (i.e., the perpendicular temperature decreases while the parallel temperature increases). When the density ratio becomes very large ($n_i/n_n \rightarrow \infty$), the asymptotic behavior of the parallel and perpendicular temperatures are the same. In other words, this means that the distribution function f_i is Maxwellian, i.e., the ion temperature is isotropized by the ion-ion collisions. Figure II.5 (bottom) shows the anisotropy $T_{i\perp}/T_{i\parallel}$ of the ion velocity distribution function versus the electric field for different values of the density ratio. The anisotropy increases with increasing electric field because the total temperature increases with the electric field, and therefore, the ion-ion collision frequency ν_{ii} decreases while the ion-neutral collision frequency ν_{in} increases. The anisotropy decreases with increasing density ratio because of ion-ion collisions which act to isotropize the temperature and the distribution function. When the density ratio is very large, the anisotropy becomes equal to 1.0, (i.e., $T_{i\parallel} = T_{i\perp}$).

4. COMPARISON WITH OTHER WORK

In this section, we compare the results of our study with two other studies: *Tereshchenko et al.* [1991] (hereafter referred to as TTK) and *Kinzelin and Hubert* [1992] (hereafter referred to as KH). Both of these studies are analytical and both are based on simple collision models. They used two different collisional models in solving Boltzmann's equation. In TTK, a pure BGK collisional model was used. They found that the ion velocity distribution consists of two parts. The first part describes the non-Maxwellian behavior and its contribution depends on ν_{in} (ion-neutral collision frequency). The second part has Maxwellian form and its contribution depends on ν_{ii} (ion-ion collision frequency). The ν_{in} and ν_{ii} were derived using Maxwellian distributions in the TTK study [*Schunk and Nagy*, 1980]. In KH, the two collision frequencies ν_{in} and ν_{ii} are called

v_{in}^{\max} and v_{ii}^{\max} , respectively. In this study, a modified BGK collision model was used. They found that the ion velocity distribution is a linear combination of two contributions; the first is Maxwellian and the second is toroidal. The coefficients of this linear combination depend on the two collision frequencies ν_{in} and ν_{ii} . The values of ν_{in} and ν_{ii} were calculated in a consistent manner with the adopted toroidal distribution, not a Maxwellian. In our work, as we mentioned earlier, we used a realistic collision model (resonance charge exchange, polarization interaction, and Coulomb collision) in solving the Boltzmann equation. The results of our work (ion velocity distribution and the ion temperature) are more accurate than TTK and KH because we assumed a more realistic collision model.

For the comparison of our work and the work of TTK and KH, we calculated the parallel ($T_{i\parallel}$), the perpendicular ($T_{i\perp}$), and the total (T_i) temperature of oxygen ions. The expressions for these temperatures are given in TTK by equations (19), (20), and (21), respectively, in KH by equations (55a), (55b), and (9), respectively, and in our work by equations (8), (9) and $[(T_{i\parallel} + 2T_{i\perp})/3]$, respectively. We calculated $T_{i\parallel}$, $T_{i\perp}$ and T_i in the three studies at low and high altitudes by using the conditions given in Table 2 of KH (i.e., O^+ -density, O -density, and normalized effective electric field $D' = c(E/B)/\sqrt{2kT_n/m_n}$). Also, we assumed that the ion drift velocity in the parallel direction is zero. The results of this comparison are given in Figure II.6 (low altitude) and Figure II.7 (high altitude). The behavior of $T_{i\perp}$ at low altitudes (Figure II.6, top panel) shows an excellent agreement between our results (solid line) and the results of KH (dotted line). This is because both studies used a realistic collisional model (RCE and polarization interaction) for ion-neutral collisions, and because ion-ion collisions can be neglected at low altitudes. This collisional model converts part of the energy gained in the perpendicular direction to the parallel direction. The behavior of $T_{i\perp}$ in TTK (dashed line) is different from the other studies; $T_{i\perp}$ is higher in the TTK study. This is because the

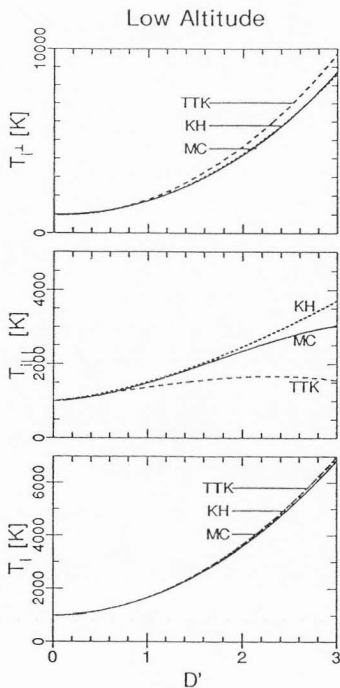


Fig. II.6. Comparison of the ion temperature characteristics at low altitude for three different studies; namely *Tereshchenko et al.* [1991] (TTK), *Kinzelin and Hubert* [1992] (KH), and our Monte Carlo simulation (MC). The panels show $T_{i\perp}$ (top), $T_{i\parallel}$ (middle), and T_i (bottom) for a wide range of the normalized effective electric field [$D' = c(E/B)/(2kT_n/m_n)^{1/2}$].

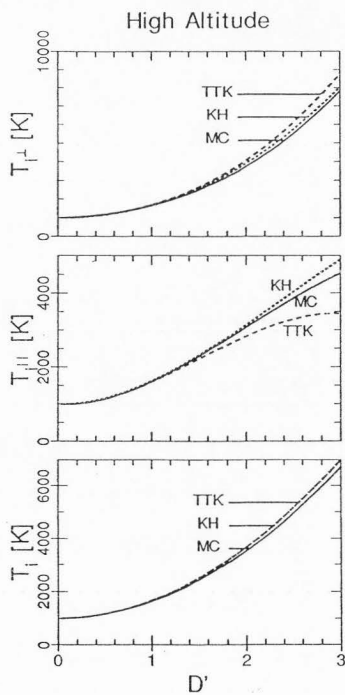


Fig. II.7. Comparison of the ion temperature characteristics at high altitude for three different studies. The format is the same as in Figure II.6.

collisional model in TTK is a BGK model which does not convert energy from the perpendicular direction to the parallel direction. Therefore, by applying this collisional model they overestimated the effect of the electric field on $T_{i\perp}$ and underestimated that effect on $T_{i\parallel}$ as shown in Figure II.6 (top and middle panels). The behavior of $T_{i\parallel}$ (middle panel) in our study and KH is related to the behavior of $T_{i\perp}$ via the collisional model. As the $T_{i\perp}$ increases due to the electric field, $T_{i\parallel}$ increases, while $T_{i\parallel}$ in TTK is less than our results and the results of KH because it did not gain energy from the perpendicular direction, as noted earlier.

It is worthwhile to point out that $T_{i\parallel}$ in TTK increases for low electric fields and decreases at high electric field. This can be explained as follows. As the electric field increases, the perpendicular temperature increases. This reduces the effect of ion-ion collisions, which transfer energy from the perpendicular to the parallel direction. This effect did not appear in our study at the given values of D' , but it will appear at higher D' . It did not appear in KH because they assumed the effect of the polarization interaction and RCE is constant; they used constant values for the ion temperature partition coefficients (β_{\parallel} and β_{\perp}).

The variation of the total ion temperature T_i with the normalized effective electric field D' is given in the bottom panel of Figure II.6. The results of TTK and KH are the same, because T_i has the same analytical form in both studies. This form is independent of ion-ion and ion-neutral collisions; it depends only on the normalized effective electric field D' . The numerical values for T_i in our study are always less than those obtained in the other two studies. This can be explained with the following argument. The O^+ ions are heated due to friction with neutral O and this heating rate is proportional to the O^+ -O momentum-transfer collision frequency ν_{in}^M . Also, the O^+ ions lose energy to the less energetic neutrals at a rate proportional to the O^+ -O energy-transfer collision frequency

v_{in}^e . The value of T_i is decided by the balance between these two factors, and hence it can be shown that

$$T_i = T_n \left[1 + (2 v_{in}^M) / (3 v_{in}^e) D'^2 \right] \quad (10)$$

For our more rigorous collision model, the faster ions collide with the neutrals more frequently than the slower ones, and hence it can be shown that the ratio v_{in}^M / v_{in}^e is less than unity. Therefore, our value of T_i is lower than those predicted by TTK and KH, where the probability of a collision between an ion-neutral pair was assumed to be independent of their relative speed g . In these studies, $v_{in}^M = v_{in}^e$.

Figure II.7 shows the values of O^+ temperature at high altitudes, where ion-ion collisions are very important and cannot be neglected. The top panel of Figure II.7 shows the variation of $T_{i\perp}$ with D' . This variation is similar to the corresponding case in Figure II.6, but the numerical values of $T_{i\perp}$ at high altitudes are less than at low altitudes because of ion-ion collisions which transfer energy from the perpendicular direction to the parallel direction. The difference between our work and KH is minimal, but it is pronounced with TTK, especially at higher D' . This is because the transfer of energy in our work and KH is due both to ion-ion collisions and to polarization interactions, while in TTK it is only due to ion-ion collisions. This makes the transfer of energy in TTK less than the other two studies. On the other hand, the parallel temperature (middle panel) increases at high altitudes because of ion-ion collisions. The results obtained for $T_{i\parallel}$ from TTK are closer to our results and KH than the corresponding case in Figure II.6. In TTK, external expressions for v_{in} and v_{ii} were used, which were derived from a local Maxwellian, while in KH the ion velocity distribution function was assumed to be a linear combination of two contributions; the first is Maxwellian and the second is toroidal. However, at high altitudes the toroidal features disappear because of ion-ion collisions and the distribution function becomes close to Maxwellian. In this case, the derived forms of v_{ii} and v_{in} in KH are close to those used in TTK, as confirmed by Table 2 in KH. Therefore, the

difference between TTK and KH at high altitudes is due to the inclusion of the polarization interaction, which acts in concert with ion-ion collisions in transferring energy from the perpendicular to the parallel direction. Since the models of TTK and KH give identical expressions for T_i , which are independent of v_{ij}/v_{in} , the profiles of T_i are the same for both models and, as shown in Figures II.6 and II.7 (bottom), they are also independent of altitude. In contrast, in our model v_{ij}/v_{in} depends on the shape of f_i and, therefore, the profiles of T_i vary with altitude.

5. CONCLUSION

The velocity distribution function of the ions in the high-latitude F-region was studied with a special attention given to the role of ion self-collisions. A Monte Carlo simulation was used that included the effect of crossed electric and magnetic fields and O⁺ collisions with a uniform background of atomic oxygen. Relatively sophisticated collision models were adopted, and, therefore, more realistic results were obtained. The O⁺ velocity distribution and the corresponding parallel and perpendicular temperatures were calculated for a wide range of ion-to-neutral density ratios n_i/n_n . We found that:

1. For the case of ($n_i/n_n = 10^{-5}$) the effect of ion self collisions is negligible and the distributions we obtained are very similar to those of *Barakat et al.* [1983].
2. As the n_i/n_n ratio increases, the role of ion self collisions becomes more apparent. The temperature anisotropy decreases and the toroidal features of the distribution become less pronounced.
3. For relatively large values of n_i/n_n (10^{-3}), ion self-collisions become dominant and the toroidal features only appear for very large values of E (≥ 150 mV/m).
4. The increase of E increases the non-Maxwellian features of f_i for two reasons. First, the interplay between the $\mathbf{E} \times \mathbf{B}$ -drift and ion-neutral collisions is the reason for creating the toroidal features in the first place [*Barakat et al.*, 1983].

Second, as E increases T_i increases, which acts to increase the ion-neutral collision frequency and decrease the ion-ion collision frequency. This results in a net reduction in the isotropizing effect of the ion self-collisions.

We also compared our results to the previous literature (TTK and KH) to assess the effect of simplified collision models on the results. The comparison showed the following:

1. The results of KH were closer to our more realistic Monte Carlo results than were those of TTK. This is because the latter used a simplified collision frequency that was consistent with the phenomenological distribution function they adopted.
2. In general, TTK overestimated $T_{i\perp}$ and underestimated $T_{i\parallel}$, because their model neglected the polarization component of the ion-neutral collision, which acts to couple $T_{i\parallel}$ and $T_{i\perp}$.
3. The deviation between the Monte Carlo results and those of the other two models increases at low altitudes and for large E because ion-neutral collisions dominated under these circumstances.
4. Both papers (TTK and KH) overestimated T_i as a result of adopting simplified collision models (BGK) for which the momentum and energy transfer collision frequencies are equal ($\nu_m^M = \nu_m^E$).

A close study of the ion distribution function shows that there are significant differences between f_i calculated by TTK and KH and those predicted by the Monte Carlo simulation. These differences can be very significant when interpreting measurements from incoherent scattering radars and retarding potential analyzers. Such problems require the use of realistic collision models that can describe the behavior of ions in a quantitative (rather than a qualitative) manner.

APPENDIX

Here we derive the asymptotic behavior of the O^+ ion temperature in the limit when $n_i/n_n \rightarrow \infty$. In this limit, f_i becomes Maxwellian, ($T_{i\parallel} = T_{i\perp} = T_i$). However, the value of T_i depends on the characteristics of the $O^+ - O$ collision process.

The energy equation for a Maxwellian ion drifting in its parent atom with a relative drift velocity v_D reduces to [Tanenbaum, 1967]:

$$\delta Q_{i0} = C \int d^3x \exp [-(x - \epsilon)^2] S_{in}^{(1)} \mathbf{G}(\mathbf{x}) \cdot \mathbf{x} \quad (\text{A1})$$

where C is a constant, $\mathbf{x} = \mathbf{g} / a_o$, $\epsilon = v_D / a_o$, $a_o^2 = 2k(T_i + T_n) / m_i$ and;

$$S_{in}^{(1)} = 2\pi \int dbb(1 - \cos \chi) \quad (\text{A2})$$

$$\mathbf{G}(\mathbf{x}) = (2k / m_i a_o)(T_n - T_i)(\mathbf{x} - \epsilon) + a_o \epsilon \quad (\text{A3})$$

Solving the above equations for T_i we get;

$$T_i = T_n + (I_1 / I_2)(T_i + T_n)\epsilon \quad (\text{A4})$$

where

$$I_1 = \int d^3x \exp [-(x - \epsilon)^2] S_{in}^{(1)} x x_{\parallel} \quad (\text{A5})$$

$$I_2 = \int d^3x \exp [-(x - \epsilon)^2] S_{in}^{(1)} (x^2 - x x_{\parallel} \epsilon) \quad (\text{A6})$$

$$S_{in}^{(1)} = \max(\sigma_p, 2Q_E) \quad (\text{A7})$$

This set of equations is implicit in T_i , which can be solved by iteration.

REFERENCES

- Barakat, A. R., and D. Hubert, Comparison of Monte Carlo simulations and polynomial expansions of auroral non-Maxwellian distributions, 2, The 1-D representation, *Ann. Geophys.*, 8, 697-704, 1990.
- Barakat, A. R., D. Hubert, and J.-P. St.-Maurice, Generating a synthetic incoherent scattering radar spectrum using a Monte Carlo simulation, *EOS*, 71, 1503, 1990.
- Barakat, A. R., and R. W. Schunk, Comparison of transport equations based on Maxwellian and bi-Maxwellian distributions for anisotropic plasmas, *J. Phys. D: Appl. Phys.*, 15, 1195-1216, 1982.
- Barakat, A. R., R. W. Schunk, and J.-P. St.-Maurice, Monte Carlo calculations of the O⁺ velocity distribution in the auroral ionosphere, *J. Geophys. Res.*, 88, 3237-3241, 1983.
- Barghouthi, A. I., A. R. Barakat, and R. W. Schunk, Effect of ion self-collisions on the non-Maxwellian ion velocity distribution in the high latitude F-region, *EOS*, 72, 365, 1991.
- Cole, K. D., Atmospheric excitation and ionization by ions in strong auroral and man-made electric fields, *J. Atmos. Terr. Phys.*, 33, 1241-1249, 1971.
- Elssamadisy, A. E., A. R. Barakat, and H.-D. Cheng, A study of incoherent radar spectrum using neural network techniques, *EOS*, 73, 414, 1992.
- Hubert, D., Auroral ion velocity distribution function: Generalized polynomial solution of Boltzmann's equation, *Planet. Space Sci.*, 31, 119-127, 1983.
- Hubert, D., Auroral ion distribution function of the E-region, *Planet. Space Sci.*, 32, 1061-1067, 1984a.
- Hubert, D., Non-Maxwellian velocity distribution functions and incoherent scattering of radar waves in the auroral ionosphere, *J. Atmos. Terr. Phys.*, 46, 601-611, 1984b.

- Hubert, D., N. Bonnard, C. Lathuillere, and W. Kofmann, A new scenario for the measurement of the auroral plasma parameters in the non-Maxwellian state, *Geophys. Res., Lett.*, in press, 1993.
- Kinzelin E., and D. Hubert, Ion velocity distribution function in the upper auroral F region. 1. Phenomenological approach, *J. Geophys. Res.*, 97, 4061, 1992.
- Knof, H., E. A. Mason, and J. T. Vanderlice, Interaction energies, charge exchange cross sections and diffusion cross sections for $N^+ - N$ and $O^+ - O$ collisions, *J. Chem. Phys.*, 40, 3548-3553, 1964.
- Lockwood, M., B. J. I. Bromage, R. B. Horne, J.-P. St.-Maurice, D. M. Willis, and S. W. H. Cowley, Non-Maxwellian ion velocity distributions observed using EISCAT, *Geophys. Res. Lett.*, 14, 111-114, 1987.
- Perraut, S., A. Brekke, M. Baron, and D. Hubert, EISCAT measurements of ion temperatures which indicate non-isotropic ion velocity distributions, *J. Atmos. Terr. Phys.*, 46, 531-543, 1984.
- Raman, R. S. V., J.-P. St.-Maurice, and R. S. B. Ong, Incoherent scattering of radar waves in the auroral ionosphere, *J. Geophys. Res.*, 86, 4751-4762, 1981.
- Schunk, R. W., Mathematical structure of transport equations for multispecies flows, *Rev. Geophys. Space Phys.*, 15, 429, 1977.
- Schunk, R. W., and A. F. Nagy, Ionospheres of the terrestrial planets, *Rev. Geophys.*, 18, 813, 1980.
- Schunk, R. W., W. J. Raitt, and P. M. Banks, Effect of electric fields on the daytime high-latitude E and F regions, *J. Geophys. Res.*, 80, 3121-3130, 1975.
- Schunk, R. W., and J. C. G. Walker, Ion velocity distributions in the auroral ionosphere, *Planet. Space Sci.*, 20, 2175-2191, 1972.
- St.-Maurice, J.-P., and R. W. Schunk, Auroral ion velocity distributions using a relaxation model, *Planet. Space Sci.*, 21, 1115-1130, 1973.

- St.-Maurice, J.-P., and R. W. Schunk, Use of generalized orthogonal polynomial solutions of Boltzmann's equation in certain aeronomy problems: Auroral ion velocity distributions, *J. Geophys. Res.*, *81*, 2145-2154, 1976.
- St.-Maurice, J.-P., and R. W. Schunk, Ion velocity distributions in the high-latitude ionosphere, *Rev. Geophys. Space Phys.*, *17*, 99-133, 1979.
- St.-Maurice, J.-P., W. B. Hanson, and J. C. G. Walker, Retarding potential analyzer measurement of the effect of ion-neutral collisions on the ion velocity distribution in the auroral ionosphere, *J. Geophys. Res.*, *81*, 5438-5446, 1976.
- Takisuki, T., and H. Abe, A binary collision model for plasma simulation with a particle code, *J. Comp. Physics*, *25*, 205, 1977.
- Tanenbaum, B. P., *Plasma Physics, Physical and Quantum Electronic Series*, McGraw-Hill, New York, 1967.
- Tereshchenko, V. D., E. D. Tereshchenko, and H. Kohl, The incoherent scattering of radio waves in a non-Maxwellian plasma: The effects of Coulomb collisions, *J. Geophys. Res.*, *96*, 17,591-17,598, 1991.
- Winkler, E., J.-P. St.-Maurice, and A. R. Barakat, Results from improved Monte Carlo calculations of auroral ion velocity distributions, *J. Geophys. Res.*, *97*, 8399, 1992.
- Winsor, K. J., G. O. L. Jones, and P. J. S. Williams, A quantitative study of the high-latitude ionospheric trough using EISCAT's common programs, *J. Atmos. Terr. Phys.*, *48*, 893-904, 1986.

CHAPTER III

MONTE CARLO STUDY OF THE TRANSITION REGION IN THE
POLAR WIND: AN IMPROVED COLLISION MODEL¹

ABSTRACT

A Monte Carlo simulation was used to study the steady-state flow of the polar wind protons through a background of O^+ ions. The simulation region included a collision-dominated region (barosphere), a collisionless region (exosphere), and the transition layer embedded between these two regions. Special attention was given to using an accurate collision model, i.e., the Fokker-Planck expression was used to represent $H^+ - O^+$ collisions. The model also included the effects of gravity, the polarization electric field, and the divergence of the geomagnetic field. For each simulation, 10^5 particles were monitored, and the collected data were used to calculate the H^+ velocity distribution function f_{H^+} , density, drift velocity, parallel and perpendicular temperatures, and heat fluxes for parallel and perpendicular energies at different altitudes. The transition region plays a pivotal role in the behavior of the H^+ flow. First, the shape of the distribution function is very close to a slowly drifting Maxwellian in the barosphere, while a "kidney bean" shape prevails in the exosphere. In the transition region, the shape of f_{H^+} changes in a complicated and rapid manner from Maxwellian to kidney bean. Second, the flow changes from subsonic (in the barosphere) to supersonic (in the exosphere) within the transition region. Third, the H^+ parallel and perpendicular temperatures increase with altitude in the barosphere due to frictional heating, while they decrease with altitude in the exosphere due to adiabatic cooling. Both temperatures reach their maximum values in the

¹ Coauthored by A. R. Barakat and R. W. Schunk. *Journal of Geophysical Research*, 1993. Published by the American Geophysical Union. Reprinted by permission.

exosphere due to adiabatic cooling. Both temperatures reach their maximum values in the transition region. Fourth, the heat fluxes of the parallel and perpendicular energies are positive and increase with altitude in the barosphere, and they change rapidly from their maximum (positive) values to their minimum (negative) values within the transition region. The results of this simulation were compared with those found in previous work in which a simple (Maxwell-molecule) collision model was adopted. It was found that the choice of the collision model can alter the results significantly. The effect of the body forces was also investigated. It was found that they can also alter the results significantly. Both the body forces and collision model have a large effect on the heat flux, while they have only a small quantitative effect on the lower-order moments (density, drift velocity, and temperature).

1. INTRODUCTION

For more than two decades, the polar wind plasma outflow received a great deal of interest. Figure III.1 shows a schematic representation of the different collision regimes of the ion flow in the polar wind. There are two main regions: (1) the collision-dominated region (ion-barosphere), where the ions behave like a fluid; and (2) the collisionless region (ion-exosphere) where the individual-particle characteristics dominate the ion motion. These two regions are separated by a narrow transition layer, where the ion behavior changes rapidly from collision-dominated to collisionless.

In the late 1960s, a large number of models were developed to study the behavior of the polar wind plasma. For instance, hydrodynamic [Banks and Holzer, 1968, 1969a, b; Raitt *et al.*, 1975; Singh and Schunk, 1985; Gombosi *et al.*, 1985] and hydromagnetic [Holzer *et al.*, 1971] models, generalized transport [Schunk and Watkins, 1981, 1982], kinetic [Lemaire, 1972; Lemaire and Scherer, 1970, 1973], and semi-kinetic [Barakat and Schunk, 1983, 1984] models were used. However, all these models had some

limitations, especially near the transition region. The results of the fluid-like (e.g., hydrodynamic) models are reliable in the barosphere only, while the results of the collisionless (e.g., kinetic, semikinetic, and hydromagnetic) models are valid in the exosphere only. Although the generalized transport models are promising in the barosphere and the exosphere, their validity in the transition region has not yet been established.

In the transition region, a more rigorous mathematical approach should be used [Lemaire, 1972]. Barakat and Lemaire [1990] used a Monte Carlo simulation to study the flow of a minor species through a major one. The gravitational force was simulated with a critical escape velocity (v_c) and the Lorentz force was ignored. They investigated the effects of the major-to-minor species mass ratio, the adopted interparticle collision model (hard-sphere and Maxwell-molecule), and the value of the escape velocity (v_c) on the flow of the minor species.

Barakat *et al.* [1990] modified the Monte Carlo simulation in order to study the H^+ flow in the polar wind over an altitude range that includes the collision-dominated, the collisionless, and the transition regions. The effects of gravity, polarization electric field, diverging magnetic field, and $H^+ - O^+$ collisions were considered. However, they used a simplified collision model (Maxwell-molecule). They concluded that inside the transition region the H^+ flow changes from subsonic to supersonic, and the H^+ parallel and perpendicular temperatures attain their maxima. The heat flux was found to be negative at all altitudes with a minimum occurring in the transition region. In the collisionless and transition regions, the H^+ distribution function took the form of a kidney bean embedded in a Maxwellian.

Barghouthi *et al.* [1990] used an improved collision model (Fokker-Planck representation for Coulomb collisions) in order to study the same problem mentioned above. They found that the adopted collision model can have a large effect on the results.

Later, *Wilson* [1992] used a hybrid fluid/particle-in-cell model with a collision model that approximates the Fokker-Planck term. He confirmed the results of *Barghouthi et al.* [1990]. Here, we present an augmentation of the presentation of *Barghouthi et al.* [1990], with the emphasis on the effect of the collision model on the distribution function and its moments.

2. THEORETICAL FORMULATION

In this work we will study the proton motion in the polar wind. At all altitudes considered here, O^+ is assumed to be the dominant ion, which enables us to neglect H^+ self-collisions compared to H^+-O^+ collisions. The validity of the assumptions used here and their effect on the results will be discussed later. We will follow the motion of H^+ from the barosphere, through the transition layer, and into the exosphere, as shown in Figure III. 1.

Neglecting H^+ self-collisions, the H^+ distribution function (f_{H^+}) is governed by the Boltzmann equation [cf. *Schunk*, 1977],

$$\frac{\partial f_{H^+}}{\partial t} + \mathbf{v}_{H^+} \cdot \nabla f_{H^+} + \left[\mathbf{G} + \frac{e_{H^+}}{m_{H^+}} \left(\mathbf{E} + \frac{1}{c} \mathbf{v}_{H^+} \times \mathbf{B} \right) \right] \cdot \nabla_{\mathbf{v}_{H^+}} f_{H^+} = \int d\mathbf{v}_{O^+} d\Omega g \sigma(g, \chi) \left[f'_{H^+} f'_{O^+} - f_{H^+} f_{O^+} \right] \quad (1)$$

where \mathbf{v} is the velocity, \mathbf{G} is the gravitational acceleration, e and m are the charge and mass, respectively, \mathbf{E} and \mathbf{B} are the electric and magnetic fields, c is the speed of light, $\mathbf{g} [\equiv \mathbf{v}_{H^+} - \mathbf{v}_{O^+}]$ is the relative velocity, $\Omega [= (\phi, \chi)]$ is the solid angle, σ is the differential scattering cross section, and χ is the scattering angle. The primes denote quantities evaluated after collision. The subscripts H^+ , O^+ , and e denote quantities related to hydrogen ions, oxygen ions, and electrons, respectively.

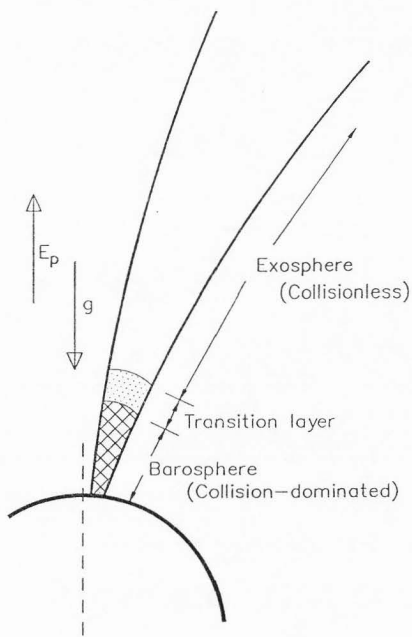


Fig. III.1. A schematic diagram for the flow of the polar wind plasma along diverging geomagnetic field lines. The different regimes of the ion flow are shown; namely, the barosphere where collision-dominated conditions prevail, the exosphere where collisionless conditions prevail, and the transition region embedded in between.

The O^+ ions are assumed to be in static equilibrium and, consequently, their distribution function f_{O^+} is assumed to have a local Maxwellian distribution that depends on the altitude z .

$$f_{O^+}(z, \mathbf{v}_{O^+}) = n_{O^+}(z) f_{O^+}^{(M)}(\mathbf{v}_{O^+}) \quad (2)$$

where

$$f_{O^+}^{(M)}(\mathbf{v}_{O^+}) = \left[\frac{m_{O^+}}{2\pi kT_{O^+}} \right]^{3/2} \exp\left(-\frac{m_{O^+} v_{O^+}^2}{2kT_{O^+}} \right) \quad (3)$$

In equations (2) and (3), n is the number density, k is the Boltzmann constant, and T is the temperature. A typical profile of the O^+ density was adopted from Appendix B of *Banks and Kockarts* [1973].

In this study the effects of gravity, polarization electric field, diverging magnetic field, and $H^+ - O^+$ collisions are taken into account. We assumed that the electrons obey the Boltzmann distribution. Both the electrons and O^+ ions were assumed to be isothermal and have equal temperatures ($T_{O^+} = T_e = 2500$ K). Finally, the magnetic field \mathbf{B} was assumed to be radial. The gravitational potential energy is given by

$$\Phi_g = -\gamma m_{H^+} M_E / r \quad (4)$$

where γ is the gravitational constant, M_E is the Earth mass, and r is the geocentric distance. The polarization electric field is given by

$$eE_p = -\partial\Phi_p / \partial r \quad (5)$$

where

$$\Phi_p = kT_e \ln(n_e) + \text{const.} \quad (6)$$

Using the above mentioned conditions, we can reduce the steady state Boltzmann equation to

$$\begin{aligned}
 v_{H^+ \parallel} (\partial f_{H^+} / \partial z) + (1/m_{H^+}) \{ -[\partial(\Phi_g + \Phi_p) / \partial z] \mathbf{e}_z + \\
 (\mathbf{e}_{H^+} / c) \mathbf{v}_{H^+} \times \mathbf{B} \} \cdot \nabla v_{H^+} f_{H^+} = \\
 n_{O^+}(z) \int d\mathbf{v}_{O^+} d\Omega g \sigma(g, \chi) \left[f'_{H^+} f_{O^+}^{(M)} - f_{H^+} f_{O^+}^{(M)} \right] \quad (7)
 \end{aligned}$$

where \mathbf{e}_z is a unit vector in the vertical direction. By using a simple change of variables similar to the one given by *Barakat and Lemaire* [1990], the above equation can be expressed in terms of a distance that is normalized with respect to the H^+ mean-free-path (mfp),

$$\tilde{z} = \int_z^\infty dz' v(z') / v_{th} \quad (8)$$

$$v_{th} = [2kT_{O^+} / m_{H^+}]^{1/2} \quad (9)$$

where v is the $H^+ - O^+$ momentum-transfer collision frequency given by *Schunk* [1977]. The resulting transformed equation represents the diffusion of H^+ through a semi-infinite homogeneous background of O^+ (with the proper adjustments of the gravitational and Lorentz forces taken into account). It is worthwhile to point out that the normalization mentioned above depends on the adopted O^+ density profile. The normalized results are general as long as O^+ is the dominant ion.

In this study we adopted a realistic collision model (Coulomb collision) to simulate $H^+ - O^+$ collisions. This model is more suitable than the collision models used in the previous works [e.g., *Barakat et al.*, 1990; *Wilson et al.*, 1992]. A comparison of the different collision models, and the sensitivity of the results to the adopted collision model, will be discussed later. The Coulomb force between H^+ and O^+ is inversely proportional to the square of the interparticle distance. For such a long-range interaction, the collision term reduces to the well-known Fokker-Planck form [*Hinton*, 1983]

$$\text{collision term} = -\frac{\partial}{\partial \mathbf{v}_{H^+}} \cdot [\mathbf{A}_{H^+} f_{H^+} - \frac{1}{2} \frac{\partial}{\partial \mathbf{v}_{H^+}} \cdot (\mathbf{D}_{H^+} f_{H^+})] \quad (10)$$

where \mathbf{A}_{H^+} is the friction coefficient and \mathbf{D}_{H^+} is the diffusion coefficient tensor given by

$$\mathbf{D}_{H^+} = D_{H^+ \parallel} \mathbf{e}_z \mathbf{e}_z + D_{H^+ \perp} (\mathbf{I} - \mathbf{e}_z \mathbf{e}_z) \quad (11)$$

The expressions for \mathbf{A}_{H^+} , $D_{H^+ \parallel}$, and $D_{H^+ \perp}$ are given by *Hinton* [1983] and are not repeated here.

Equation (10) indicates that the collision process is analogous to a combination of dynamic friction (corresponding to the drag term) and diffusion (corresponding to scattering) in velocity space. This suggests the use of a Monte Carlo approach to simulate the collision effect.

3. MONTE CARLO SIMULATION

Our main objective is to calculate the velocity distribution function of H^+ and its moments (e.g., drift velocity, temperature, etc.). As mentioned earlier, the H^+ ions move under the effect of gravity, electromagnetic forces, and $H^+ - O^+$ (Coulomb) collisions. The Monte Carlo simulation used here is explained in detail in previous publications [*Barakat and Schunk*, 1982a; *Barakat et al.*, 1983; *Barakat and Lemaire*, 1990]. A schematic representation of the simulation region is given in Figure III. 2. An H^+ ion is injected into the system at $\tilde{z} = 30$ with an initial velocity that is randomly generated such that it is consistent with a nondrifting Maxwellian immediately below the injection region.

The "test" H^+ ion is considered to move for a short interval of time Δt under the influence of the "effective" body force (gravitational + electrostatic + magnetostatic). The effect of Coulomb collisions (with the O^+ background) during the period Δt is

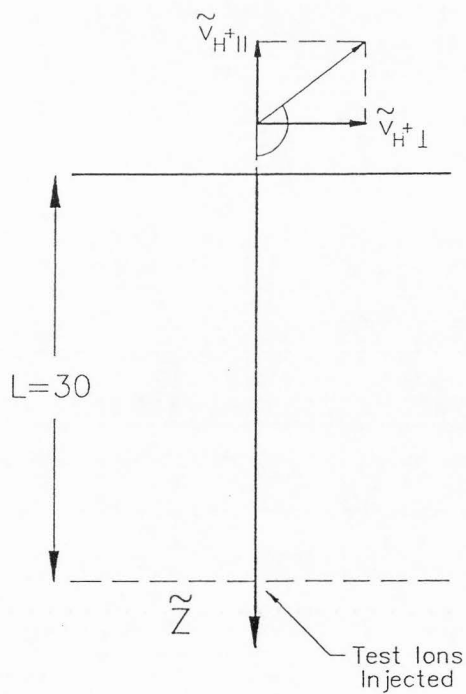


Fig. III.2. A schematic diagram of the setup for the Monte Carlo simulation.

implemented at the end of Δt . The above procedure is repeated until the test ion exits the simulation region at either end ($\tilde{z} = 0$ or $\tilde{z} = 30$), and then another test ion is initiated at the bottom. The test ions are monitored as they cross a predetermined set of altitudes $\{\tilde{z}_j\}$. At each altitude, a suitable grid is used to register their behavior. Here, we used a 2-D grid whose coordinates are the velocities parallel and perpendicular to the geomagnetic field \mathbf{B} . The symmetry in the azimuthal direction is used to simplify the registration process. The time that the test ions spend in a given velocity bin, divided by the bin's volume, is proportional to the value of the velocity distribution function (f_{H^+}) at the center of the bin. Moreover, the velocities of the test ions, as they cross one of the monitoring altitudes, can be directly used to compute the moments of the distribution function at that altitude.

The cumulative effect of Coulomb collisions during the period Δt is given by

$$\Delta \mathbf{u} = \mathbf{A}_{H^+} \Delta t \quad (12)$$

$$\langle (\Delta v_{H^+ \parallel})^2 \rangle = D_{H^+ \parallel} \Delta t \quad (13)$$

$$\langle (\Delta v_{H^+ \perp})^2 \rangle = 2D_{H^+ \perp} \Delta t \quad (14)$$

where $\Delta \mathbf{u}$ is the change in the test ion velocity due to drag, and $\langle (\Delta v_{H^+ \parallel})^2 \rangle$ and $\langle (\Delta v_{H^+ \perp})^2 \rangle$ are the variances of the change in the test ion velocity due to diffusion (in velocity space) in the directions parallel and perpendicular to the original velocity \mathbf{v}_{H^+} , respectively. The Monte Carlo simulation of the Fokker-Planck collision model is discussed in detail by *Spitzer and Hart* [1971].

The time step should be chosen small enough so that the test ion velocity, and, consequently, the drag and diffusion coefficients, can be considered constant during Δt . On the other hand, the available computational resources impose limitations on how small Δt can be chosen. We tested the collision model by considering a simple case (homogeneous O^+ background with a Maxwellian velocity distribution) for which the

exact solution was known. We ran the model for this simple case for different values of Δt . The results were compared to the exact solution, and, consequently, a Δt was selected that struck a compromise between speed and accuracy. In particular, for the adopted value of Δt [= 0.01 v_{H^+}/A_{H^+}], f_{H^+} was Maxwellian with a temperature equal to that of the background O^+ to within about 1%. This indicates that the adopted simulation conserves both energy and momentum within a reasonable accuracy.

4. RESULTS

The Monte Carlo technique explained above was used to simulate the behavior of the H^+ ions. In each simulation, 10^5 test ions were monitored as they drifted across the system, and the H^+ distribution function as well as its lower-order moments were computed at different normalized altitudes \tilde{z} . Then the results were transformed back in order to be presented in terms of unnormalized altitudes (in kilometers).

In order to facilitate the understanding of the different physical mechanisms in this problem, we separated the effect of the geomagnetic field divergence from the other effects. First, we neglected the effect of the geomagnetic field divergence ($\partial B/\partial \tilde{z} = 0$). Then we compared the results with those of the simulation that included the B field dependence ($\partial B/\partial \tilde{z} \neq 0$).

4.1. *No B Field Altitude Dependence*

In this case the effective body force is simplified as $F_{eff} = -\partial(\Phi_g + \Phi_E)/\partial \tilde{z}$. This force is not constant in the simulation region. For simplicity, the simulation region was divided into 22 horizontal layers, where the total potential energy ($\Phi = \Phi_g + \Phi_E$) was approximated by a straight line in each zone. Figure III.3 shows a comparison between the exact (solid) and the approximated (dashed) profiles of Φ . The two curves are so close that they cannot be distinguished from each other within the resolution of the graph.

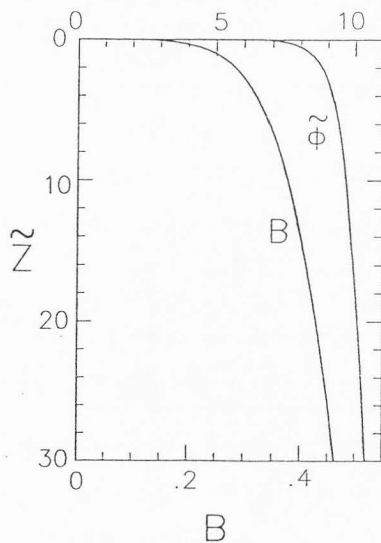


Fig. III.3. Comparison of the exact profiles (dashed) and the piecewise linear approximation (solid) adopted in the simulation for the H^+ normalized potential energy ($\tilde{\Phi} \equiv \Phi / 2kT_{O^+}$) and the magnetic field (B). The exact and approximate profiles are indistinguishable within the graph resolution.

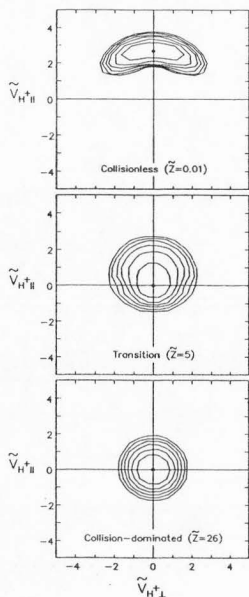


Fig. III.4. The H^+ velocity distribution function for the case of no B field altitude dependence ($\partial B / \partial \bar{z} = 0$). We considered three representative altitudes: (bottom) in the barosphere, (middle) in the transition region, and (top) in the exosphere. The distribution function f_{H^+} is represented by equal-value contours in the normalized velocity ($v_{H^+||}$, $v_{H^+\perp}$) plane, where $v_{H^+} = v_{H^+} / \sqrt{2kT_{O^+} / m_{O^+}}$. The contour levels decrease successively by a factor of $e^{1/2}$ from the maximum, which is marked by a solid circle.

Figure III.4 shows the H^+ velocity distribution function at three altitudes that correspond to different collision conditions. As a convention, the barosphere is defined to be below 650 km ($\bar{z} > 10$), the exosphere above 2500 km ($\bar{z} < 0.1$), and the transition region between 650 km and 2500 km ($0.1 < \bar{z} < 10$). In the barosphere (bottom panel), the distribution function is very close to Maxwellian, which is consistent with the assumed conditions at the injection point ($\bar{z} = 30$). As altitude increases, the H^+ distribution function becomes progressively more non-Maxwellian. The middle panel shows f_{H^+} in the transition region. The maximum of f_{H^+} remains close to the origin, while an enhanced tail appears in the upward direction. If we remember that Coulomb collisions are less effective for the faster ions, the shape of f_{H^+} can be explained as follows. The slow H^+ ions are strongly coupled (via collisions) to the nondrifting O^+ ions, and hence they cannot be easily accelerated by the upward body forces. Therefore, the peak of f_{H^+} remains close to the origin. On the other hand, the fast ions can be easily accelerated upward, creating an upward tail. The distribution function in the exosphere is given in the top panel. At high altitudes, the collisional effect is very small such that all of the H^+ ions gain upward velocities due to the dominant body force. Also, for such large velocities, the velocity diffusion in the perpendicular direction dominates ($D_{H^+\perp} \sim v_{H^+}^{-1} \gg D_{H^+\parallel} \sim v_{H^+}^{-3}$). Had $D_{H^+\perp}$ been very large, the H^+ ions would have formed a spherical shell. However, since $D_{H^+\perp}$ is relatively small compared to what is needed to form a complete shell, f_{H^+} has the shape of a spherical cap. A cross section of this cap is the "kidney bean" shape shown in the top panel of Figure III.4.

The lower-order moments were computed at different altitudes as mentioned above. Since the Boltzmann equation is linear with respect to f_{H^+} , its solution is defined within a constant factor. The H^+ density can be arbitrarily normalized such that the normalized density equals unity at a given altitude (say, 230 km). The other normalized moments are defined as follows:

$$\tilde{u}_{H^+} = [m_{H^+} / (2kT_{O^+})]^{1/2} u_{H^+} = [m_{H^+} / (2kT_{O^+})]^{1/2} \int v_{H^+ \parallel} f_{H^+} dv_{H^+} / n_{H^+} \quad (15)$$

$$\tilde{T}_{H^+ \parallel} = [m_{H^+} / (kT_{O^+})] \int (v_{H^+ \parallel} - u_{H^+})^2 f_{H^+} dv_{H^+} / n_{H^+} \quad (16)$$

$$\tilde{T}_{H^+ \perp} = [m_{H^+} / (2kT_{O^+})] \int v_{H^+ \perp}^2 f_{H^+} dv_{H^+} / n_{H^+} \quad (17)$$

$$\tilde{q}_{H^+ \parallel} = [m_{H^+} / (2kT_{O^+})]^{3/2} \int (v_{H^+ \parallel} - u_{H^+})^3 f_{H^+} dv_{H^+} / n_{H^+} \quad (18)$$

$$\tilde{q}_{H^+ \perp} = [m_{H^+} / (2kT_{O^+})]^{3/2} \int v_{H^+ \perp}^2 (v_{H^+ \parallel} - u_{H^+}) f_{H^+} dv_{H^+} / (2n_{H^+}) \quad (19)$$

In the above equations, the tilde denotes normalized quantities and \tilde{u}_{H^+} , $T_{H^+ \parallel}$, $\tilde{T}_{H^+ \perp}$, $q_{H^+ \parallel}$, and $q_{H^+ \perp}$, are the H^+ ion drift velocity, parallel temperature, perpendicular temperature, parallel heat flux, and perpendicular heat flux, respectively.

Figure III.5 shows the low-order moment profiles for H^+ ions. For clarity, two arrows were used to mark the altitudes where $\tilde{z} = 0.1$ and $\tilde{z} = 10$. As mentioned earlier, the transition region lies between the two arrows, while the barosphere lies at the bottom segment and the exosphere lies at the top segment. The drift velocity monotonically increases with altitude (top right panel). At low altitudes the effect of Coulomb collisions dominates that of the upward body force and, consequently, the drift velocity is very small. As the altitude increases, the effect of the body force becomes more important and the drift velocity increases. In the transition region, the velocity increases more rapidly and the flow changes from subsonic to supersonic. In the exosphere, the velocity continues to increase with altitude and asymptotically approaches an upper limit of

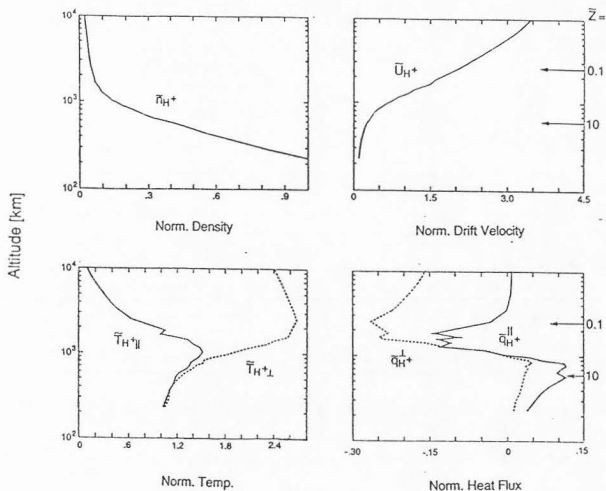


Fig. III.5. Altitude profiles of the different H⁺ moments for the case of no B field altitude dependence ($\partial B / \partial \bar{z} = 0$). The normalized moments considered here are (top left) density \bar{n}_{H^+} , (top right) drift velocity \bar{u}_{H^+} , (bottom left) parallel $\bar{T}_{H^+||}$ and perpendicular $\bar{T}_{H^+⊥}$ temperatures, and (bottom right) the parallel $\bar{q}_{H^+||}$ and perpendicular $\bar{q}_{H^+⊥}$ heat fluxes. The two arrows indicate the boundaries between the barosphere, the transition region, and the exosphere.

$\tilde{u}_{H^+} \sim 5$. We found that (in general) the H^+ ion flow crosses its sonic point, and its velocity gradient attains a maximum, in the transition region.

The fact that the ion flow changes from subsonic to supersonic inside the transition region can be understood if we remember the following two facts. First, for subsonic flow, the number of down-going ions n_d is close to the number of up-going ions n_u ($n_d \approx n_u$), while for supersonic flow we must have ($n_d \ll n_u$). Second, since the body force is always upward, only collisions can reflect the ions downwards. In the barosphere the effect of collisions is dominant, and hence we have $n_u = n_d$, which corresponds to a subsonic flow. In the exosphere, the collision effect is negligible and hence most of the particles are accelerated upward, which corresponds to a supersonic flow. Therefore, the transition from the subsonic flow (in the barosphere) to the supersonic flow (in the exosphere) must occur at some altitude inside the transition region.

The fact that the maximum velocity gradient occurs in the transition region is due to the balance between the body force and the drag force due to collisions with the O^+ ions. In the barosphere the drag force decreases exponentially with altitude (due to the exponential decrease of n_{O^+}) and hence the velocity gradient increases with altitude. On the other hand, the upward H^+ acceleration decreases with altitude in the exosphere due to the decrease in the body force (collisions are negligible). Therefore, an inflection point (maximum $\partial \tilde{u}_{H^+} / \partial z$) has to occur within the transition region.

The top left panel shows the H^+ density profile. The density scale height in the barosphere is much smaller than its value in the exosphere. The transition between the two trends shows as a "knee" in the transition region.

The profiles of the H^+ parallel ($T_{H^+||}$) and perpendicular ($T_{H^+\perp}$) temperatures are given in the bottom left panel. Deep in the barosphere, the H^+ temperature is isotropic and equal to the background O^+ temperature ($\tilde{T}_{H^+||} \approx \tilde{T}_{H^+\perp} \approx 1$) due to the strong collisional coupling between H^+ and O^+ . As altitude increases, the ion drift velocity increases and

hence both $\bar{T}_{H+\parallel}$ and $\bar{T}_{H+\perp}$ increase due to frictional heating with the background O^+ gas. In the transition region, $\bar{T}_{H+\parallel}$ reaches a maximum and then decreases due to "parallel adiabatic cooling" until it asymptotically reaches a value of about 0.1 at the top of the exosphere. According to this process (parallel adiabatic cooling), the parallel velocity dispersion of the ion population should decrease as it is accelerated adiabatically in the parallel direction. In contrast, the perpendicular temperature remains almost constant in the exosphere due to the neglect of the effect of the diverging geomagnetic field lines.

The bottom right panel of Figure III.5 shows the profiles of the heat fluxes for the parallel ($q_{H+\parallel}^{\parallel}$) and perpendicular ($q_{H+\perp}^{\perp}$) energies. In the barosphere, both heat fluxes are positive and increase with altitude. This behavior can be explained using an approach similar to that given in the appendix of *Barakat and Lemaire* [1990], in which we expand the 16-moment equations [*Barakat and Schunk*, 1982*b*] in the collision-dominated limit. In the transition region, both $q_{H+\parallel}^{\parallel}$ and $q_{H+\perp}^{\perp}$ change rapidly from a (positive) maximum to a (negative) minimum; then they increase monotonically with altitude as the flow gets deeper into the exosphere. The negative values of the heat fluxes in the exosphere are consistent with the "kidney bean" shape of the distribution function.

4.2. Effect of B Field Altitude Dependence

We then included the effect of diverging field lines on the results. In particular, we used the conservation of total ion energy (kinetic + potential) and the first adiabatic invariant ($v_{H+\perp}^2/B$) to compute the changes in the test ion's velocity between collisions. For computational convenience, the profile of B was approximated in a similar way to that of Φ . Figure III. 3 shows the excellent agreement between the exact profile and the piecewise linear approximation.

The results of the simulation with $\partial B/\partial z$ included are present in Figures III.6 and III.7. Comparing Figures III.6 and III.7 with the corresponding ones with no B field altitude dependence (Figures III.4 and III.5), we notice that

1. The results of the two cases are not significantly different in the low-altitude region. This is because in this region the divergence of the magnetic field is dominated by the other factors (e.g., collisions, body forces, etc.).

2. The effect of the diverging magnetic field becomes significant at high altitudes. Above 2000 km, the perpendicular temperature decreases rapidly with altitude and eventually becomes less than the parallel temperature. Also, the heat flux of the perpendicular energy decreases in a similar fashion. These two features are due to the dominance of the perpendicular adiabatic cooling.

3. The effect of the diverging magnetic field is such that \mathbf{v}_{H^+} rotates towards the direction of \mathbf{B} . This makes the H^+ distribution function at high altitudes (Figure III.6, top panel) closer to a bi-Maxwellian than the corresponding results for the case of $\partial B/\partial z = 0$.

4.3. *Effect of Collision Model and Body Forces*

It is a common practice to adopt some simplified assumptions in order to facilitate the numerical computations. For example, simplified collision models were used [e.g., Barakat and Lemaire, 1990; Barakat et al., 1990; Gombosi and Rasmussen, 1991; Wilson, 1992; I. A. Barghouthi, A. R. Barakat, and R. W. Schunk, The effect of self collision on the O^+ velocity distribution of auroral F-region, submitted to *Journal of Geophysical Research*, 1993, hereafter referred to as Barghouthi et al., 1993], and body forces were neglected [e.g., Barakat and Lemaire, 1990]. In order to illustrate the effect of these assumptions, we compared the above results with those of two other cases. In the first case, a "Maxwell molecule" collision model was adopted instead of the correct (Coulomb) collision model (case I), while all the other conditions (e.g., total collision

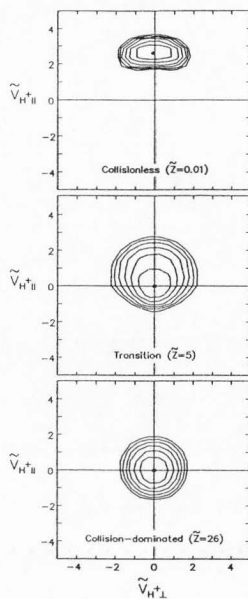


Fig. III.6. The H^+ velocity distribution function for the case when the B field altitude dependence is included ($\partial B / \partial \tilde{z} \neq 0$). We considered three representative altitudes: (bottom) in the barosphere, (middle) in the transition region, and (top) in the exosphere. The format is similar to that of Figure III.4.

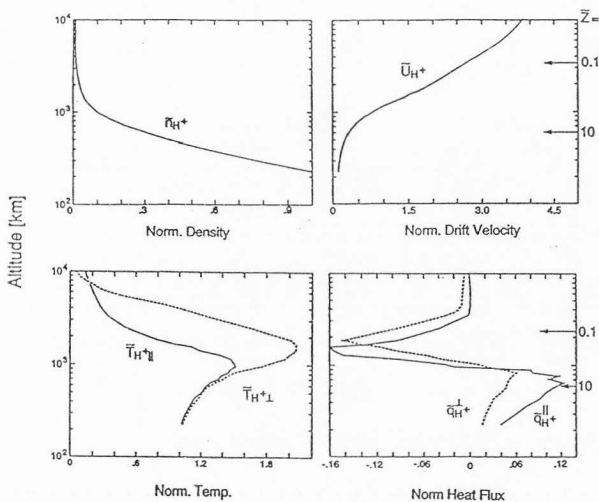


Fig. III.7. Altitude profiles of the different H^+ moments for the case when the B field altitude dependence is included ($\partial B / \partial z \neq 0$). The format is similar to that of Figure III.5.

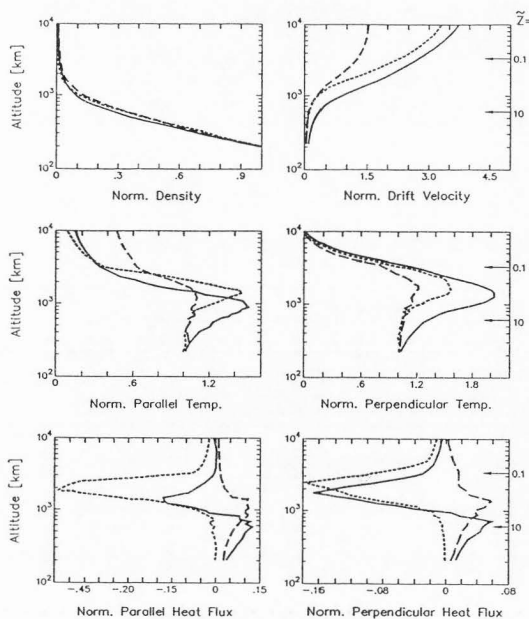


Fig. III.8. Comparison of the H^+ moments for three cases: Coulomb collision with body forces (solid), Maxwell molecule collision with body forces (dotted), and Coulomb collision without body forces (dashed). The normalized moments considered here are (top left) density, (top right) drift velocity, (middle left) parallel temperature, (middle right) perpendicular temperature, (bottom left) parallel heat flux, and (bottom right) perpendicular heat flux. In all cases the effect of B field altitude dependence is included.

frequency, body forces, etc.) were kept the same. In the second case (II), the body forces were turned off.

Figure III.8 shows a comparison of the moment profiles for the three cases. We notice that the normalized density profile is not too sensitive to the collision model nor to the body forces (top left panel). The top-right panel shows that the adoption of the Maxwell molecule collision model results in the reduction of the H^+ drift velocity. This reduction is due to the fact that for the Maxwell molecule collision model the heat flow does not contribute to the momentum equation, and hence the mobility is increased [see *Schunk*, 1977]. We notice that the reduction factor decreases at higher altitudes due to the reduced contribution of the collision term in the momentum equation. The absence of the (upward) body forces (case II) results in a reduction of the drift velocity at all altitudes.

The profiles of $T_{H^+ \parallel}$ (middle left) and $T_{H^+ \perp}$ (middle right) indicate that the adoption of a Maxwell molecule collision model changes the temperature profiles in a quantitative (rather than qualitative) manner. The absence of body forces results in a reduction in the drift velocity (as mentioned above), and hence both the frictional heating at low altitude and the parallel adiabatic cooling at high altitudes are reduced. Therefore, the peak of the temperature is greatly reduced and the limit of $T_{H^+ \parallel}$ at high altitudes is enhanced in the absence of body forces.

The profiles of the parallel (bottom left) and perpendicular (bottom right) heat fluxes indicate that the heat flux has the same direction at all altitudes both for the Maxwell molecule collision model (downward) and for Coulomb collisions in the absence of the body forces (upward), with a single maximum within the transition region. These cases are qualitatively different from the case that includes Coulomb collisions and body forces. In general, the adoption of simplified assumptions (such as those studied above) has only a quantitative effect on the lower-order moments (such as density and drift velocity), but it has a large qualitative effect on the higher-order moments (such as heat fluxes).

5. CONCLUSION

We have used a Monte Carlo simulation to study the steady-state flow of the H^+ ions through an O^+ background in the polar wind. The simulation region included the barosphere (collision-dominated region), the exosphere (collisionless region), and the transition region. The effects of polarization electric field, gravitational force, diverging geomagnetic field, and $H^+ - O^+$ collisions were taken into consideration. A special attention was paid to using an accurate collision model. We used a Coulomb collision model (Fokker-Planck form) for the $H^+ - O^+$ interparticle interaction. This collision model is more accurate than those used in previous simulations of similar problems.

We previously discussed the effect of adopting a Maxwell molecule collision model on the results. In reality, we want to use the Coulomb collision model. A convenient approximation to Coulomb collisions was introduced by *Takizuka and Abe* [1977], which was used by *Wilson* [1992] and by *Barghouthi et al.* [1993]. The basic idea is to replace the "real" particles by a smaller (yet large) number of "simulation" particles, with the collision differential cross section adjusted accordingly. It can be shown that the collision term reduces to the Fokker-Planck form as the number of simulation particles tends to infinity. However, more investigations are needed to assess the error resulting from using a relatively small number of such particles. *Wilson* [1992] tried to test the approach by applying it to a spatially uniform ion population with a given initial velocity distribution. He found that the distribution function became Maxwellian in about 10 collision periods. However, this test is not sufficient to determine if the collision model accurately represents the Coulomb collision. In fact, this test can be passed by any elastic collision with a differential cross section that depends only on the magnitude of the relative velocity of the colliding particles $|\mathbf{v}_2 - \mathbf{v}_1|$ (such as Maxwell molecule, hard sphere, etc.).

Each of our simulations used 10^5 test ions to compute the ion distribution function at different altitudes. We also computed the profiles of H^+ normalized density (\bar{n}_{H^+}), drift

velocity (\bar{u}_{H^+}), parallel and perpendicular temperatures ($\bar{T}_{H^+||}$ and $\bar{T}_{H^+\perp}$), and the heat fluxes for the parallel and perpendicular energies $q_{H^+||}$ and $q_{H^+\perp}$. At low altitudes, f_{H^+} is close to Maxwellian with a small drift velocity, while f_{H^+} takes the shape of a "kidney bean" in the exosphere. In the transition region, the H^+ distribution changes rapidly from one shape to the other.

We found that the flow changes from subsonic (in the barosphere) to supersonic (in the exosphere) with the sonic point occurring in the transition region. The H^+ parallel and perpendicular temperatures attain their maxima in the transition region as a result of the competition between frictional heating (which dominates in the barosphere) and adiabatic cooling (which dominates in the exosphere). Finally, both heat flux components $q_{H^+||}$ and $q_{H^+\perp}$ are positive and increase with altitude in the barosphere, which is consistent with the moment equation approach. In the transition region, $q_{H^+||}$ and $q_{H^+\perp}$ change very rapidly from positive maxima to negative minima, and then they start to increase with altitude in the transition region and the exosphere.

The adopted collision model was shown to have a significant effect on the shape of the H^+ distribution function, especially in the transition region. Although the choice of the collision model influenced the low-order moments (density, drift velocity, parallel and perpendicular temperatures) in a quantitative manner only, it had a more significant (qualitative) influence on the higher-order moments (heat fluxes).

The model used here included some assumptions that must be considered in the interpretation of the results. First, the H^+ ions were considered to be minor, which enabled us to neglect both H^+ self-collisions and the H^+ density compared to the O^+ density ($n_e = n_{O^+}$). Some modeling studies [e.g., Cannata and Gombosi, 1989] indicate that this may be the case at all altitudes on open field lines. If the (lighter) H^+ ions become major, the density scale height increases, and hence the polarization electric field is reduced. This will act to reduce the drift velocity and the parallel adiabatic cooling at high

altitudes. Second, we neglected ion-neutral collisions, which is valid above about 400 km. The major effect of including H^+ -neutral collisions is that we would get negative heat fluxes $\bar{q}_{H^+}^{\parallel}$ and $\bar{q}_{H^+}^{\perp}$ at low altitudes ($\ll 400$ km), where they dominate the other collisions [see Barakat *et al.*, 1990]. Finally, if H^+ self-collisions become significant at high altitudes, we expect the results to be modified accordingly. In particular, the non-Maxwellian H^+ features will be reduced, the temperature anisotropy will approach unity, and the heat flux will be reduced. In contrast, self-collisions should have a small effect (if any) on the density, drift velocity, and total temperature.

REFERENCES

- Banks, P. M., and T. E. Holzer, The polar wind, *J. Geophys. Res.*, **73**, 6846–6854, 1968.
- Banks, P. M., and T. E. Holzer, Features of plasma transport in the upper atmosphere, *J. Geophys. Res.*, **74**, 6304–6316, 1969a.
- Banks, P. M., and T. E. Holzer, High-latitude plasma transport: The polar wind, *J. Geophys. Res.*, **74**, 6317–6332, 1969b.
- Banks, P. M., and G. Kockarts, *Aeronomy*, Academic, San Diego, Calif., 1973.
- Barakat, A. R., and J. Lemaire, Monte Carlo study of the escape of a minor species, *Phys. Rev. A, Gen. Phys.*, **42**, 3291–3302, 1990.
- Barakat, A. R., and R. W. Schunk, Comparison of Maxwellian and bi-Maxwellian expansions with Monte Carlo simulations for anisotropic plasmas, *J. Phys. D*, **15**, 2189–2203, 1982a.
- Barakat, A. R., and R. W. Schunk, Transport equations for multicomponent anisotropic space plasmas, *Plasma Phys.*, **24**, 389–418, 1982b.
- Barakat, A. R., and R. W. Schunk, O^+ ions in the polar wind, *J. Geophys. Res.*, **88**, 7887–7894, 1983.

- Barakat, A. R., and R. W. Schunk, Effect of hot electrons on the polar wind, *J. Geophys. Res.*, 89, 9771-9783, 1984.
- Barakat, A. R., R. W. Schunk, and J.-P. St.-Maurice, Monte Carlo calculations of the O⁺ velocity distribution in the auroral ionosphere, *J. Geophys. Res.*, 88, 3237-3241, 1983.
- Barakat, A. R., R. W. Schunk, I. A. Barghouthi, and J. Lemaire, Monte Carlo study of the transition from collision-dominated to collisionless polar wind flow, in *Physics of Space Plasmas*, edited by T. Chang, G. B. Crew, and J. R. Jaspers, pp. 431-437, Scientific Publisher, Cambridge, Mass., 1990.
- Barghouthi, I. A., A. R. Barakat, R. W. Schunk, and J. Lemaire, H⁺ outflow in the polar wind: A Monte Carlo simulation (abstract), *EoS Trans. AGU*, 71, 1493, 1990.
- Cannata, R. W., and T. I. Gombosi, Modeling the solar cycle dependence of quiet-time ion upwelling at high geomagnetic latitudes, *Geophys. Res. Lett.*, 16, 1141-1144, 1989.
- Gombosi, T. I., and C. E. Rasmussen, The transport of gyration-dominated space plasmas of thermal origin, 1, Generalized transport equations, *J. Geophys. Res.*, 96, 7759-7778, 1991.
- Gombosi, T. I., T. E. Cravens, and A. F. Nagy, A time-dependent theoretical model of the polar wind: Preliminary results, *Geophys. Res. Lett.*, 12, 167-170, 1985.
- Hinton, F. L., Collisional transport in plasma, in *Basic Plasma Physics I*, edited by A. A. Galeev and R. N. Sudan, pp. 147-197, North-Holland, New York, 1983.
- Holzer, T. E., J. A. Fedder, and P. M. Banks, A comparison of kinetic and hydrodynamic models of an expanding ion-exosphere, *J. Geophys. Res.*, 76, 2453-2468, 1971.
- Lemaire, J., O⁺, H⁺, and He⁺ ion distributions in a new polar wind model, *J. Atmos. Terr. Phys.*, 34, 1647-1658, 1972.

- Lemaire, J., and M. Scherer, Model of the polar ion-exosphere, *Planet. Space Sci.*, 18, 103-120, 1970.
- Lemaire, J., and M. Scherer, Kinetic models of the solar and polar winds, *Rev. Geophys.*, 11, 427-468, 1973.
- Raitt, W. J., R. W. Schunk, and P. M. Banks, A comparison of the temperature and density structure in high and low speed thermal proton flows, *Planet. Space Sci.*, 23, 1103-1117, 1975.
- Schunk, R. W., Mathematical structure of transport equations for multispecies flows, *Rev. Geophys.*, 15, 429-445, 1977.
- Schunk, R. W., and D. S. Watkins, Electron temperature anisotropy in the polar wind, *J. Geophys. Res.*, 86, 91-102, 1981.
- Schunk, R. W., and D. S. Watkins, Proton temperature anisotropy in the polar wind, *J. Geophys. Res.*, 87, 171-180, 1982.
- Singh, N., and R. W. Schunk, Temporal evolution of density perturbations in the polar wind, *J. Geophys. Res.*, 90, 6487-6496, 1985.
- Spitzer, L., Jr., and M. H. Hart, Random gravitational encounters and the evolution of spherical systems, 1, Method, *Astrophys. J.*, 164, 399-409, 1971.
- Takizuka, T., and H. Abe, A binary collision model for plasma simulation with particle code, *J. Comput. Phys.*, 25, 205-219, 1977.
- Wilson, G. R., Semi-kinetic modeling of the outflow of ionospheric plasma through transition region, *J. Geophys. Res.*, 97, 10551-10565, 1992.
- Wilson, G. R., J. L. Horwitz, and J. Lin, A semikinetic model for early stage plasmasphere refilling, 1, Effect of Coulomb collisions, *J. Geophys. Res.*, 97, 1109-1119, 1992.

CHAPTER IV
EFFECTS OF ALTITUDE-DEPENDENT WAVE PARTICLE
INTERACTIONS ON THE POLAR WIND PLASMA¹

ABSTRACT

The effect of wave-particle interactions on the outflow characteristics of polar wind plasma was investigated. The theoretical model included gravitational acceleration (g), polarization electrostatic field (Ep), and divergence of the geomagnetic field. Within the simulation region (1.7 to 10 R_e) the ions were assumed to be collisionless and the electrons to obey Boltzmann relation. Profiles of altitude-dependent diffusion coefficients [$D_{\perp}(O^+)$ and $D_{\perp}(H^+)$] were computed from the wave spectral density S observed by the Plasma Wave Instrument (PWI) on board DE-1. The effect of PWI was introduced via a Monte Carlo technique, and an interactive approach was used to converge to reach self-consistent results. The main conclusions of this study were the following. As a result of perpendicular heating, the temperature anisotropy (T_{\parallel}/T_{\perp}) was reduced and even reversed ($T_{\parallel} < T_{\perp}$) at high altitudes. The O^+ velocity distribution function developed a conic shape at high altitudes. The altitudes above which the PWI influences the O^+ ions were lower than those for the H^+ ions. The escape flux of O^+ could be enhanced by more than an order of magnitude while the H^+ flux remains constant. The O^+ ions are heated more efficiently than the H^+ ions, especially at low altitudes due to the "pressure cooker" effect. As the ions are heated and move to higher altitudes, the ion's Larmor radius a_L may become comparable to the perpendicular wave length λ_{\perp} . As the ratio a_L/λ_{\perp} becomes ≥ 1 , the heating rate becomes self-limited and the ion distribution displays toroidal

¹ Coauthored by A. R. Barakat and A. M. Persoon.

features. This result is consistent with the observation of O^+ toroidal distribution at high altitude ionosphere. Finally, the large variability in the wave spectral density S was studied. This variability was found to change our results only in a quantitative manner, while our conclusions remained qualitatively unchanged.

1 Introduction

The polar wind is the ambi-polar flow of plasma along "open" field lines originating in the polar cap region. It is generally accepted that the polar wind plays an important role in ionosphere-magnetosphere coupling via mass and energy transfer. The ionosphere plays an important role in supplying the magnetospheric ions, especially O^+ (Chappel *et al.*, 1987), which was observed with significant abundance in the magnetosphere. On the other hand, the magnetosphere provides the "demand" on ionospheric ions (Barakat *et al.*, 1987). Therefore, the proper modeling of the polar wind is crucial to understanding the ionosphere-magnetosphere coupling.

Several models were developed to simulate the behavior of the polar wind plasma, including hydrodynamic, hydromagnetic, generalized transport, kinetic, and semi-kinetic models. Detailed review of these models and the "classical" picture of the polar wind were given by Schunk (1988). A semi-kinetic model was used by Barakat and Schunk (1983) to show that H^+ had a near-to-Maxwellian at low altitudes ($\sim 1.7 R_e$). As the plasma reached higher altitudes ($\gtrsim 5 R_e$), it developed large temperature anisotropy ($T_{\parallel} > T_{\perp}$) and upward heat-flow component. This classical picture of the polar wind was verified observationally by Persoon *et al.* (1983) and Biddle *et al.* (1985).

In the last ten years, several nonclassical effects were included in order to study their effect on the plasma outflow. The escape flux of O^+ was found to be enhanced due to the effect of high electron temperature (Barakat and Schunk, 1983), high ion temperature (Li *et al.*, 1988), and energetic magnetospheric electrons (Barakat and Schunk, 1984). The effects of ion-acceleration at high altitudes, and of chemical and collisional $H^+ - O^+$

coupling, on the composition of the ion escape flux were investigated by Barakat *et al.* (1987). Recently, a 3-D time-dependent model was developed (Schunk and Sojka, 1989) that included the effect of horizontal drifts on the coupling between the regions above the polar cap, auroral oval, and cusp.

The wave-particle interactions (WPI) were not included in the models discussed above. However, theoretical studies (Barakat and Schunk, 1987; 1989; Chen and Ashour-Abdulla, 1990) indicated that the nonclassical polar wind could become unstable to a host of modes. Observations indicated that a significant level of electromagnetic turbulence occurred above the polar cap (Gurnett *et al.*, 1984; Gurnett and Inan, 1988). Ganguli and Palmadesso (1987) and Ganguli *et al.* (1988) used a phenomenological approach to include the WPI into the generalized transport equations in a self-consistent manner. The transcendental problem of the coupling of waves and plasma transport is global, highly nonlinear, and multi-scale in the spatial and temporal domains. This raised questions with regard to the validity of the above simple local phenomenological model, and makes the solution of the exact problem beyond the available mathematical and technical capabilities. A possible way to tackle this problem is to include the observed wave data as an input to the theoretical model.

The effects of WPI on the ion characteristics along auroral field lines were a subject of many theoretical studies. For instance, Chang *et al.* (1986) and Retterer *et al.* (1987) used a Monte Carlo simulation to produce O^+ conics. Remarkable agreement was found between the simulated and observed O^+ energy and shape of the distribution function. Barakat *et al.* (1993) developed an approach based on the generalized transport equations. This approach was shown to be much more efficient, and of comparable accuracy to the Monte Carlo simulations. These studies assumed that gravity and polarization electrostatic force are negligible with respect to ion energization. It can be easily shown that this is not necessarily the case, especially above the polar cap.

Barakat and Barghouthi (1994) studied the effect of WPI on the ion outflow in the polar wind. They included the effects of WPI and the body force, which were shown to be of comparable importance. However, this study was parametric in the sense that the velocity-space diffusion coefficient for H^+ and O^+ ($D_{\perp}(H^+)$ and $D_{\perp}(O^+)$) were varied systematically. Also $D_{\perp}(O^+)$ and $D_{\perp}(H^+)$ were assumed to be constant with altitude and were assigned values independent of each other. It was found that appreciable effect of WPI occurred for values of $\tilde{D}_{\perp} = [D_{\perp} R_e / v_{th}^3]$ that were comparable to or greater than unity, where R_e is the earth radius, and v_{th} is the ion's thermal speed. An O^+ temperature peak was observed to occur at low altitudes due to the "pressure cooker" effect.

In this study, we used the wave spectral density S as observed by the PWI aboard DE-1 to compute more realistic strength of WPI. This produced altitude-dependent S , and specified $D_{\perp}(O^+)$ and $D_{\perp}(H^+)$, and hence enabled us to solve simultaneously for the O^+ and H^+ ions. The chapter will be organized as follows. The theoretical model and simulation details are presented in Sections 2 and 3. The utilized data and the reduction technique are discussed in Section 4. The effect of WPI on the behavior of O^+ and H^+ ions is given in Section 5. Sections 6 and 7 are devoted to studying the effect of self limited energization due to finite ion gyroradius, and of the large uncertainty in the observed strength of WPI.

2 The Model

This work is an extension to that of Barakat and Schunk (1983) who studied the plasma outflow in the polar wind. We adopted a model based on their work after extending it to include the effect of wave-particle interactions (WPI). In this work, ions move under the effect of body forces (i.e., gravitational and polarization electrostatic) and the mirror force due to divergence of the geomagnetic field. During their motion, the ions interact with electromagnetic turbulence.

The simulation region is a magnetic tube extending from the exobase (at altitude of $r_o = 10.870$ km to about $10 R_e$ (earth radii)). We considered the steady flow of the plasma composed of electrons, hydrogen ions (H^+), and oxygen ions (O^+). The geomagnetic field was taken to be proportional to r^{-3} where r is the geocentric distance. At the top of the barosphere (i.e., just below the exobase), the ion distributions are assumed to be drifting Maxwellian for H^+ and nondrifting Maxwellian for O^+ . In the absence of wave-particle interactions, the ion motion can be described by Liouville theorem. Using that theorem, conservation of energy, conservation of the first adiabatic invariant (μ) and the ion distribution function at the boundary, we can calculate the ion velocity distribution at any point in the simulation region for a given potential energy profile ($\phi(r)$). The resulting relation can be solved simultaneously with the expression for $\phi(r)$ and the quasi-neutrality condition:

$$\phi(r) = kT_e \ell n \left(\frac{n_e}{n_{eo}} \right) + GM_E m \left(\frac{1}{r_o} - \frac{1}{r} \right) \quad (1)$$

$$n_e \equiv n(O^+) + n(H^+) \quad (2)$$

where k is Boltzmann's constant, T_e is electron temperature, n_e and n_{eo} are the electron densities at r and r_o , respectively, G is the universal gravitational constant, M_e is the mass of the earth, and m is the ion mass either H^+ or O^+ .

The effect of the interactions between the ions and the electromagnetic ion cyclotron waves can be described by the diffusion equation:

$$\frac{\partial f}{\partial t} = \left(\frac{1}{v_{\perp}} \right) \frac{\partial}{\partial v_{\perp}} \left[D_{\perp} v_{\perp} \frac{\partial f}{\partial v_{\perp}} \right] \quad (3)$$

where D_{\perp} is the quasi-linear velocity diffusion rate perpendicular to the geomagnetic field given by (Retterer *et al.* 1987);

$$D_{\perp} = \frac{\eta q^2}{4m^2} |E_x(w = \Omega)|^2 \quad (4)$$

where q and m are the ion charge and mass, respectively, Ω is the ion gyrofrequency, and w is the wave frequency, $|E_x^2|$ is the measured spectral density of the wave, and η is the proportion of the measured spectral density that corresponds to a left-hand-polarized wave. The determination of $|E_x^2|$ is given in Section 4.

3 Monte Carlo Simulation

We will use the Monte-Carlo method to solve the diffusion equation (3) to obtain the ion velocity distribution and its moments. An ion is injected into the simulation region at the lower boundary (r_o) with a random initial velocity that corresponds to the ion distribution function immediately below r_o . The generated ion is assumed to move for a short interval of time Δt under the influence of the gravitational force, polarization electrostatic force, and geomagnetic force. The effect of the wave-particle interaction during the period Δt is taken into account by perturbing the ion's perpendicular velocity by a random increment Δv_{\perp} such that:

$$\langle (\Delta v_{\perp})^2 \rangle = 4D_{\perp} \Delta t \quad (5)$$

The above procedure is repeated until the test ion exits the simulation region at either end ($r = r_o$ or $= 10 R_e$), and then another test ion is initiated at r_o . The test ions are monitored as they cross a predetermined set of altitudes (r_i). At each altitude a suitable grid in the velocity space is used to register their behavior. Besides the velocities of the test ions, as they cross one of the monitoring altitudes, can be directly used to compute the moments of the distribution function at that altitude.

The time step Δt should be infinitesimal ($\Delta t \rightarrow 0$). However, as Δt decreases, the computational time increases. In order to select an optimum value of Δt that strikes a

compromise between speed and accuracy, the simulation was repeated for successively decreasing values of Δt until the results became insensitive to the specific value of Δt .

The boundary conditions selected are similar to those of Barakat and Schunk (1983). At the lower boundary (r_o) we set the H^+ drift velocity $u(H^+)$ at 11 km/s, H^+ density $n(H^+)$ at 200 cm^{-3} , and H^+ temperature $T(H^+)$ at 3000 K. The O^+ lower boundary conditions are $u(O^+) = 0$, $n(O^+) = 100 \text{ cm}^{-3}$, and $T(O^+) = 3000 \text{ K}$.

In practice, an iterative approach was used to find the plasma outflow characteristics. First, a semi-kinetic model (Barakat and Schunk, 1983) to solve for the case of negligible WPI as a starting point. The resulting electrostatic potential was then used with the Monte Carlo simulation to find the O^+ and H^+ ions densities with the WPI included, which were substituted in equations (1) and (2) in order to compute an improved value of $\phi(r)$. The iteration process was continued until convergence was reached.

4 Wave Spectral Density

It is a formidable task to include the wave-particle interaction and the plasma transport in a self-consistent manner. First, the wave spectrum is very sensitive to the details of the ion velocity distributions of the plasma at the point where the wave is generated. Second, the saturation level of the wave depends on the nonlinear characteristics of the plasma. The wave generated at a given location can propagate to another one where it interacts with the plasma. That is, the resulting nonlinear and global problem is beyond our present technical and computational capabilities. Therefore, we use the observed wave spectral density as an input to our model.

The principal source of measured wave needed for this work is the data collected by the Plasma Wave Instrument (PWI) on board the Dynamics Explorer 1 (DE-1) spacecraft. In particular, the low frequency range of the wave spectrum (\leq ion cyclotron frequency) measured above the high latitude region is the most relevant to our study, since it interacts with the ions more efficiently. The general DE-1 microfiche data base was scanned in

order to identify the events of special interest. Four sets of spectral density were chosen in order to achieve the following objectives: (1) they cover a wide range of altitudes ($1.5 R_e$ to $4.5 R_e$); (2) they occur at polar cap latitudes; and (3) they sample both polar caps. An example of one set of data is given in Figure IV.1 (top panel). Each set was fit with a power law $|E^2| = \gamma w^\beta$. The fitted spectrum is then used to compute the quasi-linear diffusion rate perpendicular to the geomagnetic field D_\perp at the corresponding altitude. Finally, the computed value of D_\perp was fitted with a power law $\left[D_\perp = \gamma \left(\frac{r}{R_e} \right)^\delta \right]$ as shown in Figure IV.1 (lower panel). The optimum values of γ and δ were found to be $\gamma(\text{H}^+) = 9.55 \times 10^2 \text{ cm}^2/\text{s}^3$, $\delta(\text{H}^+) = 13.3$, $\gamma(\text{O}^+) = 5.77 \times 10^3 \text{ cm}^2/\text{s}^3$, and $\delta(\text{O}^+) = 7.95$.

5 Outflow Characteristics

The Monte Carlo technique explained above was used to simulate the behavior of H^+ and O^+ ions outflow under the effect of body forces, geomagnetic field, and wave-particle interaction. In each simulation 10^5 test ions were monitored as they travel across the simulation region, and H^+ and O^+ ions velocity distribution functions as well as their lower order moments were computed at different geocentric altitudes r . In the rest of this section the characteristics of H^+ and O^+ ions outflow are presented. The perpendicular wavelength (λ_\perp) of the electromagnetic turbulence is considered to be much longer than the ion Larmor radius (a_L). Under this condition the quasi-linear velocity diffusion rate D_\perp is given by equation (4).

5.1 H^+ Ions

In order to verify our model, we first implemented the simulation for the case of negligible WPI ($D_\perp(\text{H}^+) \cong 0$). The results of this simulation (left panel of Figure IV.2) are similar to the results of Barakat and Schunk (1983), who did not include the effect of

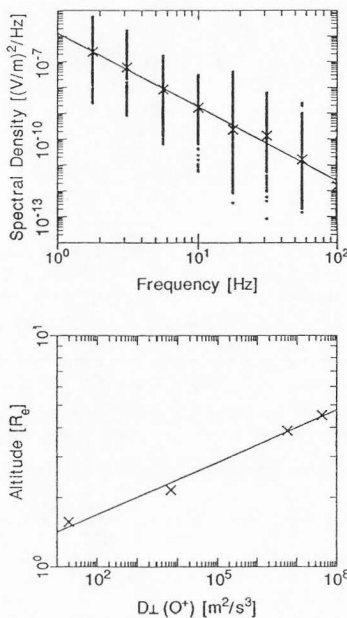


Fig. IV. 1. An example of the observed data and the reduction technique employed to compute the velocity diffusion coefficient D_{\perp} . In the top panel, the spectral densities are represented by the dots, and their (geometric) means are presented by the x's. The straight line is the best fit of these means, which is used to compute D_{\perp} for the ions. The straight line in the bottom panel is the adopted profile for $D_{\perp}(O^+)$, which best fits the values of $D_{\perp}(O^+)$ for different altitudes (marked by x's).

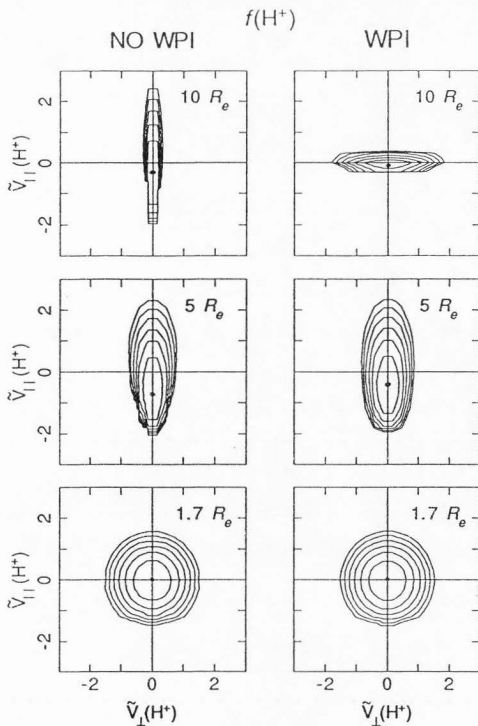


Fig. IV. 2. H^+ velocity distributions for the case of negligible WPI (left panel) and for WPI (right panel) at different geocentric altitudes. $f(H^+)$ is represented by equal-value contours in the normalized velocity $(\tilde{v}_{\parallel}, \tilde{v}_{\perp})$ plane, where $\tilde{v} = v/[2kT(H^+)/m(H^+)]^{1/2}$. The contour levels decrease successively by a factor $e^{1/2}$ from the maximum (marked by a dot).

WPI. The bottom left panel of Figure IV.2 shows the Maxwellian features of $f(H^+)$ at the exobase. As altitude increases, $f(H^+)$ develops a large temperature anisotropy [$T_{\parallel}(H^+)/T_{\perp}(H^+) > 50$], and an asymmetry with an upward tail at $10 R_e$ (top left panel). The large anisotropy is due to adiabatic cooling, which occurs as the ions drift upward and, hence, the magnetic field intensity decreases.

The right panel of Figure IV.2 shows the effect of WPI at different altitudes. At the exobase ($1.7 R_e$) $f(H^+)$ is Maxwellian, same as the case of negligible WPI, because $D_{\perp}(H^+)$ is very small at low altitude. As altitude increases, $D_{\perp}(H^+)$ increases, and then the strength of WPI increases. For example, at $5 R_e$ the anisotropy reduced, while at $10 R_e$ it inverted [$T_{\perp}(H^+) > T_{\parallel}(H^+)$]. This can be explained as follows: as H^+ ions drift upward the WPI heats the ions in the perpendicular direction. This results in increasing $T_{\perp}(H^+)$ as shown in Figure IV.3.

The lower-order moments were coupled at different altitudes as mentioned in Section 3. The moments are defined by:

$$n_i = \int f_i d^3 v_i \quad (6)$$

$$u_i = \frac{1}{n_i} \int v_{i\parallel} f_i d^3 v_i \quad (7)$$

$$T_{i\parallel} = \frac{m_i}{m_i k} \int (v_{i\parallel} - u_i)^2 f_i d^3 v_i \quad (8)$$

$$T_{i\perp} = \frac{m_i}{2n_i k} \int v_{i\perp}^2 f_i d^3 v_i \quad (9)$$

In the above equations i denotes the type of the ion (H^+ or O^+), n_i , u_i , $T_{i\parallel}$, and $T_{i\perp}$ are the ion density, drift velocity, parallel temperature, and perpendicular temperature, respectively.

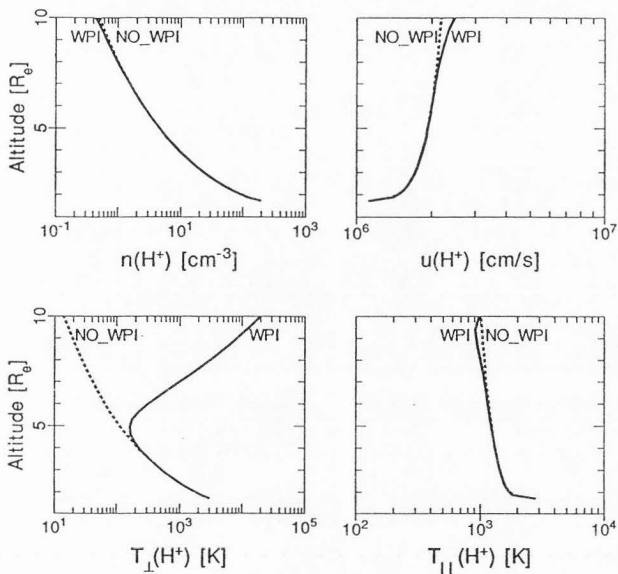


Fig. IV. 3. Altitude profiles of the lower order H^+ moments for the case of negligible WPI (dotted) and WPI (solid). The moments considered here are density $n(H^+)$ (top left), drift velocity $u(H^+)$ (top right), perpendicular temperature $T_{\perp}(H^+)$ (bottom left), and parallel temperature $T_{\parallel}(H^+)$ (bottom right).

Figure IV.3 shows the profiles of H^+ density $n(H^+)$, drift velocity $u(H^+)$, parallel temperature $T_{\parallel}(H^+)$, and perpendicular temperature $T_{\perp}(H^+)$, for two cases with (solid) and without (dotted) the effect of WPI included. Including the WPI increases the drift velocity $u(H^+)$ (top right panel), which can be explained as follows. The WPI heats the ions in the perpendicular direction, which increases the upward mirror force and, hence, accelerates the H^+ ions in the upward direction. Since the H^+ ions are in the flux-limiting flow condition, a corresponding decrease in the H^+ density $n(H^+)$ (top left panel) is expected in order to compensate for the increase in $u(H^+)$ and hence, keep the net escape flux constant.

The behavior of the perpendicular temperature $T_{\perp}(H^+)$ (bottom left panel) is a result of the competition between the heating due to WPI and the perpendicular adiabatic cooling. At low altitude, the adiabatic cooling is dominant, and, therefore, $T_{\perp}(H^+)$ decreases with altitude. However, for high altitude the WPI dominates, resulting in a rapid increase of $T_{\perp}(H^+)$. In contrast, $T_{\perp}(H^+)$ decreases monotonically due to the perpendicular adiabatic cooling.

The profiles of H^+ parallel temperature $T_{\parallel}(H^+)$ are presented in the bottom right panel of Figure IV.3 for the case with (solid) and without (dotted) WPI effect. As explained earlier, WPI heats H^+ ions in the perpendicular direction, which results in increasing $T_{\perp}(H^+)$ and $u(H^+)$. The increase in $u(H^+)$ increases the parallel adiabatic cooling, which decreases $T_{\parallel}(H^+)$. The increase of $T_{\perp}(H^+)$ is eventually transferred into the parallel direction due to the divergence of the geomagnetic field lines. The balance between these two effects determines the behavior of $T_{\parallel}(H^+)$.

5.2 O^+ Ions

We calculated the O^+ velocity distribution function at different altitudes as shown in Figure IV.4 for two cases, namely, with (right) and without (left) the effect of WPI included. For negligible WPI the results are consistent with those of Barakat and Schunk

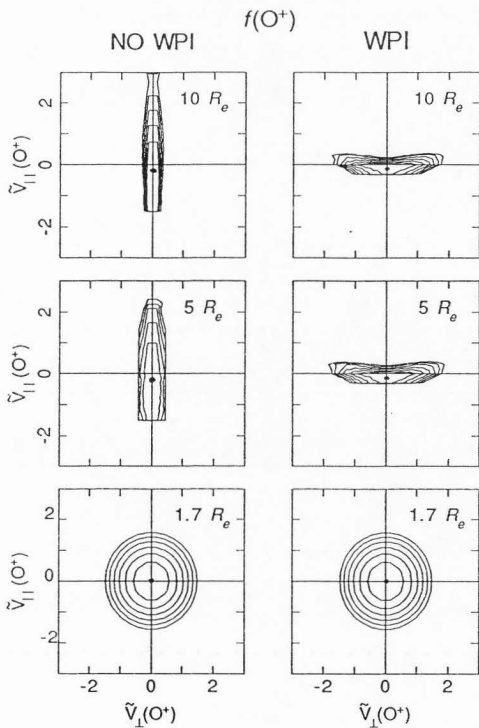


Fig. IV. 4. O^+ velocity distributions for the case of negligible WPI (left panel) and for WPI (right panel) at different geocentric distances. The format is the same as those of Figure IV.2.

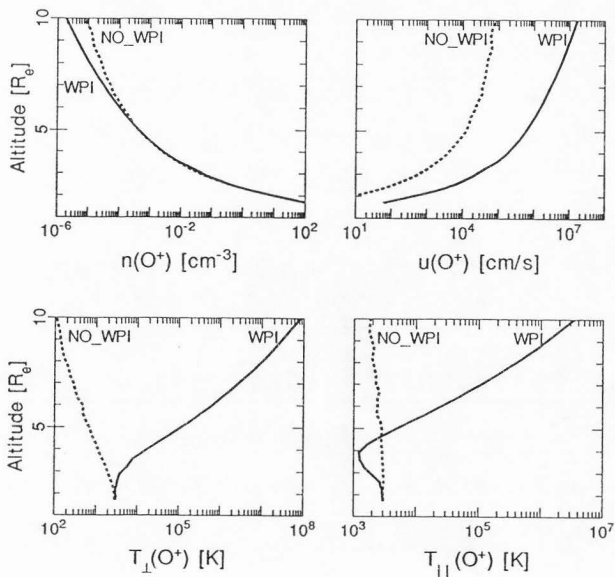


Fig. IV. 5. Altitude profiles of the lower order O⁺ moments for the case of negligible WPI (dotted) and WPI (solid). The moments considered here are density $n(\text{O}^+)$ (top left), drift velocity $u(\text{O}^+)$ (top right), perpendicular temperature $T_{\perp}(\text{O}^+)$ (bottom left), and parallel temperature $T_{\parallel}(\text{O}^+)$ (bottom right).

(1987). For example, $f(O^+)$ is Maxwellian at the exobase ($1.7 R_e$), and develops large temperature anisotropy [$T_{\parallel}(O^+) > T_{\perp}(O^+)$] and an asymmetry with an upward tail at high altitudes. The effect of WPI on $f(O^+)$ is demonstrated by the right column of Figure IV.4. At the exobase (bottom right) the WPI has a negligible effect, and consequently $f(O^+)$ remains Maxwellian. At higher altitudes, the role of WPI becomes more significant in heating the ions in the perpendicular direction. The resulting perpendicular heating leads to the formation of "pancake-like" distributions [$T_{\perp}(O^+) > T_{\parallel}(O^+)$], which folds into O^+ -conics due to the effect of diverging magnetic fields, as shown in the middle and top right panels.

The response of O^+ behavior to the introduction of WPI is significantly different from that of the H^+ behavior. There are two reasons for that difference. First, the potential function $\phi(H^+)$ for H^+ is monotonically decreasing, while $\phi(O^+)$ increases up to a large maximum value and then decreases (Barakat and Schunk, 1983). Second, the O^+ velocity diffusion coefficient [$D_{\perp}(O^+)$] exceeds that of H^+ [$D_{\perp}(H^+)$], and, therefore, O^+ is expected to be preferentially heated with respect to H^+ . This is consistent with the results of Horwitz (1984).

The effect of WPI on O^+ moments is shown in Figure IV.5. In the absence of WPI (dotted), the dominant gravitational force permits only a few particle (in velocity distribution tail) to reach to high altitudes. This explains the rapid decrease of $n(O^+)$ with altitude. However, this potential barrier acts as a velocity filter that results in an increase in $u(O^+)$, which reaches a trans-sonic speed at the peak of the potential, as noted by Barakat and Schunk (1983). In comparison, the O^+ energization due to WPI enhances the drift velocity as shown in the top right panel. The inclusion of WPI has two opposing effects on O^+ density $n(O^+)$. First, it increases the number of O^+ ions that can overcome the potential barrier and reach to higher altitudes. Second, the increase of $u(O^+)$ due to WPI tends to reduce $n(O^+)$ especially above the peak of $\phi(O^+)$. The former effect slightly

dominates at low altitudes while the latter manifests clear dominance at higher altitudes. This explains the slight increase at low altitudes and the larger increase at high altitudes of the O^+ density as a result of WPI.

An interesting fact is that the heating due to WPI dominates the perpendicular adiabatic cooling at all altitudes. As a consequence, the $T_{\perp}(O^+)$ profile (bottom left) reverses its behavior from monotonically decreasing (dotted) to monotonically increasing (solid) where the effect of WPI was included. The heating is enhanced at lower altitudes due to the "pressure cooker" effect. Briefly, this effect results from the temporary trapping of the O^+ ions between an upper gravitational and a lower magnetic deflection point. As the ion repeatedly bounces between these deflection points, it is energized to significantly higher perpendicular temperature.

The bottom right panel shows the O^+ parallel temperature $T_{\parallel}(O^+)$ for the cases with (solid) and without (dotted) WPI effect. We notice that the WPI results in net reduction of $T_{\parallel}(O^+)$ at low altitudes due to parallel adiabatic cooling, and net enhancement of $T_{\parallel}(O^+)$ at high altitudes due to the transfer of energy from the perpendicular to the parallel direction.

6 Finite Larmor Radius Effect

In the previous section, the ion Larmor radius (a_L) was assumed to be much less than the perpendicular wave length (λ_{\perp}) of electromagnetic turbulence, that is, $\lambda_{\perp} \gg a_L$. However, as an ion drift upward along a geomagnetic field line, it heats up due to WPI, and the geomagnetic field intensity B decreases. The combined effect of these two factors results in a rapid increase in a_L with altitude. At higher altitudes a_L may become comparable to or even more than λ_{\perp} , and consequently the velocity independent expression given in Equation (4) becomes inaccurate. In this section, we investigate the effect of this phenomenon on the shape of the ions distribution functions, and on the altitude profiles of the lower order moments.

A more general theory, which considers the ion orbit, was used by Curtis (1985) to derive an expression for D_{\perp} which is valid for a wide range of the ratio $\varepsilon = a_L/\lambda_{\perp}$. A close examination of that expression showed that D_{\perp} is independent of ε for $\varepsilon \ll 1$, while it tends to decrease as ε^{-3} for $\varepsilon \gg 1$. Therefore, we adopted a simple model for D_{\perp} for any value of ε , namely:

$$D_{\perp} = D_{\perp}|_{\varepsilon=0} \begin{cases} 1 & \text{for } \varepsilon \leq 1 \\ \varepsilon^{-3} & \text{for } \varepsilon \geq 1 \end{cases} \quad (10)$$

where $D_{\perp}|_{\varepsilon=0}$ is given by Equation (4).

Since the data collected by PWI do not include information about λ_{\perp} , we considered a wide range [$\lambda_{\perp} = 1, 10, \text{ and } 100 \text{ km}$] that covers the conditions expected to occur above the polar cap. Figure IV.6 shows the O^+ velocity distribution $f(O^+)$ at different altitudes and for different values of λ_{\perp} . For the case of ($\lambda_{\perp} = 100 \text{ km}$), $f(O^+)$ is similar to the case of ($\lambda_{\perp} = \infty$) up to $\sim 6 R_e$ (left column). At very high altitude ($\sim 10 R_e$) the distribution function displays toroidal features. This toroidal shape can be explained if we remember that D_{\perp} peaks near $v_{\perp} \approx 0$ and decreases rapidly for large values of v_{\perp} . Therefore, the ions tend to move out of the region of large diffusion rate ($v_{\perp} \approx 0$) and accumulate in the region of relatively low D_{\perp} , forming the aforementioned toroidal distributions. The above mechanism may explain the O^+ toroidal distribution observed by Moore *et al.* (1985).

As λ_{\perp} decreases, the ratio a_L/λ_{\perp} approaches unity at lower altitudes and consequently the toroidal shape of $f(O^+)$ appears earlier. In particular, for the case of ($\lambda_{\perp} = 10 \text{ km}$), the weak toroidal features appear at about $6 R_e$ and becomes more pronounced at $10 R_e$ (middle column). For even smaller values of λ_{\perp} (1 km), the toroidal features start to appear at about $4 R_e$, and form completely at about $6 R_e$ (left column). It is worthwhile to notice that the toroidal shape eventually saturates, that is, the general shape of $f(O^+)$ become invariable with altitude.

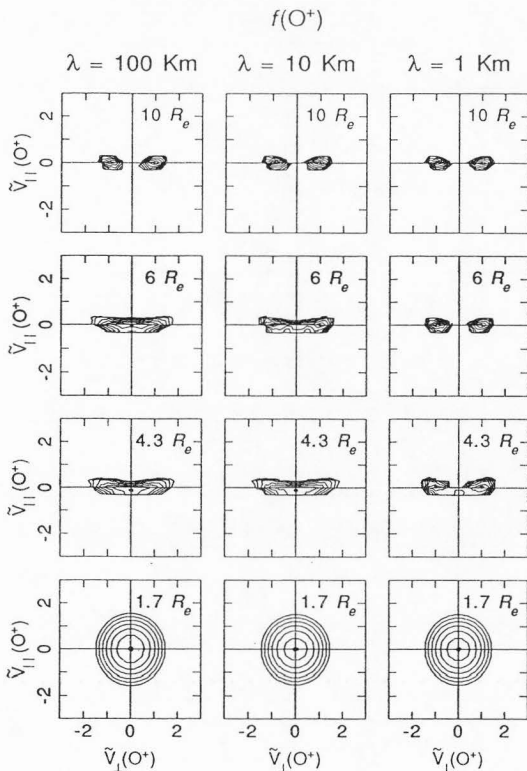


Fig. IV. 6. O^+ velocity distribution function at different geocentric distances for different EMIC-wavelengths (λ). The wavelengths considered here are $\lambda = 100 \text{ km}$ (left panel), $\lambda = 10 \text{ km}$ (middle panel), and $\lambda = 1 \text{ km}$ (right panel). The format is similar to that of Figure IV. 2.

The effect of including self-limiting heating on the O^+ low-order velocity moments is presented in Figure IV.7. Profiles for ion density $n(O^+)$, drift velocity $u(O^+)$, parallel temperature $T_{\parallel}(O^+)$, and perpendicular temperature $T_{\perp}(O^+)$ are given for $\lambda_{\perp} = \infty$ (solid), $\lambda_{\perp} = 100$ km (dotted), $\lambda_{\perp} = 10$ km (short dashes), and $\lambda_{\perp} = 1$ km (long dashes). We notice that for large values of λ_{\perp} (100 km) the role of self-limiting heating takes over at higher altitude ($\sim 8 R_e$). At that altitude the moments show a tendency towards saturation. This is consistent with the behavior of $f(O^+)$. As λ_{\perp} decreases, the ratio a_L/λ_{\perp} reaches unity, and hence the saturation point occurs at lower altitudes.

The top left panel of Figure IV.7 shows the profiles of $u(O^+)$ for different values of λ_{\perp} . At low altitudes the ratio a_L/λ_{\perp} is much less than unity, and hence the profiles of $u(O^+)$ coincide for all values of λ_{\perp} . For the case of ($\lambda_{\perp} = 100$ km), the acceleration rate and hence $u(O^+)$ are reduced above a saturation level of about $8 R_e$, in comparison to the case of ($\lambda_{\perp} = \infty$). This is an obvious result of the self limiting of energization which occurs when a_L/λ_{\perp} exceeds unity. As λ_{\perp} decreases, the relative reduction of $u(O^+)$ increases and starts at lower saturation points.

Since the ion energy is comparable to, or exceeds the potential barrier at the saturation point, the O^+ escape flux is insensitive to the conditions at higher altitudes. Therefore, O^+ density $n(O^+)$ should increase (top left panel) in order to compensate for the decrease of $u(O^+)$ noted above. As λ_{\perp} decreases, the enhancement of $n(O^+)$ increases and occurs at lower altitudes. This is consistent with the behavior of $u(O^+)$. The self-limiting heating is expected to reduce $T_{\perp}(O^+)$ (bottom left) in a direct manner. The reduction of $T_{\perp}(O^+)$ results in a corresponding reduction of $T_{\parallel}(O^+)$ due to the decrease of the energy transfer from the perpendicular to the parallel directions. In general, we notice that $T_{\parallel}(O^+)$ and $T_{\perp}(O^+)$ displays much more variation (several orders of magnitude) with λ_{\perp} than $n(O^+)$ and $u(O^+)$ do.

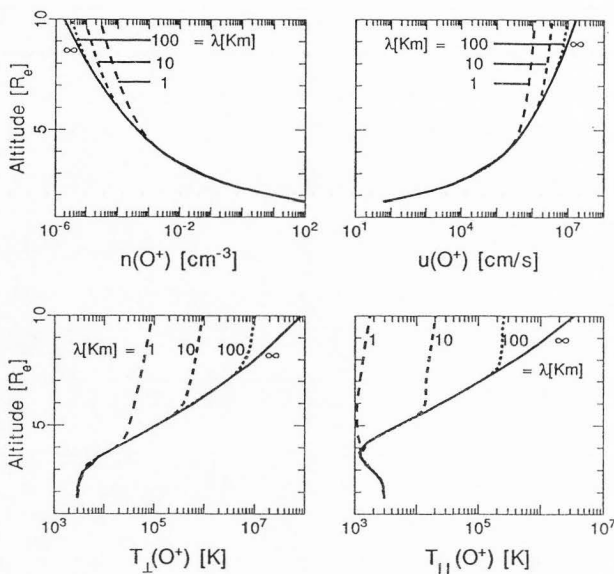


Fig. IV. 7. Altitude profiles of the lower order O^+ moment for different electromagnetic turbulence wavelengths (λ). The wavelengths considered here are $\lambda = 100$ km (dotted), $\lambda = 10$ km (dashed), $\lambda = 1$ km (long dashed), and $\lambda \rightarrow \infty$ (solid). The O^+ moments considered here are: density $n(O^+)$ (top left), drift velocity $u(O^+)$ (top right), perpendicular temperature $T_{\perp}(O^+)$ (bottom left), and parallel temperature $T_{\parallel}(O^+)$ (bottom right).

To study the effect of finite Larmor radius on H^+ ions, we calculated $f(H^+)$ at different altitudes and for different values of λ_{\perp} . The results are shown in Figure IV.8. For $\lambda_{\perp} = 100$ km, $f(H^+)$ is identical to the case of infinite wavelength (i.e., right panel of Figure IV.2). The same is true for the case of ($\lambda_{\perp} = 10$ km) up to $10 R_e$. Had we extended our modeling region, the toroidal features would have appeared at $12 R_e$ (not shown here). However, at such high altitudes the adopted model of \mathbf{B} is not valid, and consequently our results are valid only in a qualitative sense. For short wavelength ($\lambda_{\perp} = 1$ km) and high altitude ($10 R_e$) the toroidal features of $f(H^+)$ are well pronounced.

The difference between the behavior of O^+ and H^+ under the influence of finite a_L is due to two reasons. First, the large mass ratio ($m_{O^+} = 16m_{H^+}$) and secondly, the preferential heating of O^+ noted earlier. Therefore, the Larmor radius a_L for O^+ is higher than that for H^+ . The self-limiting effect of ion heating is significant for $a_L/\lambda_{\perp} > 1$. Consequently, the saturation point occurs at higher altitudes for H^+ than for O^+ .

Figure IV.9 shows the profiles of the lower order moment for H^+ ions. Since the saturation point in the case of H^+ occurs at higher altitudes, we extended the simulation tube to $14 R_e$. The behavior of H^+ ions below the saturation point (i.e., $a_L/\lambda_{\perp} < 1$) is the same for all values of λ_{\perp} (i.e., ion self limiting is negligible). Above the saturation point the H^+ moments display trends similar to those of O^+ moments as λ_{\perp} decreases. For example, the drift velocity $u(H^+)$ (top right) decreases due to the reduction in the heating rate and the density $n(O^+)$ (top left) increases to keep the net escape flux constant. Because of the significant reduction in the heating rate above the saturation point, the perpendicular temperature $T_{\perp}(H^+)$ (bottom left) and consequently the parallel temperature $T_{\parallel}(H^+)$ (bottom right) decrease as λ_{\perp} decrease. In general, the saturation point occurs at higher altitudes for larger values of λ_{\perp} , namely, at about $8 R_e$, $10 R_e$, and $> 14 R_e$ for the cases of ($\lambda_{\perp} = 1$ km, 10 km, and ≥ 100 km), respectively.

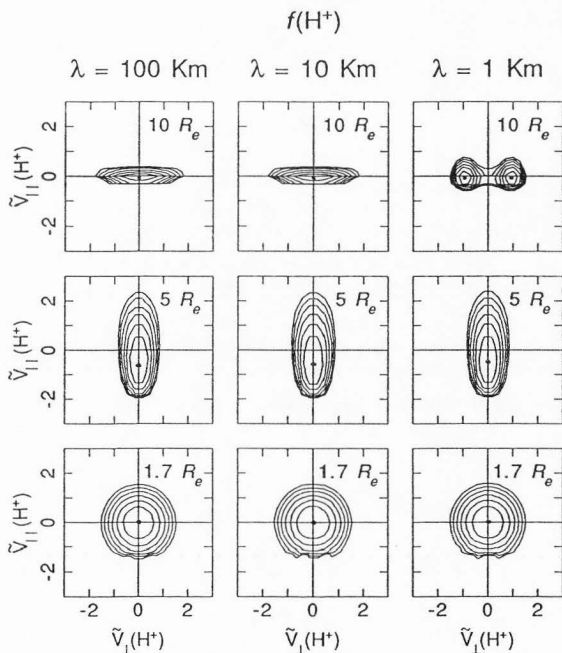


Fig. IV. 8. H^+ velocity distribution function at different geocentric distances for different EMIC-wavelengths λ_{\perp} . The format is similar to that of Figure IV.6.

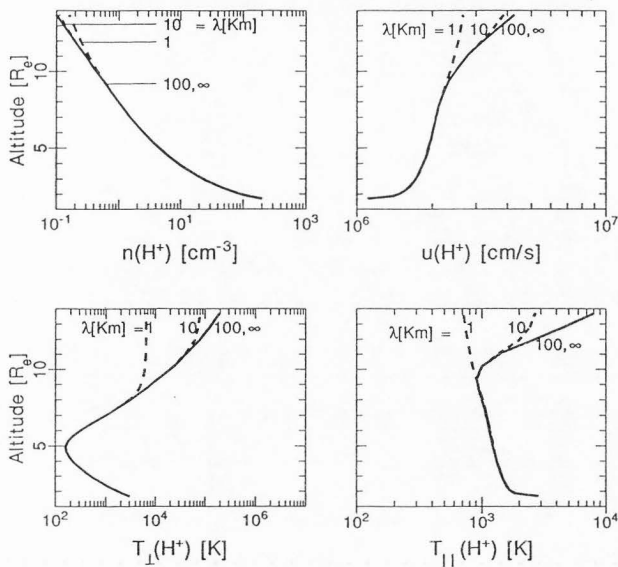


Fig. IV. 9. Altitude profiles of the lower order H^+ moments. The format is similar to that of Figure IV.7.

7 Effect of WPI Level

The observed spectral density shows a great variability (up to three orders of magnitudes) over a time interval as short as a few minutes as shown in the top panel of Figure IV.1, for example. In the previous sections we adopted an average profile \bar{S} . In order to study the effect of the adopted level of WPI on the results, we repeated the simulations with two extreme values of S . In particular, we considered the cases of ($S = 30\bar{S}$), which corresponds to a high level of WPI, and of ($S = \bar{S}/30$), which corresponds to a low level of WPI. The obtained results should bracket all physically plausible ones.

The profiles of O^+ ions moments ($n(O^+)$, $u(O^+)$, $T_{\perp}(O^+)$, and $T_{\parallel}(O^+)$) for different levels of WPI are presented in Figure IV.10. The profiles corresponding to the average level \bar{S} are given by solid lines and denoted by the letter A, while the high and low levels are given by dotted and dashed lines and denoted by the letters H and L, respectively. The case of negligible WPI (long dashed) is included for comparison and denoted by "NO". Expectedly, as WPI increases, the ion heating in the perpendicular direction increases, and the moments' profile is modified correspondingly. For example, the drift velocity $u(O^+)$ (top right) increases with the level of WPI. This is a result of the increased ion perpendicular heating, and the corresponding enhancement of the upward mirror force. An enhancement of about an order of magnitude was found to occur at $10 R_e$ for the cases of low and high levels of WPI.

As we discussed earlier, the WPI causes two opposing effects on $n(O^+)$, namely, an increasing effect due to the increased number of particles that are able to overcome the potential barrier, and a decreasing one to compensate for the increase in $u(O^+)$. The intricate balance between these two effects results in the somewhat complicated behavior of $n(O^+)$ profiles as given in the top left panel.

For negligible WPI, $T_{\perp}(O^+)$ decreases monotonically because of the perpendicular adiabatic cooling. For a low level of WPI, $T_{\perp}(O^+)$ slightly decreases at low altitudes due

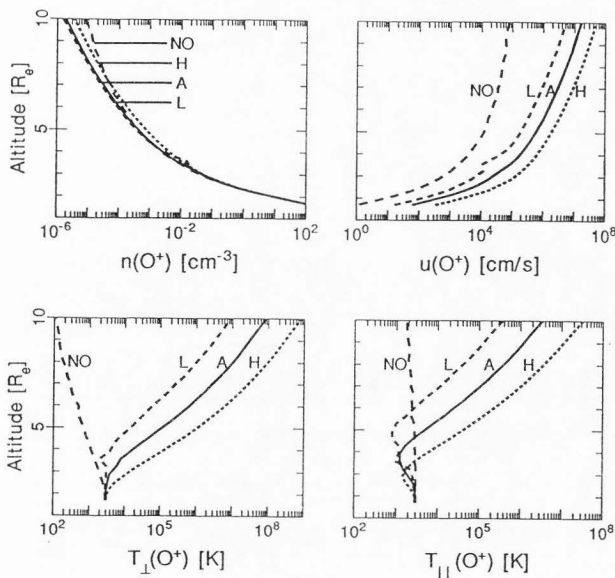


Fig. IV. 10. Altitude profiles of the lower order O^+ moments for different spectral densities. The cases considered here are high level of WPI marked by "H" (dotted), low level of WPI marked by "L" (dashed), average level of WPI marked by "A" (solid), and negligible WPI marked by "NO" (long dashed). The O^+ moments considered here are the same as in Figure IV.7.

to the dominance of perpendicular adiabatic cooling, and then starts to increase due to the perpendicular heating. For average and high levels of WPI, $T_{\perp}(O^+)$ increases monotonically, because of the perpendicular heating which is enhanced at low altitudes due to the "pressure cooker" effect. The O^+ parallel temperature $T_{\parallel}(O^+)$ is presented in the bottom right panel. In the absence of WPI, $T_{\parallel}(O^+)$ decreases monotonically, due to parallel adiabatic cooling. For a low level of WPI, the mirror force is increased and hence the parallel adiabatic cooling is enhanced at low altitudes. At higher altitudes, the ion heating dominates, creating a minimum of $T_{\parallel}(O^+)$ at about $5 R_e$. As the WPI level increases, both parallel adiabatic cooling and energy transfer from the perpendicular to parallel directions are enhanced. This results in further reduction of $T_{\parallel}(O^+)$ at low altitudes as well as further increase of $T_{\parallel}(O^+)$ at high altitudes. Besides, the minimum of $T_{\parallel}(O^+)$ occurs at lower altitudes.

Figure IV.11 shows the profiles of H^+ moments, namely, $n(H^+)$, $u(H^+)$, $T_{\parallel}(H^+)$, and $T_{\perp}(H^+)$ for different levels of WPI. In general, as the level of WPI increases (from negligible, to low, to average, to high), the basic physical mechanisms that arise are the same discussed for O^+ ions, that is, parallel adiabatic cooling, perpendicular adiabatic cooling, perpendicular heating, perpendicular-to-parallel energy transfer, etc. This explains the somewhat similar response of the two species. However, distinct differences between the behavior of the two species remain because of the different shapes of their potential energies $\phi(H^+)$ and $\phi(O^+)$. In particular $\phi(H^+)$ is negative and monotonically decreasing with altitude while $\phi(O^+)$ has a positive maximum as explained in Barakat and Schunk (1983).

Since $\phi(H^+)$ is a monotonically decreasing negative function of altitude, the only influence of WPI on $u(H^+)$ is to accelerate the ions at high altitude. As the level of WPI increases, $u(O^+)$ is enhanced (top right) by a factor as high as 8 for a high level of WPI at altitudes of $10 R_e$. Since H^+ is in a flux-saturated flow condition, $n(H^+)$ systematically

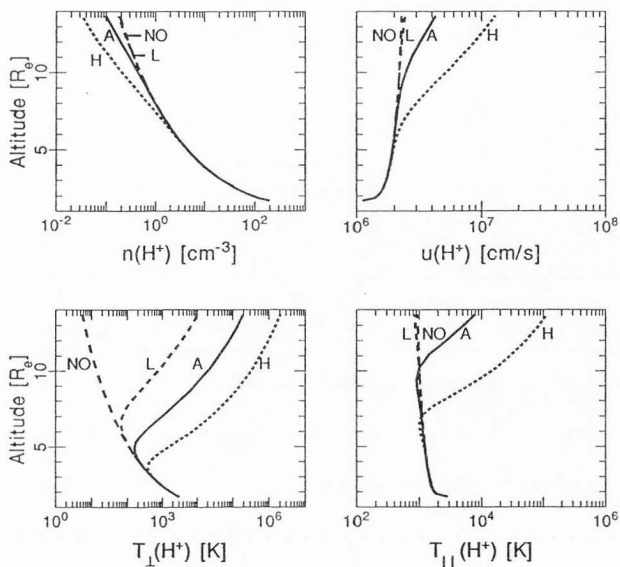


Fig. IV. 11. Altitude profiles of the lower order H^+ moments for different levels of WPI. The moments considered here are the same as in Figure IV.7. The format is similar to that of Figure IV.10.

decreases (top left) with the level of WPI to compensate for the increase in $u(H^+)$. In contrast to the O^+ , the H^+ perpendicular temperature (bottom left) decreases at low altitudes for all levels of WPI considered. This is due to the absence of the "pressure cooker" effect which existed for the O^+ ions. The bottom right panel shows that for the case of low level WPI, the enhanced parallel adiabatic cooling reduces $T_{\parallel}(H^+)$ at all altitudes considered as compared to the case of no WPI. At higher levels of WPI the parallel adiabatic cooling is enhanced more, but eventually overcome by energization at high altitudes. This creates a shallow minimum at about $10 R_e$ for the case of ($S = \bar{S}$). As the WPI increases to its high level ($S = 30 \bar{S}$), the minimum occurs at lower altitudes of about $6 R_e$.

8 Summary

We investigated the effects of WPI on the H^+ and O^+ ions outflow in the polar wind using a Monte Carlo simulation. The data of the PWI aboard DE-1 were used in order to obtain altitude-dependent ion perpendicular diffusion coefficients in the velocity space D_{\perp} . In addition to the WPI, we considered the body forces (gravitational and polarization electrostatic) and the divergence of geomagnetic field lines. It was concluded that:

1. As a result of perpendicular heating, the temperature anisotropy (T_{\perp}/T_{\parallel}) was reduced at lower altitudes, and even reversed ($T_{\perp} > T_{\parallel}$) at higher altitudes.
2. The O^+ velocity distribution $f(O^+)$ developed conic features at high altitudes due to WPI.
3. The points above which significant influence of WPI occurred for O^+ ions were found to occur at altitudes lower than those of H^+ ions.
4. Comparing the results of H^+ and O^+ , we found that O^+ ions were preferentially heated.
5. The escape flux of O^+ increased by a factor of 40 due to WPI, while the escape flux of H^+ remained constant.

As the ions were heated at high altitudes, their gyro-radius a_L increases and may exceed the wavelength in the perpendicular direction λ_{\perp} . This resulted in a velocity-dependent velocity diffusion coefficient D_{\perp} . The effect of this phenomenon was investigated by considering a wide range of λ_{\perp} between 1 and 100 km. In general, we found that:

1. At low altitudes, the ratio a_L/λ_{\perp} was much less than unity and, consequently, the results were independent of λ_{\perp} .

2. Above a certain point (called the saturation point) the ratio a_L/λ_{\perp} became comparable to or exceeded unity and the ion heating became self limiting.

3. Above the saturation point, the ion distribution function displayed a toroidal feature, because the ions tend to diffuse out of the heating zone in the velocity space.

4. The ion heating rate is dramatically reduced above the saturation point.

5. As λ_{\perp} decreased, the ratio a_L/λ_{\perp} became comparable to unity and, hence, the saturation point occurred at lower altitudes.

6. The saturation point of O^+ occurred at lower altitudes than those for H^+ . This is due to both the larger mass and larger energy of O^+ as compared to those of H^+ .

Finally, we considered a range of wave spectrum S as wide as three orders of magnitudes in order to take into consideration the large variability of the observed spectrum. We noticed that the main (qualitative) features of the moment's profiles remained unchanged, in spite of the large (quantitative) variability they displayed.

References

- Barakat, A. R., and I. A. Barghouthi**, The effect of wave-particle interaction on the polar wind: Preliminary results, *Planet. and Space sci.*, submitted, 1994.
- Barakat, A. R., H. G. Demars, and R. W. Schunk**, Application of the generalized transport equations on the wave-particle interactions at high latitudes, in

Physics of Space Plasmas, edited by T. Chang, G. B. Crew, and J. R. Jasper, submitted, 1993.

Barakat, A. R., and R. W. Schunk, O⁺ ions in the polar wind, *J. Geophys. Res.*, 7887-7894, 1983.

Barakat, A. R., and R. W. Schunk, Effect of hot electrons on the polar wind, *J. Geophys. Res.*, **89**, 9771-9783, 1984.

Barakat, A. R., and R. W. Schunk, Stability of the polar wind, *J. Geophys. Res.*, **92**, 3409-3415, 1987.

Barakat, A. R., and R. W. Schunk, Stability of the H⁺ beams in the polar wind, *J. Geophys. Res.*, **94**, 1487-1494, 1989.

Barakat, A. R., R. W. Schunk, T. E. Moore, and J. H. Waite, Ion escape fluxes from the terrestrial high-latitude ionosphere, *J. Geophys. Res.*, **92**, 12,255-12,266, 1987.

Biddle, A. P., T. E. Moore, and C. R. Chappell, Evidence for ion heat flux in the light ion polar wind, *J. Geophys. Res.*, **90**, 8552-8558, 1985.

Chang, T., G. B. Crew, N. Hershkowitz, J. R. Jasperse, J. M. Retterer, and J. D. Winningham, Transverse acceleration of oxygen ions by electromagnetic ion cyclotron resonance with broadband left-hand-polarized waves, *Geophys. Res. Lett.*, **13**, 636, 1986.

Chappel, C. R., T. E. Moore, and J. H. Waite, Jr., The ionosphere as a fully adequate source of plasma for the earth's magnetosphere, *J. Geophys. Res.*, **92**, 5896-5910, 1987.

Chen, M. W., and M. Ashour-Abdalla, Heating of the polar wind due to ion beam instabilities, *J. Geophys. Res.*, **95**, 18,949-18,968, 1990.

Curtis, S. A., Equatorial trapped plasmasphere ion distributions and transverse stochastic accelerations, *J. Geophys. Res.*, **90**, 1765, 1985.

- Ganguli, S. B., and P. J. Palmadesso**, Plasma transport in the auroral return current region, *J. Geophys. Res.*, **92**, 8673-8690, 1987.
- Ganguli, S. B., P. J. Palmadesso, and H. G. Mitchell**, Effects of electron heating on the current driven electrostatic ion cyclotron instability and plasma transport processes along auroral field lines, *Geophys. Res. Lett.*, **15**, 1291-1294, 1988.
- Gurnett, D. A., R. L. Huff, J. D. Menietti, J. L. Burch, J. D. Winningham, and S. D. Shawhan**, Correlated low-frequency electric and magnetic noise along the auroral field lines, *J. Geophys. Res.*, **89**, 8971-8985, 1984.
- Gurnett, D. A., and U. S. Inan**, Plasma wave observations with the Dynamics Explorer 1 spacecraft, *Rev. Geophys.*, **26**, 285-316, 1988.
- Horwitz, J. L.**, Residence time heating effect in auroral conic generation, *Planet. Space Sci.*, **32**, 1115-1117, 1984.
- Li, P., G. R. Wilson, J. L. Horwitz, and T. E. Moore**, Effect of mid-altitude ion heating on ion outflow at polar latitudes, *J. Geophys. Res.*, **93**, 9753-9763, 1988.
- Moore, T. E., C. R. Chappell, M. Lockwood, and J. H. Waite, Jr.**, Superthermal ion signatures of auroral acceleration processes, *J. Geophys. Res.*, **90**, 1611-1618, 1985.
- Persoon, A. M., D. A. Gurnett, and S. D. Shawhan**, Polar cap electron densities from DE 1 plasma wave observations, *J. Geophys. Res.*, **88**, 10,123-10,136, 1983.
- Retterer, J. M., T. Chang, G. B. Crew, J. R. Jasperse, and J. D. Winningham**, Monte Carlo modeling of oxygen ion conic acceleration by cyclotron resonance, *Phys. Rev. Lett.*, **59**, 148, 1987.

Schunk, R. W., Polar wind tutorial, in *Physics of Space Plasma (1988)*, SPI Conf.

Proc. and Reprint Series, No. 8, edited by T. S. Chang, G. B. Crew, and J. R. Jasperse, Scientific Publishers, Inc., Cambridge, MA, 1989.

Schunk, R. W. and J. J. Sojka, A three-dimensional time-dependent model of the polar wind, *J. Geophys. Res.*, **94**, 8973-8991, 1989.

CHAPTER V

THE EFFECTS OF WAVE-PARTICLE INTERACTION ON H^+ AND O^+
OUTFLOW AT HIGH LATITUDE: A COMPARATIVE STUDY

ABSTRACT

A Monte Carlo simulation was used to study the effect of wave-particle interaction (WPI) on ion outflow at high latitudes (the auroral region and the polar cap). As the ions drift upward along the geomagnetic field lines, they interact with the electromagnetic turbulence and consequently get heated in the direction perpendicular to the geomagnetic field. The mirror force converts some of the gained ion energy in the perpendicular direction into parallel kinetic energy. These effects combine to form an ion-conic distribution. Previous studies of WPI in the auroral region neglected the body forces (i.e., gravitational and polarization electrostatic) and the altitude-dependence of the spectral density. In contrast, this work included the effect of body forces, and an altitude-dependent spectral density. The ion distribution function, the profiles of ion density, drift velocity, and parallel and perpendicular temperatures were presented for both H^+ and O^+ ions. These results were compared to the ones corresponding to polar wind conditions. The main conclusions are as follows: (1) The effect of body forces is more important in the polar wind case and for the O^+ ions than it is for the auroral region and the H^+ ions, respectively; (2) the O^+ ions are preferentially energized in both regions; (3) both ions (H^+ and O^+) are more energetic in the auroral region at most altitudes; and (4) the results of the Monte Carlo simulations agree with the "analytical" results of the mean particle theory.

1 Introduction

The coupling between the ionosphere and the magnetosphere is a subject of intense investigation. A prominent mechanism of this coupling is the flow of plasma along the "open" geomagnetic field lines at high latitude. The connection provided by these field lines facilitates the exchange of mass and energy between the ionosphere and the magnetosphere. Chappell *et al.* (1987) showed that the outflow of ions from the high latitude ionosphere is fully adequate to provide the magnetospheric plasma. In general, there are three main ionospheric sources for magnetospheric plasma, namely, the polar cap, the auroral region, and the cusp.

The large area of the polar cap makes it a significant source of ions via the relatively low energy ion outflow known as the polar wind. Several models were developed to study the polar wind, including generalized transport, semi-kinetic, fully kinetic, and Monte Carlo models. As a result of these studies a "classical" picture of the polar wind emerged. The ions were found to become supersonic at high altitudes and develop temperature anisotropy ($T_{\parallel} > T_{\perp}$) and an upward heat flow vector (e.g., Barakat and Schunk, 1983). Several studies were devoted to include the nonclassical features of the polar wind. The escape flux of O^+ was found to be greatly enhanced due to elevated electron temperature, elevated ion temperature, and energetic magnetospheric electrons (Barakat and Schunk, 1983, 1984; Li *et al.*, 1988).

Theoretical studies (Barakat and Schunk 1987, 1989; Chen and Ashour-Abdalla, 1990) indicated that the polar wind could become unstable. Significant levels of electromagnetic turbulence were observed, for example by the Plasma Wave Instrument (PWI) aboard the DE-1 satellite (Gurnett and Inan, 1988). The ion heating due to ion cyclotron resonances with these turbulence has an important effect on the escape of heavy ionospheric ions into the magnetosphere.

Barakat and Barghouthi (1994a, b) used a Monte Carlo approach to study the effect of wave-particle interactions (WPI) on the H^+ and O^+ outflow in the polar wind. However, these studies were parametric, that is, an altitude-independent diffusion coefficient in the velocity space (D_{\perp}) was adopted, and was varied over a wide range of values. They found that appreciable effects of WPI occurred for values of $\tilde{D}_{\perp} [= D_{\perp} / (v_{th}^3 / r_0)]$ comparable to or greater than unity, where r_0 is the exobase geocentric distance and v_{th} is the ion's thermal speed. Conics were found to form for the ion velocity distributions due to the combined effect of perpendicular heating and "folding" of the distribution function as the ions drift along the diverging geomagnetic field lines. An interesting peak in the O^+ temperature at low altitudes formed due to the "pressure cooker" effect.

A realistic altitude-dependent WPI was included by Barghouthi *et al.* (1994). They used the data collected by the PWI to find a power law for $D_{\perp} [\sim (r/r_0)^{3\alpha}]$ for both profiles of D_{\perp} for O^+ and H^+ . This made it possible to find a consistent solution for the two ions' densities. They found that the O^+ is preferentially heated due to its higher mass and due to the pressure cooker effect. The escape flux of O^+ was greatly enhanced while that of the H^+ remained unchanged. Finally, at high altitudes the ion gyro-radius a_L could become comparable to the wavelength of the electromagnetic turbulence λ_{\perp} perpendicular to \mathbf{B} and D_{\perp} was found to decrease rapidly for large values a_L/λ_{\perp} . This mechanism resulted in a self-limiting heating, and the velocity distribution function displayed toroidal features.

In the auroral region, the observed levels of turbulence exceed those in the polar cap by several orders of magnitude. Therefore, it was natural for the studies of the effect of WPI on auroral field lines to precede those of the polar wind. In a series of papers, a Monte Carlo simulation was used to investigate the effect of WPI on the ion outflow along auroral field lines (e.g., Retterer *et al.*, 1987a, b). The model adopted ignored the effect

of body forces (gravitational, and polarization electrostatic) and assumed an altitude independent wave spectral density S . The O^+ ions were shown to form conics in agreement with observations.

Several other techniques were developed to address similar problems. Ganguli and Palmadesso (1987) and Ganguli *et al.* (1988) used a phenomenological approach to include the effect of WPI on auroral plasma transport in a self-consistent manner. Also, Barakat *et al.* (1994) solved the 16-moment transport equations for the same problem addressed by Retterer *et al.* (1987a) using a Monte Carlo simulation. The 16-moment method was shown to be comparable in accuracy with the Monte Carlo one, and required far fewer computer resources.

In this work, we compare the behavior of plasma outflow in the polar wind to its behavior on auroral field lines. We modified the model of WPI used by Retterer *et al.* (1987a) by including the effects of body forces and adopting an altitude-dependent wave spectral density S , consistent with observation. The effects of body forces on the results of the polar wind and on the auroral region are also investigated.

This chapter is organized as follows: A short description of the model in the auroral region is provided in Section 2, with a detailed description of the model given by Barghouthi *et al.* (1994). The model is tested in Section 3. We compared the results of the model for the auroral region conditions similar to those adopted by Retterer *et al.* (1987a) with the Monte Carlo results of Retterer *et al.* (1987a), and with the estimates of the mean particle theory (Chang *et al.*, 1986) at $2.0 R_e$. The effects of the altitude dependent WPI and the geomagnetic field on the plasma outflow along the auroral field lines are discussed in Section 4. In Section 5 we compared the results of the Monte Carlo simulations for auroral region conditions and the altitude dependent WPI with the estimates of the mean particle theory. The effects of body forces in the auroral region and in the polar wind are discussed in Section 6. A comparison between the effects of WPI in the auroral region

and in the polar wind is presented in Section 7. Our conclusions are presented in Section 8.

2 The Model

In this work we studied the steady-state flow of a fully ionized plasma (H^+ , O^+ , and electrons) along the geomagnetic field lines in the high latitude topside ionosphere (i.e., the auroral region and the polar cap). The polar wind model was explained in detail by Barghouthi *et al.* (1994). For the auroral region conditions we adopted a model similar to the polar wind model. Only a brief description of that model is given here. The simulation region was a geomagnetic tube extending from the exobase at $1.2 R_e$ to $10 R_e$. The geomagnetic field B was taken to be proportional to r^{-3} where r is the geocentric distance. In this study we considered the effects of body forces (i.e., gravitational and polarization electrostatic) which have not been included in the pioneering work of Retterer *et al.* (1987a) and Chang *et al.* (1986). The potential energy due to the body forces is given by:

$$\phi(r) = kT_e \ln\left(\frac{n_e}{n_{e0}}\right) + GM_e m \left(\frac{1}{r_0} - \frac{1}{r}\right) \quad (1)$$

where k is Boltzmann's constant, T_e is the electron temperature, n_e and n_{e0} are the electron densities at r and r_0 (i.e., the exobase), respectively, which can be calculated from the quasi-neutrality condition [$n_e \equiv n(O^+) + n(H^+)$]. G is the universal gravitational constant, M_e is the mass of the earth, and m is the ion's mass (i.e., H^+ or O^+).

The wave-particle interaction between the ions and the electromagnetic turbulence can be described by the diffusion equation

$$\frac{\partial f}{\partial t} = \frac{1}{v_\perp} \frac{\partial}{\partial v_\perp} \left[D_\perp v_\perp \frac{\partial f}{\partial v_\perp} \right] \quad (2)$$

where D_\perp is the quasi-linear velocity diffusion rate perpendicular to the geomagnetic field and is given by Retterer *et al.* (1987b)

$$D_{\perp} = \frac{\eta q^2}{4m^2} |E_x(\omega = \Omega)|^2 \quad (3)$$

where q and m are the ion's charge and mass respectively, Ω is the ion's gyro-frequency, and ω is the wave frequency. $|E_x|^2$ is the measured spectral density of the electromagnetic turbulence, and η is the proportion of the measured spectral density that corresponds to a left hand polarized wave.

A Monte Carlo simulation was developed in order to study the effects of WPI, body forces, and diverging geomagnetic field lines on ion outflow in the auroral region. The ions were injected at the exobase r_0 with velocity consistent with the ion distribution function. The ion motion was followed for a 'small' time interval Δt as it moved under the influence of body forces and a diverging geomagnetic field. The influence of WPI during Δt was simulated by incrementing the ion's perpendicular velocity by a random increment Δv_{\perp} such that :

$$\langle (\Delta v_{\perp})^2 \rangle = 4D_{\perp} \Delta t \quad (4)$$

A large number of test ions (10^5 - 10^6) were followed (one at a time) as they moved until they exited the simulation region. The ion distribution functions, as well as the altitude profiles of its moments (density, drift velocity, parallel temperature, and perpendicular temperature), were computed.

It is worthwhile to point out that an iterative approach was used to find the electrostatic potential in a consistent manner. We started the simulation with body forces turned off. The resulting H^+ and O^+ densities were used to find $\phi(r)$. The iteration process was continued until convergence was reached.

As mentioned earlier, the models used by Retterer *et al.* (1987a) and Chang *et al.* (1986) adopted an altitude-independent spectral density of the electromagnetic turbulence.

However, Barghouthi *et al.* (1994) found the observed spectral density of the electromagnetic turbulence to be altitude-dependent in the polar cap region. Moreover, it is well accepted that the electromagnetic turbulence is more intense in the auroral region than in the polar cap. Therefore, the value of D_{\perp} should be higher in the auroral region than in the polar cap. In Figure V.1, we compared the values of the velocity diffusion coefficient D_{\perp} in the polar cap (dashed) (Barghouthi *et al.*, 1994) with those in the auroral region (dotted) (Retterer *et al.*, 1987a) and found that $D_{\perp}(O^+)$ in the polar cap is higher than in the auroral region at higher altitudes. This result contradicts the above principle. This motivated our research to correct the altitude dependence of D_{\perp} for both H^+ and O^+ , and to study the effects of the altitude-dependence WPI on plasma outflow in the auroral region. In this study, we assumed the altitude-dependence of the spectral density in the auroral region to be similar to that in the polar wind (i.e., polar cap). We calculated the spectral density in the auroral region by using the altitude dependence from Barghouthi *et al.* (1994) and the measured spectral density at $2.0 R_e$ from Retterer *et al.* (1987a). Accordingly, the perpendicular diffusion coefficients $D_{\perp}(O^+)$ and $D_{\perp}(H^+)$ are calculated and the results are :

$$D_{\perp}(O^+)[\text{cm}^2 / \text{sec}^3] = 6.94 \times 10^5 (r^{13.3}) \quad (5)$$

$$D_{\perp}(H^+)[\text{cm}^2 / \text{sec}^3] = 4.45 \times 10^7 (r^{7.95}) \quad (6)$$

The boundary conditions selected for the auroral altitude-dependence WPI are similar to those of Retterer *et al.* (1987a) and Ganguli and Palmadesso (1987). At the lower boundary ($1.2 R_e$) we set the H^+ ion drift velocity at 16 km/sec, the H^+ ion density at 100 cm^{-3} , and the H^+ ion temperature at the lower boundary at 0.2 eV. At the lower boundary we set the O^+ ion drift velocity at 0 km/sec, the oxygen ion density at 5000

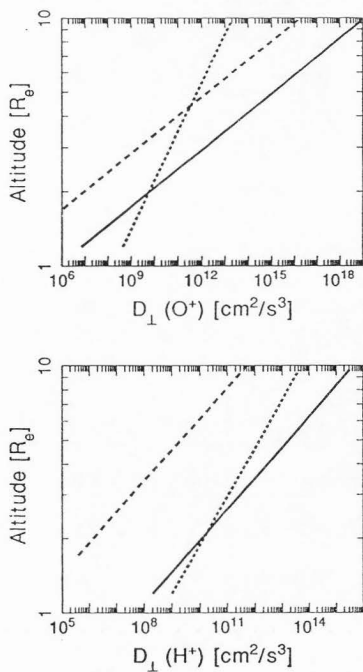


Fig. V. 1. Profiles of the perpendicular diffusion coefficients $D_{\perp}(O^+)$ (top-panel) and (bottom-panel) for different studies. The uncorrected profiles (dotted) for the auroral region are similar to those adopted by Retterer *et al.* (1987a). The solid line represents the D_{\perp} profiles corrected as explained in the text. The D_{\perp} profile for the polar wind is represented by the dashed line.

cm^{-3} , and the O^+ ion temperature at 0.2 eV. The electron temperature was kept constant at 1000 K along the entire length of the flux tube. At the lower boundary, we assume a flux of ions (H^+ or O^+) moving into the simulation region. We also assume the velocity distribution to be a drifting Maxwellian for H^+ ions and the up-going half of a nondrifting Maxwellian for O^+ ions. The perpendicular diffusion coefficients are given by equations (5) and (6). η was chosen to be 1/16 consistent with the values adopted by Chang *et al.* (1986). The body forces are turned off in Sections 3, 4, and 5, and turned on in Sections 6 and 7.

3 Model Test

As a check on the model, we ran the Monte Carlo simulation for the same initial conditions as used by Retterer *et al.* (1987a). In particular we have chosen O^+ ion outflow in the auroral region, the injection point to be $1.2 R_e$, $T(\text{O}^+) = 0.2 \text{ eV}$, $|E_0|^2 = 1.2 \times 10^{-6} (\text{V/m})^2 \text{ Hz}$ at $\omega_0 / 2\pi = 5.6 \text{ Hz}$, $\alpha = 1.7$, $\eta = 1/8$. Body forces are neglected. The oxygen ion-velocity distribution is calculated at $2.0 R_e$ and several velocity moments are also calculated at $2.0 R_e$, to compare with the results of Retterer *et al.* (1987a) and the mean particle theory calculations of Chang *et al.* (1986).

The O^+ ion velocity distribution at $2.0 R_e$ is presented in Figure V.2. $f(\text{O}^+)$ has conic features which can be explained as follows: As the O^+ ions drift upward along the geomagnetic field lines, they interact with the electromagnetic turbulences and consequently get heated in the direction perpendicular to the geomagnetic field. The mirror force converts some of the ion energy gained in the perpendicular direction into parallel kinetic energy. These two effects combine to form an ion-conic distribution. The O^+ velocity distribution presented in Figure V.2 is similar to the one presented in the top panel of Figure 1 in Retterer *et al.* (1987a).

Additionally, several O^+ velocity moments are calculated and compared with the Monte Carlo results of Retterer *et al.* (1987a) and the estimates of the mean particle theory.

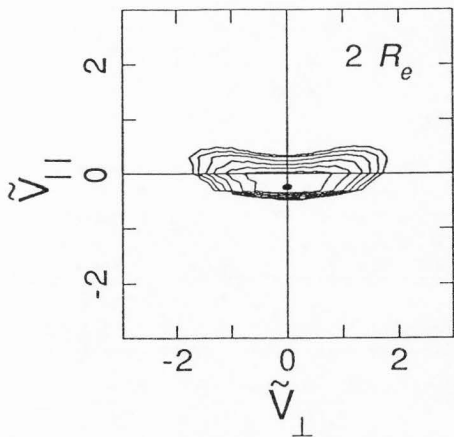


Fig. V. 2. The O^+ velocity distribution function $f(O^+)$ at geocentric distance of $2R_e$ on auroral field lines, using physical conditions identical to those of Retterer *et al.* (1987a). The distribution function $f(O^+)$ is represented by equal-value contours in the normalized random velocity plane $[\tilde{v} = v/[2kT(O^+/m(O^+))]^{1/2}]$. The contours decrease successively by a factor of $e^{1/2}$.

The estimates of the mean particle theory (Chang *et al.*, 1986) are obtained by using the following expressions:

$$W_{i\parallel} = \frac{9m_i}{2^{1/3}} \left[\frac{rD_{\perp}(r)}{(3\alpha+1)(6\alpha+1)} \right]^{2/3} \quad (7)$$

$$W_{i\perp} = \frac{(6\alpha+2)m_i}{2^{1/3}} \left[\frac{rD_{\perp}(r)}{(3\alpha+1)(6\alpha+1)} \right]^{2/3} \quad (8)$$

$$W_i = W_{i\parallel} + W_{i\perp} = (3\alpha+11/2)^{1/3} m_i [rD_{\perp}(r)/(3\alpha+1)]^{2/3} \quad (9)$$

where W_{\parallel} and W_{\perp} are the mean parallel and perpendicular energies, W is the total mean energy, and i denotes the type of the ion (H^+ or O^+). Our Monte Carlo results are calculated by using the following expressions:

$$W_{i\parallel} = \frac{1}{2} m u_i^2 + \frac{1}{2} k T_{i\parallel} \quad (10)$$

$$W_{i\perp} = k T_{i\perp} \quad (11)$$

$$W_i = W_{i\parallel} + W_{i\perp} \quad (12)$$

where u_i , $T_{i\parallel}$ and $T_{i\perp}$ are given by equations (14), (15) and (16), respectively.

Table V. 1 gives the mean parallel energy W_{\parallel} , the perpendicular energy W_{\perp} and the total energy W and also the ratios of the mean W_{\perp} and W_{\parallel} at $2.0 R_e$ for the above three studies. Comparing these studies we found that the Monte Carlo calculations of this study are closer to the estimates of the mean particle theory than are the results of Retterer *et al.* (1987a).

Table V. I. The Monte Carlo results of this study are compared to the Monte Carlo calculation of Retterer *et al.* (1987a) and to the estimates of the mean particle theory.

	Monte Carlo (this study)	Monte Carlo Retterer <i>et al.</i> (1987a)	Mean Particle Theory
W_{\parallel} (eV)	30.16	28.5	30.8
W_{\perp} (eV)	39.69	40.7	40.1
W (eV)	69.84	69.2	70.9
$W_{\perp} / W_{\parallel}$	1.316	1.428	1.302

According to these checks, our model produced the ion-conic distribution in the auroral region and shows excellent agreement with the mean particle theory at $2.0 R_e$.

4 Corrected Auroral Ion Outflow

In this section, we report research into the effects of the altitude-dependent WPI and the divergence of the geomagnetic field lines on O^+ and H^+ ion outflow in the auroral region. The effect of body forces was "turned off" in this work, in order to facilitate the understanding of the different physical mechanisms. These effects are turned on in Sections 6 and 7.

The ion velocity distributions for H^+ and O^+ at different altitudes are presented in Figure V.3. At the injection point $1.2 R_e$ the ion velocity distributions are consistent with the boundary conditions, $f(H^+)$ is drifting Maxwellian, and $f(O^+)$ is half nondrifting Maxwellian. However, as altitude increases, the distribution function develops conic features at $2.5 R_e$ for H^+ and at $1.6 R_e$ for O^+ . The formation of ion-conics is due to WPI which heats the ions in the perpendicular direction and to the mirror force which

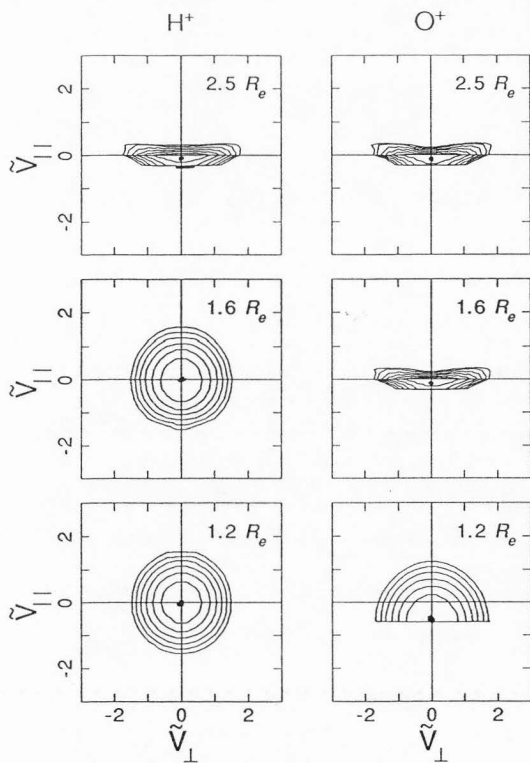


Fig. V. 3. Ion velocity distribution functions at different geocentric distances (1.2, 1.6 and $2.5 R_e$) for H^+ (left panel) and O^+ (right panel). The format is similar to that of Figure V.2.

converts some of the energy gained in the perpendicular direction over to the parallel direction. At higher altitudes the ion velocity distribution's $f(\text{H}^+)$ and $f(\text{O}^+)$ saturate at $2.5 R_e$ and $1.6 R_e$ respectively, due to dominant WPI. This behavior is consistent with the similarity scaling of the velocity distribution discussed by Retterer *et al.* (1987b).

Also, the saturation of the ion velocity distribution is consistent with the mean particle theory (Chang *et al.*, 1986). In that theory, the mean energy ratio W_{\perp}/W_{\parallel} asymptotically approaches a constant value of $(6\alpha + 2)/9$ as shown in Figure V.5 (bottom-panel). More discussions on this theory are found in Section 5.

The lower-order velocity moments of $f(\text{H}^+)$ and $f(\text{O}^+)$ are computed at different altitudes. The moments considered here are defined as follows:

$$n_i = \int f_i d\mathbf{v}_i \quad (13)$$

$$u_i = \frac{1}{n_i} \int v_{i\parallel} f_i d\mathbf{v}_i \quad (14)$$

$$T_{i\parallel} = \frac{m_i}{n_i k} \int (v_{i\parallel} - u_i)^2 f_i d\mathbf{v}_i \quad (15)$$

$$T_{i\perp} = \frac{m_i}{2n_i k} \int v_{i\perp}^2 f_i d\mathbf{v}_i \quad (16)$$

In the above equations i denotes the type of the ion (H^+ or O^+), $n_i, u_i, T_{i\parallel}$, and $T_{i\perp}$ are the ion density, drift velocity, parallel temperature and perpendicular temperature, respectively.

The altitude profiles of O^+ moments (solid lines) and H^+ moments (dotted lines) are given in Figure V.4. The drift velocity (right-top) of the ions (H^+ or O^+) increases with altitude. This can be explained as follows: the WPI heats the ions (H^+ or O^+) in the

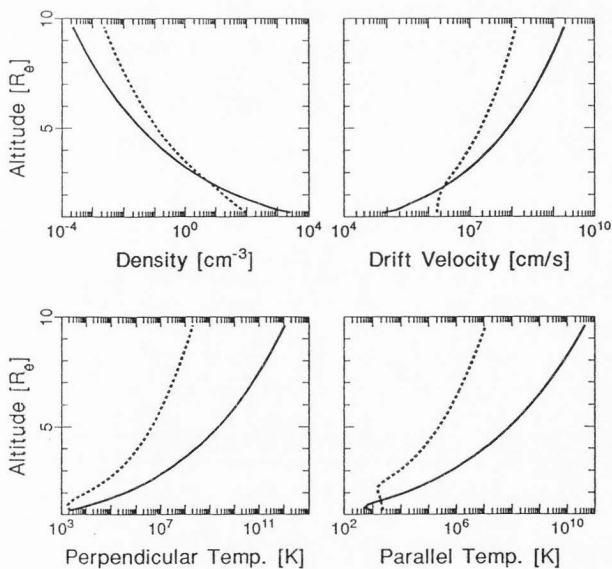


Fig. V. 4. Altitude profiles of the different O^+ (solid) and H^+ (dotted) moments in the auroral region. The moments considered here are density (top-left), drift velocity (top-right), perpendicular temperature (bottom-left), and parallel temperature (bottom-right). No body forces included.

perpendicular direction, which increases the upward mirror force, and, hence, accelerates the ions in the upward direction. Since the H^+ or O^+ ions are in the flux-limiting flow condition, a corresponding decrease in the ion's density (top left panel) is expected in order to compensate for the increase in the ion's drift velocity and, hence, to keep the net escape flux constant. As the strength of WPI increases with altitude, the ion perpendicular temperature (bottom-left) increases. The behavior of the ion perpendicular temperature ($T_{\perp}(O^+)$ or $T_{\perp}(H^+)$) is a result of the balance between the WPI heating in the perpendicular direction and the perpendicular adiabatic cooling. But $T_{\perp}(O^+)$ and $T_{\perp}(H^+)$ are increasing monotonically with altitude, i.e., the heating due to WPI dominates the perpendicular adiabatic cooling. The profiles for ion parallel temperature, $T_{\parallel}(O^+)$ and $T_{\parallel}(H^+)$, are presented in the bottom-right panel of Figure V.4. The effects of WPI on ion parallel temperature are two-fold. First, the increase in the drift velocity of the ion results in parallel adiabatic cooling which decreases ion parallel temperature. Second, the increase of ion perpendicular temperature is eventually transferred into the parallel direction due to the divergence of geomagnetic field lines. The balance between these two effects determines the behavior of $T_{\parallel}(O^+)$ and $T_{\parallel}(H^+)$.

The quantitative differences between the behavior of the O^+ and H^+ ions are due to the large mass ratio ($m_{O^+} = 16m_{H^+}$) and the ion velocity diffusion coefficient, where $D_{\perp}(O^+)$ is larger than $D_{\perp}(H^+)$. Therefore, O^+ is expected to be preferentially heated with respect to H^+ . This result is consistent with the results of Horwitz (1984). For example, $T_{\perp}(O^+)$ is higher than $T_{\perp}(H^+)$ at all altitudes, $u(O^+)$ is higher than $u(H^+)$ at altitudes above $2.0R_e$, and $T_{\parallel}(O^+)$ is higher than $T_{\parallel}(H^+)$ at altitudes above $1.8R_e$. However, at low altitudes the difference between O^+ and H^+ can be attributed to the initial conditions where H^+ was chosen to be supersonic and O^+ trans-sonic.

In this study, the ion Larmor radius a_L was assumed to be much less than the perpendicular wavelength of the electromagnetic turbulence λ_{\perp} . However, as an ion

drifts upward along geomagnetic field lines, it heats up due to WPI, and the geomagnetic field intensity B decreases. The combined effect of these two factors results in a rapid increase in the ion Larmor radius with altitude. At higher altitudes the ion Larmor radius may become comparable to or even greater than the wavelength of the electromagnetic turbulence. Consequently, the velocity independent expression for D_{\perp} given in equation (3) becomes inaccurate. Barghouthi *et al.* (1994) investigated the effect of this phenomenon on the shape of the ion distribution function, and on the altitude profiles of the lower order moment in the polar wind. They found that the ion velocity distribution displayed toroidal features at high altitudes. An ongoing study adopts a more appropriate form for the velocity diffusion coefficient D_{\perp} , in order to investigate the existence of the toroidal distributions in the auroral region which have been observed by Moore *et al.* (1985).

5 Comparison with the Mean Particle Theory

The mean particle theory (Chang *et al.*, 1986) estimates the values of the mean perpendicular and parallel energies as a function of geocentric distance by including the mean heating rate per ion in a set of equations (7), (8), and (9) which describe the motion of an ion guiding center in the geomagnetic field. In order to compare the predictions of this theory to the auroral region simulations, we turned off the body forces, i.e., the Monte Carlo model includes the effect of altitude dependent WPI, the geomagnetic field, and the auroral region conditions mentioned in Section 2. The results of our comparison are presented in Figure V.5. In this figure the left column depicts H^+ ions and the right column, O^+ ions. In each column we calculated the mean parallel energy W_{\parallel} (top), mean perpendicular energy W_{\perp} (middle), and energy ratio W_{\perp}/W_{\parallel} (bottom). Our Monte Carlo results (solid) are calculated by using equations (11), (12), (13), while the estimates of the mean particle theory (dotted) are calculated by using equations (7), (8), and (9). The comparison in the case of O^+ ions (right column) shows an excellent agreement

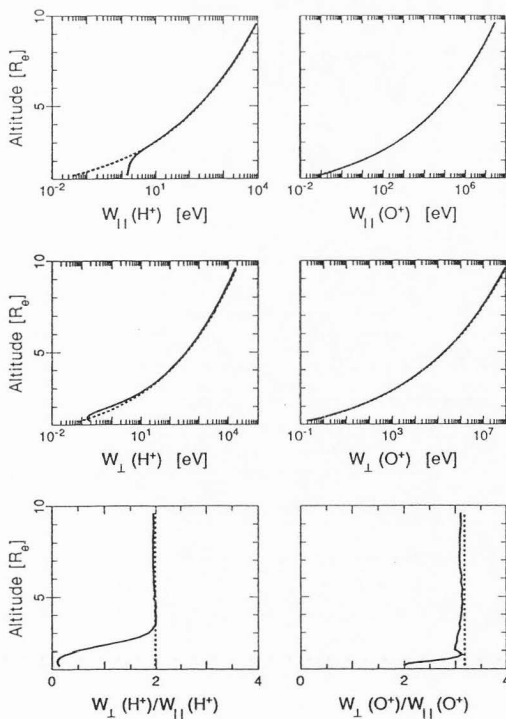


Fig. V. 5. Comparison between the Monte Carlo calculations (solid) and the estimates of the mean particle theory (dotted) for auroral conditions. Both O^+ (right panel) and H^+ (left panel) ions were considered. The mean parallel energy W_{\parallel} (top), the mean perpendicular energy W_{\perp} (middle), and the energy ratio $W_{\perp} / W_{\parallel}$ (bottom) are presented. No body force included.

between the two approaches. For example, the Monte Carlo results (solid) cannot be distinguished from the estimates of the mean particle theory (dotted) in case of W_{\parallel} and W_{\perp} .

The left column compares H^+ ion profiles. The agreement between the Monte Carlo results and the estimates of the mean particle theory is excellent at altitudes above $3R_e$. However, the asymptotic approximation in the mean particle formulas easily accounts for the differences between the results at lower altitudes. For example, as r approaches zero, the results of mean particle theory W_{\parallel} and W_{\perp} approach zero as shown in Figure V.5 (top and middle panels). In another way, the mean particle theory is applicable at altitudes where the achieved energies of the ion are much larger than the initial energies in the distribution, suggesting that the initial state of the distribution has been forgotten (Retterer *et al.*, 1987b).

In the light of this, predictions of the mean particle theory deviated from the Monte Carlo ones at low altitudes, showing higher levels for H^+ than for O^+ . This deviation is likely due to assumed initial conditions for O^+ being closer to the estimates of the mean particle theory at the injection altitude. Therefore, O^+ ions very quickly gained enough energy due to WPI and reached the asymptotic regime. However, the initial conditions for H^+ are far removed from the predictions of the mean particle theory at lower altitudes. Therefore, H^+ ions have to drift to a higher altitude to gain enough energy, through WPI, in order to reach the asymptotic regime.

6 The Effect of Body Forces

One of the objectives of this study is to investigate the effect of body forces (gravitational and electrostatic polarization) on ion outflow at high latitudes. The majority of the previous studies of WPI on auroral field lines neglected this effect (e.g. Retterer *et al.*, 1987a, b; Chang *et al.*, 1986). In contrast, the body forces are included in the Monte Carlo model in addition to the geomagnetic field and the altitude dependence WPI.

Equation (1) gives the potential function ϕ due to the body forces. The potential function $\phi(O^+)$ increases with altitude up to a large maximum value and then decreases, and it is always positive. However, $\phi(H^+)$ is monotonically decreasing. This means that $\phi(O^+)$ acts as a potential barrier to O^+ ion's outflow, while $\phi(H^+)$ acts to enhance the outflow of H^+ ions. In this section we discussed the effects of body forces on O^+ and H^+ ion outflow in the auroral region and in the polar wind.

6.1 Auroral Region

We studied the effects of body forces on H^+ ion outflow in the auroral region; the results are not shown here. We found that the enhancements in the H^+ moments were very minimal. In particular, the H^+ ion acceleration due to body forces is much less than the ion acceleration due to WPI heating, and the temperature enhancement was very negligible.

In the case of O^+ ions, the inclusion of body forces did not enhance the parallel $T_{\parallel}(O^+)$ and perpendicular $T_{\perp}(O^+)$ temperatures and the drift velocity $u(O^+)$. However, it decreased the ion's density $n(O^+)$, Figure V.6, very dramatically, where $n(O^+)$ decreased by a factor of 10^5 at $10R_e$. The response of O^+ density to the inclusion of body forces can be explained as follows. The WPI is weak at lower altitudes and it is dominated by the gravitational force. This gravitational force permits only a few ions (in velocity distribution tail) to reach to high altitudes, where WPI is strong enough. This potential barrier acts as a velocity filter. Therefore, the number of O^+ ions that can overcome the potential barrier and escape is much smaller than for the case of neglected body forces, where all O^+ ions escape.

It was assumed that $f(O^+)$ is the up-going half of a nondrifting Maxwellian at the injection altitude ($1.2 R_e$). The shape of $f(O^+)$ in Figure V.3 (bottom-left panel) is consistent with this assumption in the case of neglected body forces, because all injected O^+ ions drifted upward in the simulation region. The effect of including body forces on

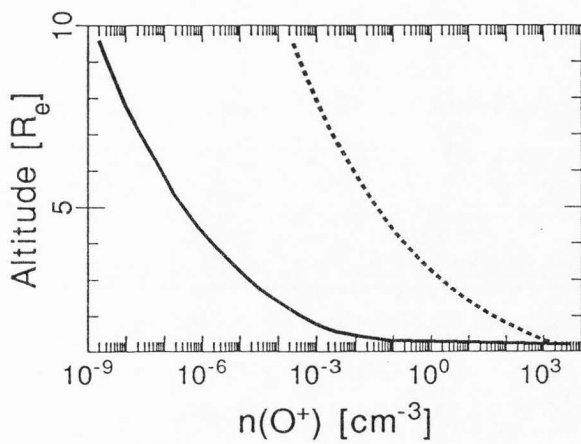


Fig. V. 6. An altitude profile for O⁺ density in the auroral region. The altitude dependent WPI, the divergence geomagnetic field lines, and the body forces were included.

the O^+ velocity distribution $f(O^+)$ is presented in Figure V.7. At the injection point, $f(O^+)$ is Maxwellian, because most of the O^+ ions injected into the simulation region were reflected downward due to the gravitational force. It is worth pointing out that the lower part of $f(O^+)$ at the injection point is larger than the upper part. This is due to the "pressure cooker" effect. Briefly, this effect results from the temporary trapping of the O^+ ions between an upper gravitational and a lower magnetic deflection point. As the ion repeatedly bounces between these deflection points, it is energized to a higher perpendicular temperature. Therefore, O^+ ions reflected downward have a higher temperature than they initially do. At higher altitudes, the WPI takes over and energize the ions to overcome the potential barrier, i.e., it dominates the body forces. For example, $f(O^+)$ in the middle and top panels of Figure V.7 is very similar to the corresponding ones in the right column of Figure V.3, in which the body forces were neglected.

6.2 Polar Wind

Barghouthi *et al.* (1994) studied the effect of WPI on O^+ and H^+ ion outflow in the polar wind. In that study they included the effect of body forces. For the sake of comparison, we turned off the body forces and ran the Monte Carlo model for the polar wind. Figures V.8a and V.8b present the H^+ and O^+ moment profiles for two cases; body forces are included (solid lines) and neglected (dotted lines).

The inclusion of body forces affected the H^+ ion outflow in the following ways:

- (1) The drift velocity $u(H^+)$ (top-right) increases because the body forces accelerate the ions in the upward direction, and these support the heating action of WPI in resulting H^+ ion drifting upward.
- (2) The density $n(H^+)$ (top-left) decreases in order to keep the net escape flux constant.
- (3) The parallel temperature $T_{\parallel}(H^+)$ (bottom-right) decreases due to the enhancement of the parallel adiabatic cooling, which itself is a result of increasing the drift velocity.
- (4) The perpendicular temperature $T_{\perp}(H^+)$ (bottom-left) decreases at high

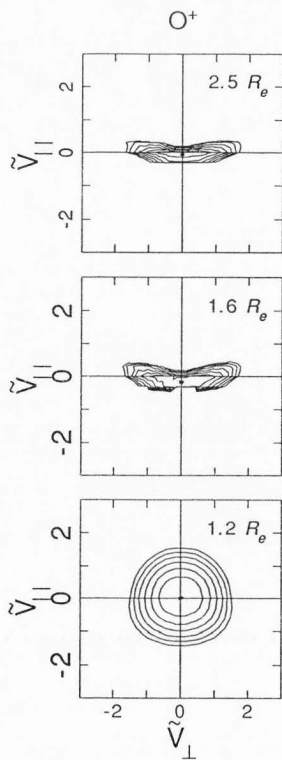


Fig. V. 7. O^+ velocity distribution in the auroral region at different geocentric distances (1.2, 1.6, and $2.5 R_e$). The altitude dependent WPI, the body forces, and the divergence of geomagnetic field lines were included. The format is similar to that of Figure V.2.

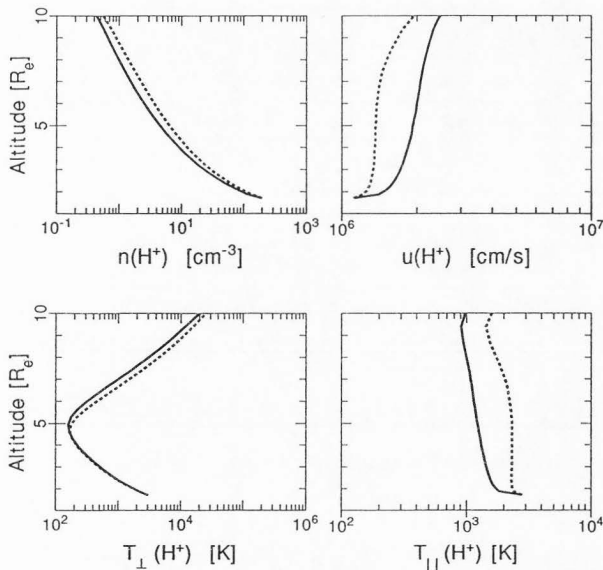


Fig. V. 8a. Comparison of the H⁺ moments in the polar wind for two cases: Body forces included (solid) and body forces neglected (dotted). The moments considered here are H⁺ density (top-left), drift velocity (top-right), perpendicular temperature (bottom-left), and parallel temperature (bottom-right). In both cases the effect of WPI and the geomagnetic field is included.

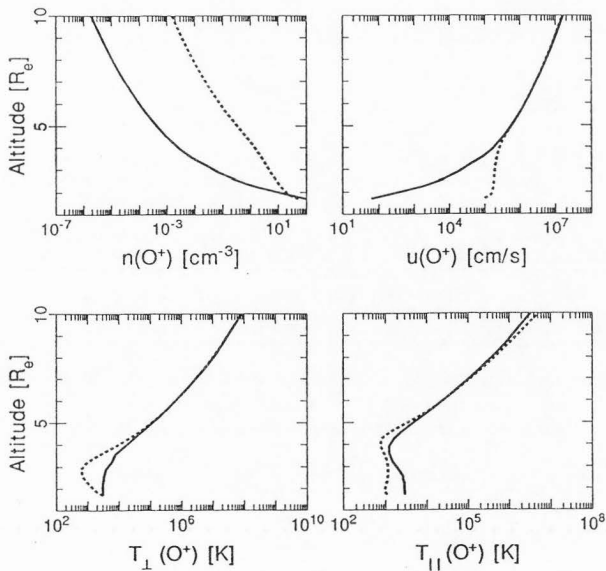


Fig. V. 8b. Comparison of the O⁺ moments in the polar wind for two cases: Body forces included (solid) and body forces neglected (dotted). The format is similar to that of Figure V.8a.

altitudes ($>5R_e$) because the residence time of interaction between H^+ ions and the electromagnetic turbulence decreases due to the enhanced upward acceleration. At lower altitudes ($<5R_e$) $T_{\perp}(H^+)$ did not significantly change because the perpendicular adiabatic cooling dominates the WPI heating.

Figure V.8b shows the effect of body forces on O^+ outflow in the polar wind. As mentioned earlier, $\phi(O^+)$ increases with altitude up to a large maximum value and then decreases. At lower altitudes ($<3R_e$) the drift velocity of O^+ ions $u(O^+)$ (top-right) decreases (solid lines) when the body forces are included, even though the velocity changed from trans-sonic to subsonic. This is due to the potential barrier mentioned earlier; few O^+ ions overcome this barrier and reach high altitudes. Therefore, the majority of O^+ ions are reflected downward. This downward motion decreases the drift velocity $u(O^+)$ because $u(O^+)$ is the average drift velocity of two populations (up going and down going). However, in the case of neglected body forces $u(O^+)$ is the average drift velocity of the up-going population since there is no down-going population. But as O^+ ions become energized enough to overcome the potential barrier at about $3R_e$, the role of the body forces becomes minor and is dominated by WPI heating. The O^+ density $n(O^+)$ (top-left) decreases (solid lines) with altitude when the body forces are included. For example, $n(O^+)$ decreased by a factor of 10^3 at $10R_e$. This is also due to the potential barrier, where the number of O^+ that overcomes the barrier is very small compared to the total number of O^+ ions, which reached to high altitudes where body forces were neglected. The O^+ perpendicular temperature $T_{\perp}(O^+)$ (bottom-left) is monotonically increasing with body forces (solid lines). $T_{\perp}(O^+)$ increases at lower altitudes because of the "pressure cooker" effect discussed earlier, and at higher altitudes due to WPI heating. However, when the body forces are neglected (dotted lines), $T_{\perp}(O^+)$ decreases at lower altitude due to perpendicular adiabatic cooling, and at $3R_e$ it starts to increase due to WPI heating. The WPI heating dominates the body forces at

altitudes above $5 R_E$, and $T_{\perp}(O^+)$ behavior is the same in both cases. The parallel temperature of O^+ ions $T_{\parallel}(O^+)$ (bottom-right) in the case of body forces included is higher than the case of neglected body forces at altitudes below $5 R_E$. This is due to the energy transfer from perpendicular to parallel direction. As O^+ ions overcome the peak of the potential barrier, their drift velocity increases very slightly because $\phi(O^+)$ is decreasing beyond the peak. This increases the parallel adiabatic cooling. Consequently, $T_{\parallel}(O^+)$ slightly decreases at higher altitudes when the body forces are included.

We concluded that had we ignored the body forces in the auroral region, we would have overestimated O^+ density $n(O^+)$, while $u(O^+)$, $T_{\perp}(O^+)$, $T_{\parallel}(O^+)$ and H^+ moments would have not been affected. Also, we do not get the correct shape of $f(O^+)$ at low altitudes. Had we ignored the body forces in the polar wind, we would have overestimated $n(H^+)$, $n(O^+)$ and $T_{\parallel}(H^+)$ at all altitudes, $T_{\perp}(H^+)$ and $T_{\parallel}(O^+)$ at high altitudes, $u(O^+)$ at lower altitudes, underestimated $u(H^+)$ at all altitudes, and $T_{\parallel}(O^+)$ and $T_{\perp}(O^+)$ at lower altitudes. $T_{\perp}(O^+)$ and $u(O^+)$ at high altitudes, and $T_{\perp}(H^+)$ at low altitudes would not have been affected. To sum up, the body forces are more important in the polar cap than in the auroral region, and they are more important for O^+ than for H^+ .

7 Comparison Between WPI in the Auroral Region and the Polar Wind

In this section we compare between the effect of WPI in the polar cap and in the auroral region. The polar wind results were taken from Barghouthi *et al.* (1994). The auroral region results are obtained by running the Monte Carlo simulation for initial conditions similar to those given in Retterer *et al.* (1987a) and Ganguli and Palmadesso (1987) with body forces and the altitude dependence of the wave spectrum included. The results of this comparison are given in Figure V.9.

The left panel of Figure V.9 represents the results of comparing H^+ ions. The H^+ drift velocity $u(H^+)$ (top-left) slowly increases in the polar wind (dotted) while it

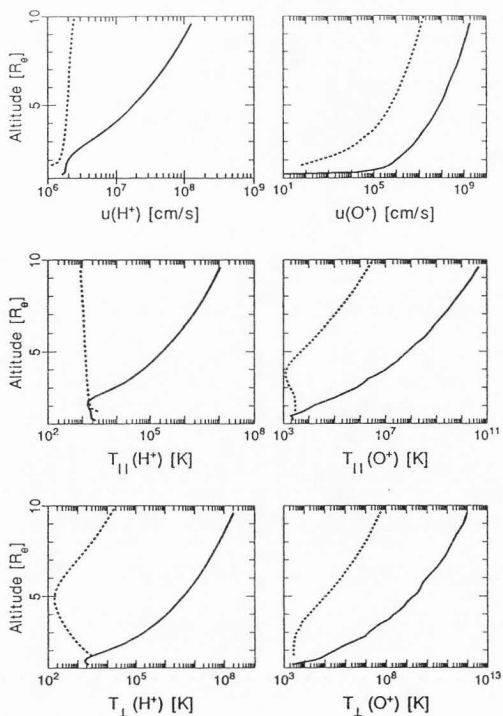


Fig. V. 9. Comparison between the ion moments profiles for the case of the polar wind (dotted) and for the auroral region (solid). The moments considered here are drift velocity u (top), parallel temperature T_{\parallel} (middle), and perpendicular temperature T_{\perp} (bottom), for both H^+ (left) and O^+ (right) ions.

quickly increases in the auroral region (solid), especially at higher altitudes. This is due to the stronger WPI in the auroral region, where the electromagnetic turbulences are more intense. The behavior of $T_{\parallel}(H^+)$ (middle-left) is completely different in the two regions. In the polar wind, $T_{\parallel}(H^+)$ decreases due to parallel adiabatic cooling. However, in the auroral region $T_{\parallel}(H^+)$ decreases at lower altitudes and then increases due to the energy transferred from the perpendicular direction to the parallel direction. This energy transfer dominates the parallel adiabatic cooling above $2.2 R_e$. $T_{\parallel}(H^+)$ increased in the auroral region by a factor of 10^4 while in the polar cap it decreased by a factor of 2 at $10 R_e$.

In the polar wind, the perpendicular adiabatic cooling dominates at low altitudes, causing $T_{\perp}(H^+)$ to decrease until it reaches a minimum at $5 R_e$ (bottom-left panel). Above $5 R_e$ the influence of the WPI is dominant, and $T_{\perp}(H^+)$ increases with altitude. In the auroral region, the relatively higher WPI effect dominates, and hence $T_{\perp}(H^+)$ minimizes at much lower altitudes ($< 2 R_e$).

The right panel of Figure V.9 shows the moments of O^+ ions in the polar cap (dotted) and in the auroral region (solid). The O^+ drift velocity $u(O^+)$ increases in the auroral region more than in the polar cap due to the stronger WPI in the former region.

The parallel temperature $T_{\parallel}(O^+)$ monotonically increases in the auroral region (solid) while it decreases and then increases in the polar cap (dotted). The perpendicular temperature $T_{\perp}(O^+)$ (bottom-right panel) increases in both regions. In the polar wind case (dotted) $T_{\perp}(O^+)$ increases slowly due to the "pressure cooker" effect and then rapidly due to the increase in the WPI with altitude. As expected, $T_{\perp}(O^+)$ in the auroral region exceeds that in the polar wind at all altitudes due to the stronger WPI in the auroral region.

It is clear that the difference between the moments' profiles for the cases of the polar cap and the auroral region is mainly due to the strength of WPI. The electromagnetic turbulence is more intense in the auroral region than in the polar cap. In general, this

makes the auroral region ions have higher parallel temperature, perpendicular temperature, and more rapid drifts at most altitudes. We also found that the minima in the ion temperatures were shallower and occurred at lower altitudes for the auroral region case.

8 Conclusion

A Monte Carlo simulation was used to study the effect of altitude-dependent WPI on O^+ and H^+ ion outflow in the auroral region and the polar cap. The polar wind results were obtained by running the Monte Carlo simulation for the polar cap conditions, which are identical to Barghouthi *et al.* (1994). The auroral region conditions are similar to those of Retterer *et al.* (1987a) with the body forces and an altitude dependent spectral density.

We tested the model by comparing the results of the auroral region simulations, obtained by adopting physical conditions similar to those in Retterer *et al.* (1987a), with the estimates of the mean particle theory (Chang *et al.*, 1986) and the results of Retterer *et al.* (1987a) at $2.0 R_e$. We reproduced the results of Retterer *et al.* (1987a) (i.e., O^+ conic distribution at $2.0 R_e$). The Monte Carlo results for the above case agreed with the estimates of the mean particle theory.

In this study, we assumed the spectral density of the electromagnetic turbulence to be altitude dependent in the auroral region. We discussed the effects of altitude-dependent WPI and neglected body forces on O^+ and H^+ ion outflow in the auroral region. We concluded that :

1. The ions formed a conic-distribution; O^+ -conics occurred at $1.6 R_e$, while H^+ -conics at $2.5 R_e$.
2. As the strength of WPI increases with altitude, the ion (H^+ or O^+) density decreases, drift velocity increases, perpendicular temperature increases, and parallel temperature decreases and then increases.
3. O^+ is preferentially heated.

4. The Monte Carlo calculations agree with the estimates of the mean particle theory at all altitudes in the case of O^+ ions, and at altitudes above $2.5 R_E$ for H^+ ions.

Models that neglected the body forces tend to overestimate or underestimate the behavior of the ion outflow. We discussed the effect of body forces in the auroral region as well as in the polar wind. In the auroral region, the inclusion of body forces did not affect the H^+ ion behavior and also it did not affect the $T_{\perp}(O^+)$, $T_{\parallel}(O^+)$ and $u(O^+)$. However, inclusion of body forces has a major influence on O^+ density $n(O^+)$ and O^+ distribution $f(O^+)$. In particular, $n(O^+)$ decreased very rapidly, and $f(O^+)$ changed from half nondrifting Maxwellian to Maxwellian at low altitudes. Neglecting the body forces in the polar wind tends to overestimate $n(H^+)$, $n(O^+)$, and $T_{\parallel}(H^+)$ at all altitudes, and $T_{\perp}(H^+)$ and $T_{\parallel}(O^+)$ at high altitudes, $u(O^+)$ at lower altitudes, and underestimates $u(H^+)$ at all altitudes, $T_{\perp}(O^+)$ and $T_{\parallel}(O^+)$ at lower altitudes, while $T_{\perp}(O^+)$ and $u(O^+)$ at high altitudes and $T_{\perp}(H^+)$ at low altitudes would not have been affected.

Finally, we compared the effects of altitude-dependent WPI in the polar wind to those in the auroral region. Since WPI is stronger in the auroral region than in the polar cap, this resulted in higher temperatures and larger drift velocities at most altitudes for both ions H^+ and O^+ . Also the minima of the ion temperatures occur at lower altitudes for the auroral region case.

References

- Barakat, A. R., and I. A. Barghouthi, The effect of wave-particle interaction on the polar wind: Preliminary results, *Planet. and spacs sci.*, submitted, 1994a.
- Barakat, A. R., and I. A. Barghouthi, Effects of wave-particle interaction on the oxygen ion outflow in the polar wind, *Geophys. Res. Lett.*, submitted, 1994b.
- Barakat, A. R., H. G. Demars, and R.W. Schunk, Application of the generalized transport equations on the wave-particle interactions at high latitudes, in

- Physics of Space Plasmas*, edited by T. Chang, G. B. Crew, and J. R. Jasper, submitted, 1994.
- Barakat, A. R., and R.W. Schunk**, O⁺ ions in the polar wind, *J. Geophys. Res.*, **88**, 7887-7894, 1983.
- Barakat, A. R., and R.W. Schunk**, Effect of hot electrons on the polar wind, *J. Geophys. Res.*, **89**, 9771-9783, 1984.
- Barakat, A. R., and R.W. Schunk**, Stability of the polar wind, *J. Geophys. Res.*, **92**, 3409-3415, 1987.
- Barakat, A. R., and R.W. Schunk**, Stability of the H⁺ beams in the polar wind, *J. Geophys. Res.*, **94**, 1487-1494, 1989.
- Barghouthi, I. A., A. R. Barakat, A. M. Persoon**, The effects of altitude-dependent WPI on the polar wind plasma, *Annales Geophysicae*, submitted, 1994.
- Chang, T., G. B. Crew, N. Hershkowitz, J. R. Jasperse, J. M. Retterer, and J. D. Winningham**, Transverse acceleration of oxygen ions by electromagnetic ion cyclotron resonance with broadband left-hand-polarized waves, *Geophys. Res. Lett.*, **13**, 636, 1986.
- Chappel, C. R., T. E. Moore, and J. H. Waite, Jr.**, The ionosphere as a fully adequate source of plasma for the earth's magnetosphere, *J. Geophys. Res.*, **92**, 5896-5910, 1987.
- Chen, M. W., and M. Ashour-Abdalla**, Heating of the polar wind due to ion beam instabilities, *J. Geophys. Res.*, **95**, 18,949-18,968, 1990.
- Ganguli, S. B., and P. J. Palmadesso**, Plasma transport in the auroral return current region, *J. Geophys. Res.*, **92**, 8673-8690, 1987.
- Ganguli, S. B., P. J. Palmadesso, and H. G. Mitchell**, Effects of electron heating on the current driven electrostatic ion cyclotron instability and plasma transport processes along auroral field lines, *Geophys. Res. Lett.*, **15**, 1291-1294, 1988.

- Gurnett, D. A., and U. S. Inan**, Plasma wave observations with the Dynamics Explorer 1 spacecraft, *Rev. Geophys.*, **26**, 285-316, 1988.
- Horwitz, J. L.**, Residence time heating effect in auroral conic generation, *Planet. Space Sci.*, **32**, 1115-1117, 1984.
- Li, P., G. R. Wilson, J. L. Horwitz, and T. E. Moore**, Effect of mid-altitude ion heating on ion outflow at polar latitudes, *J. Geophys. Res.*, **93**, 9753-9763, 1988.
- Moore, T. E., C. R. Chappell, M. Lockwood, and J. H. Waite, Jr.**, Superthermal ion signatures of auroral acceleration processes, *J. Geophys. Res.*, **90**, 1611-1618, 1985.
- Retterer, J. M., T. Chang, G. B. Crew, J. R. Jasperse, and J. D. Winningham**, Monte Carlo modeling of oxygen ion conic acceleration by cyclotron resonance, *Phys. Rev. Lett.*, **59**, 148, 1987a.
- Retterer, J. M., T. Chang, G. B. Crew, J. R. Jasperse, and J. D. Winningham**, Monte Carlo modeling of oxygen ion conic acceleration by cyclotron resonance with broadband electromagnetic turbulence, *Physics of Space Plasmas* (1985-87), *SPI Conference proceedings* and reprint series, **Vol. 6**, edited by T. Chang, J. Belcher, J. R. Jasperse, and G. Crew, Scientific Publishers, Inc., Cambridge, MA, (97-111), 1987b.

CHAPTER VI

CONCLUSIONS

I used a Monte Carlo simulation to study the effects of ion-self (Coulomb) collisions on the non-Maxwellian ion velocity distribution in the high-latitude F-region. A similar model was used to study the effects of Coulomb collisions and wave-particle interactions on the ion outflow at high latitudes.

In Chapter II, the velocity distribution function of the ions in the high-latitude F-region was studied with a special attention given to the role of ion-self collisions. A Monte Carlo simulation was used that included the effects of $\mathbf{E} \times \mathbf{B}$ -drift, O^+ collisions with a uniform background of atomic oxygen, and O^+ (Coulomb) self-collisions. Relatively more sophisticated collision models were adopted, and therefore, more realistic results were obtained. It was found that (1) for low altitudes the effect of ion self-collisions is negligible; (2) at high altitudes the role of ion self-collisions becomes important, the toroidal features of the O^+ distribution function becomes less pronounced, parallel temperature increases, and perpendicular temperature decreases.

In Chapter III, a Monte Carlo model was developed to study the outflow of H^+ ions through an O^+ background in the polar wind region. The gravitational force, the polarization electrostatic field, the divergence of the geomagnetic field lines, and the H^+ - O^+ Coulomb collisions were considered. The transition layer that exists between the collision-dominated and the collisionless regions played a significant role in the behavior of the H^+ flow. In the transition region, the shape of H^+ distribution changes rapidly from Maxwellian to "kidney bean." With regard to the moments of f_{H^+} , the flow changes from subsonic in the collision-dominated region to supersonic in the collisionless region with the sonic point occurring in the transition region. The H^+ parallel and perpendicular temperature attain their maxima in the transition region. Both heat fluxes

for parallel and perpendicular energies change very rapidly from positive maxima to negative minima in the transition region.

In Chapter IV, the effects of wave-particle interactions on O^+ and H^+ ions outflow in the polar wind were described using a Monte Carlo simulation. The model includes an altitude dependent wave spectral density, the body forces, and divergence of the geomagnetic field lines. It was concluded that (1) the O^+ velocity distribution develops conic features at high altitudes; (2) the escape flux of O^+ increases by a factor of 40 due to WPI, while the escape flux of H^+ remains constant; (3) the temperature anisotropy (T_{\parallel}/T_{\perp}) reduced at lower altitudes and reversed ($T_{\perp} > T_{\parallel}$) at higher altitudes; and (4) including the effect of finite ion Larmor radius produces toroidal distribution for both H^+ and O^+ .

In Chapter V, the effect of WPI on the behavior of ionospheric plasma was studied for conditions representative of the auroral region. The body forces, divergence of the geomagnetic field lines, and an altitude dependent wave spectral density were taken into consideration. A comparison between the effect of WPI on H^+ and O^+ ion outflow in both the auroral and polar cap showed that (1) O^+ was preferentially energized in both regions; (2) both ions H^+ and O^+ were more energetic in the auroral region at most altitudes; and (3) the body forces were more important in the polar cap than in the auroral region, and for O^+ than H^+ ions.

In general, the theoretical predictions given here are supported by several observations. For instance, the toroidal features of the F-region O^+ distributions were shown [St.-Maurice *et al.*, 1976] to be detectable by a retarding potential analyzer (RPA). The European incoherent scattering radar (EISCAT), with its tristatic mode of operation, was able to measure the O^+ temperature anisotropy. Perraut *et al.* [1984] used the EISCAT data to deduce that O^+ velocity distribution in the auroral F-region was anisotropic, that is, $T_{\perp} / T_{\parallel}$. Moreover, clear signatures of non-Maxwellian distributions

were observed in the data from the EISCAT radar [Winser *et al.*, 1986; Lockwood *et al.*, 1987]. These signatures were similar to those predicted by Raman *et al.* [1981].

In spite of the consistency of the theoretical and observational conclusions, a one-to-one quantitative comparison is not currently possible for the following reasons. In order to produce an acceptable signal-to-noise ratio, the radar output should be integrated over time and space, which limits our ability to uniquely interpret the measurements. Similar limitations apply to the interpretation of the RPA data. On the other hand, the theoretical model is only as reliable as the adopted parameters such as the differential cross section σ . Also, the assumptions included in the model (such as neglecting wave-particle interactions, and assuming homogeneous plasma) introduce more limitations on the theoretical results.

Arguments similar to the ones mentioned above can be used for the polar wind studies. Consistent with our theoretical predictions, the observations showed that the polar wind was supersonic [Persoon *et al.*, 1983] and included a heat flow component [Biddle *et al.*, 1985]. Observations of conic [Retterer *et al.*, 1987] and toroidal O^+ distributions [Moore *et al.*, 1985] constituted further confirmation of the theoretical predictions. The validity of the observations is limited due to the space craft charging (of about 3 - 5 volts), which makes the instruments blind with regard to ions of lower energies. The limited spatial, temporal, and energy resolution further hinders the reliability of the observed data. On the other hand, the model's accuracy is affected by the lack of data about the electromagnetic turbulence wavelength, and neglecting the effect of plasma horizontal drift, etc.

The above discussion indicates that the theory and observations are to be compared in a qualitative sense. Sometimes, both theory and measurements are combined together in order to extract more information from the data as proposed by Kikuchi *et al.* [1989]. Such combined approaches should be used very cautiously, and

their results should be interpreted in the light of the limitations of both theory and observations.

REFERENCES

- Biddle, A. P., T. E. Moore, and C. R. Chappel, Evidence for ion heat flux in the light ion polar wind, *J. Geophys. Res.*, 90, 8552, 1985.
- Kikuchi, K., J.-P. St-Maurice, and A.R. Barakat, Computations of incoherent scattering radar spectrum using Monte Carlo simulation for the ion distribution function, *Annales. Geophys.*, 7, 183, 1989.
- Lockwood, M., B. J. I. Bromage, R. B. Horne, J.-P. St-Maurice, D. M. Willis, and S. W. H. Cowley, Non-Maxwellian ion velocity distributions observed using EISCAT, *Geophys. Res. Lett.*, 14, 111, 1987.
- Moore, T. E., C. R. Chappell, M. Lockwood, and J. H. Waite, Jr., Superthermal ion signatures of auroral acceleration processes, *J. Geophys. Res.*, 90, 1611, 1985.
- Perraut, S., A. Brekke, M. Baron, and D. Hubert, EISCAT measurements of ion temperatures which indicate non-isotropic ion velocity distributions, *J. Atmos. Terr. Phys.*, 46, 531, 1984.
- Persoon, A. M., D. A. Gurnett, and S. D. Shawhan, Polar cap electron densities from DE 1 plasma wave observations, *J. Geophys. Res.*, 88, 10, 123, 136, 1983.
- Raman, R. S. V., J.-P. St-maurice, and R. S. B. Ong, Incoherent scattering of radar waves in the auroral ionosphere, *J. Geophys. Res.*, 86, 4751, 1981.
- Retterer, J. M., T. Chang, G.B. Crew, J. R. Jasperse, and J. D. Winningham, Monte Carlo modeling of oxygen ion conic acceleration resonance, *Phys. Rev. Lett.*, 59, 148, 1987.

St-Maurice, J.-P., W. B. Hanson, and J. C. G. Walker, Retarding potential analyzer measurement of the effect of ion-neutral collisions on the ion velocity distribution in the auroral ionosphere, *J. Geophys. Res.*, 81, 5438, 1976.

Winser, K. J., G. O. L. Jones, and P. J. S. Williams, A quantitative study of the high-latitude ionospheric trough using EISCAT's common programs, *J. Atmos. Terr. Phys.*, 48, 893, 1986.

APPENDIX

Permission Letter

5 February 1994

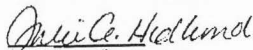
American Geophysical Union
2000 Florida Avenue, N.W.
Washington D. C. 20009

I am in the process of preparing my dissertation in the Physics Department at Utah State University. I hope to complete in the winter of 1994.

I am requesting your permission to include the paper (Monte Carlo Study of the Transition Region in the Polar Wind: An Improved Collision Model) as a chapter in my dissertation. The authors of this paper are I. A. Barghouthi (my self), A. R. Barakat, and R. W. Schunk. The paper number is 93JA01190. I would like you to know that I have the co-authors' permission. I will include appropriate citation to your work.

Please indicate your approval of this request by signing in the space provided.

If you have any questions, please contact me.


(Signed)

THE UNIVERSITY OF IOWA



14 February 1994

Imad A. Barghouthi
Department of Physics
Utah State University
Logan, UT 84322-4415

Dear Mr. Barghouthi:

As one of your co-authors, I give my permission for you to include the paper entitled "The Effects of Altitude-Dependent Wave-Particle Interactions on the Polar Wind Plasma" as a chapter in your dissertation.

If I can be of further help, please let me know.

Sincerely,

Ann M. Persoon

AMP/k

COPYRIGHT PERMISSION LETTERS



American Geophysical Union

2000 Florida Avenue, N.W.
Washington, D.C. 20009
Phone (202) 462-6900
TWX 710-822-9300
FAX 202-328-0566

AGU POLICY ON REPRODUCTION OF COPYRIGHT MATERIALS

AGU no longer requires that permission be obtained from AGU or the author(s) for the use of tables, figures, or short extracts of papers published in AGU journals or books, provided that the source be appropriately cited; however, the author's permission must be obtained for modifying the material in any way beyond simple redrawing.

We recommend that the credit line read "authors, journal or book title, volume number, page number(s), year, copyright by the American Geophysical Union." If an article was placed in the public domain, in which case the words "Not subject to U.S. copyright" appear on the bottom of the first page of the article, please substitute "published" for the word "copyright" in the credit line mentioned above.

Also, AGU policy requires that the article be published by AGU before any material may be reproduced therefrom.

AGU Publications

CURRICULUM VITAE**Personal:**

Name :	Imad A. Barghouthi
Area of Specialization :	Theoretical Space Plasma Physics
Nationality :	Palestinian
Marital Status:	Married
Languages :	Fluent in English and Arabic

Education:

- 09/89 - 02/94 Utah State University, Logan, Utah, Physics, Ph.D.
- 01/85 - 01/88 University of Jordan, Amman, Jordan, Nuclear Physics, M.Sc.
- 09/81 - 01/85 University of Jordan, Amman, Jordan, Physics, B.Sc.

Employment:

- 06/91 - 02/94 Utah State University, Logan, Utah, Research Assistant. Currently working on a funded project by NASA. The name of the project is "The effect of wave-particle interactions on ion outflow at high latitudes".
- 10/89 - 06/91 Utah State University, Logan, Utah, Teaching Assistant. During this period, taught recitations of the General Physics course (Phyx 221, 222, 223)
- 01/85 - 01/88 University of Jordan, Amman, Jordan, Teaching Assistant, During this period, instructed the labs of the General Physics course.

Field of Research Interest:

1. Plasma Physics (Wave-Particle-Interactions, Coulomb Collisions in Space Plasma, and Plasma Transport Theory).
2. Ionospheric Physics (Polar Wind, High Latitude F-Region, Auroral Region, and Ion Velocity Distribution and its Moments).
3. Monte Carlo Methods.
4. Nuclear and Particle Physics Theory (Nuclear Reactions, Scattering Theory, and Electro Weak Theory).

Awards:

1. Selected as one of the top three presentations, 17th NSF CEDAR Workshop, Boulder, Colorado, June 1992.
2. Arab Students Aid International Scholarship (for two years 1990 - 1992)
3. University of Jordan's Honor List (four semesters, 1983 - 1984).

References:

Abdallah R. Barakat (Center for Atmospheric and Space Sciences, Utah State University, Logan, UT 84322-4405, U.S.A.)

Robert W. Schunk ((Center for Atmospheric and Space Sciences, Utah State University, Logan, UT 84322-4405, U.S.A.)

J. Lemaire (IASB, 3 Avenue Circulaire, B-1180 Brussels, Belgium)

James Wheeler (Dept. of Physics, Utah State University, Logan, UT 84322-4415, U.S.A.)

Howard G. Demars (Center for Atmospheric and Space Sciences, Utah State University, Logan, UT 84322-4405, U.S.A.)

Conferences/Workshops Attended:

1. MIT Symposium/Cambridge Workshop, June 1993.
2. American Geophysical Union Fall Meeting, San Francisco, December 1992.
3. DE Science Team Meeting, Greenbelt, Maryland, October 1992.
4. 17th NSF CEDAR Workshop, Boulder, Colorado, June 1992.
5. American Geophysical Union Fall Meeting, San Francisco, December 1991.
6. American Geophysical Union Fall Meeting, San Francisco, December 1990.
7. Foreign Teaching Assistants Workshop, Utah State University, Logan, Utah, September 1990.

Publications:

1. Monte Carlo study of the transition from collision-dominated to collisionless polar wind flow, (A.R. Barakat, R.W. Schunk, I.A. Barghouthi, and J. Lemaire), in *Physics of Space Plasmas*, edited by T. Chang, and J. Crew, pp. 431-437, Scientific Publishers, Cambridge, MA, (1991).
2. Monte Carlo Study of the Transition Region in the Polar Wind: An Improved Collision Model (I.A. Barghouthi, A.R. Barakat, and R.W. Schunk), *J. Geophys. Res.*, (1993).
3. Comparison between the wave-particle interaction in the polar wind and in the auroral region, (I.A. Barghouthi, and A.R. Barakat), *Physics of Space Plasmas*, in press (1994).
4. A Monte Carlo simulation for the Effect of Ion Self-collisions on the Ion Velocity distribution Function in the High-Latitude F-region, (I.A. Barghouthi, A.R. Barakat, and R.W. Schunk), *Annales Geophysicae*, submitted 1993.
5. The effect of wave-particle-interaction on the polar wind: Preliminary results, (A.R. Barakat, and I.A. Barghouthi), *Planet. and Space Sci.*, submitted, 1994.
6. The Effects of Altitude-Dependent Wave-Particle Interactions on the Polar Wind Plasma, (I.A. Barghouthi, A.R. Barakat, and A.M. Persoon), *Annales Geophysicae*, submitted, 1994.
7. The Effects of Wave-Particle interactions on H⁺ and O⁺ outflow at High Latitude: A comparative study, (I.A. Barghouthi), *Planetary and Space Sci.*, submitted, 1994.
8. The Effect of Wave-Particle interactions on the polar wind O⁺, (A.R. Barakat, and I.A. Barghouthi), *Geophys. Res. Lett.*, submitted, 1994.
9. Double Hump distributions in the polar wind, (A.R. Barakat, and I.A. Barghouthi), *Phys. Rev. Lett.*, submitted, 1994.

Papers Presented in Conferences and Seminars:

1. The Effect of Wave-Particle interactions on H^+ and O^+ outflow at high latitude: A comparative study, (I.A. Barghouthi, and A.R. Barakat), 1993 MIT Symposium/ Cambridge Workshop, June 1993.
2. The Effect of the Wave-Particle Interaction on the PolarWind, (I.A. Barghouthi, and A. R. Barakat), AGU Fall Meeting, San Francisco, December 1992.
3. A Monte Carlo Simulation for Wave-Particle Interaction in Space Plasma, Physics colloquium, Utah State University, Fall 1992.
4. The Effect of Wave-Particle-Interaction on the Polar Wind: A Parametric study, (A.R. Barakat, and I.A. Barghouthi), DE Science Team Meeting, Greenbelt, Maryland, October 1992.
5. Altitude Dependence of Wave-Particle Interaction and its Effect on the Ion Outflow in the Polar Wind, (I.A. Barghouthi, A.R. Barakat, and A. Persoon), DE Science Team Meeting, Greenbelt, Maryland, October 1992.
6. The Effect of Ion Self-Collisions on the Non-Maxwellian Ion Distribution and the Resulting Radar Spectrum in the High-Latitude F-region, (I.A. Barghouthi, A.R. Barakat, and R.W. Schunk), 17th NSF CEDAR Workshop, Boulder, Colorado, June, 1992.
7. Effects of self collisions on the non-Maxwellian ion velocity distribution function in the high-latitude F-region. (I.A. Barghouthi, A.R. Barakat, and R.W. Schunk), AGU Fall meeting, San Francisco, December 1991.
8. H^+ outflow in the polar wind: A Monte Carlo study, (I.A. Barghouthi, A.R. Barakat, R.W. Schunk, and J. Lemaire), AGU Fall meeting, San Francisco, December 1990.
9. A Monte Carlo study of the transition layer between the collision dominated and the collisionless regions in the polar wind, (A.R. Barakat, R.W. Schunk, I.A. Barghouthi, and J. Lemaire) Cambridge Workshop in Theoretical Geoplasma Physics, Cambridge, MA, USA, July 1990.

Invited Presentation:

1. The Effect of Wave-Particle Interaction on the Polar Wind, (A.R. Barakat, and I.A. Barghouthi) Third Huntsville Workshop on Ionosphere/ Magnetosphere Plasma Models, Huntsville, Alabama, October 1992.